

Advances in Meteorology

Advances in Remote Sensing and Modeling of Terrestrial Hydrometeorological Processes and Extremes

Guest Editors: Ke Zhang, Jingfeng Wang, Iftekhar Ahmed,
and Prasanna H. Gowda





**Advances in Remote Sensing and Modeling of
Terrestrial Hydrometeorological
Processes and Extremes**

Advances in Meteorology

**Advances in Remote Sensing and Modeling of
Terrestrial Hydrometeorological
Processes and Extremes**

Guest Editors: Ke Zhang, Jingfeng Wang, Iftekhar Ahmed,
and Prasanna H. Gowda



Copyright © 2016 Hindawi Publishing Corporation. All rights reserved.

This is a special issue published in "Advances in Meteorology." All articles are open access articles distributed under the Creative Commons Attribution License, which permits unrestricted use, distribution, and reproduction in any medium, provided the original work is properly cited.

Editorial Board

José Antonio Adame, Spain
Cesar Azorin-Molina, Spain
Guillermo Baigorria, USA
Marina Baldi, Italy
Abderrahim Bentamy, France
Massimo A. Bollasina, UK
Stefania Bonafoni, Italy
Isabella Bordi, Italy
Alex Cannon, Canada
Claudio Carbone, Italy
Dominique Carrer, France
Charles Chemel, UK
Annalisa Cherchi, Italy
James Cleverly, Australia
Jill S. M. Coleman, USA
Gabriele Curci, Italy
Mladjen Ćurić, Serbia
Maher A. Dayeh, USA
Klaus Dethloff, Germany
Panuganti C. S. Devara, India
Julio Diaz, Spain
Arona Diedhiou, France
Stefano Dietrich, Italy
E. Domínguez Vilches, Spain
Antonio Donateo, Italy
Igor Esau, Norway
Stefano Federico, Italy
Enrico Ferrero, Italy
Rossella Ferretti, Italy
Roberto Fraile, Spain
Charmaine Franklin, Australia

Jan Friesen, Germany
María Ángeles García, Spain
Herminia García Mozo, Spain
Eduardo García-Ortega, Spain
Luis Gimeno, Spain
Jorge E. Gonzalez, USA
Ismail Gultepe, Canada
Rafiq Hamdi, Belgium
Adel Hanna, USA
Hiroyuki Hashiguchi, Japan
Tareq Hussein, Jordan
Bradley G. Illston, USA
Ivar S A Isaksen, Norway
Yasunobu Iwasaka, Japan
Pedro Jiménez-Guerrero, Spain
Kuruvilla John, USA
Charles Jones, USA
Hann-Ming H. Juang, USA
George Kallos, Greece
Harry D. Kambezidis, Greece
Nir Y. Krakauer, USA
Simon O. Krichak, Israel
Hisayuki Kubota, Japan
Haim Kutiel, Israel
Richard Leaitch, Canada
Monique Leclerc, USA
Ilan Levy, Israel
Gwo-Fong Lin, Taiwan
Anthony R. Lupo, USA
Paolo Madonia, Italy
Andreas Matzarakis, Germany

Samantha Melani, Italy
Nicholas Meskhidze, USA
Christophe Messenger, France
Mario M. Miglietta, Italy
Takashi Mochizuki, Japan
Goro Mouri, Japan
Brian R. Nelson, USA
Efthymios I. Nikolopoulos, USA
Sandip Pal, USA
Giulia Panegrossi, Italy
Giulia Pavese, Italy
Kyaw T. Paw, USA
Olivier P. Prat, USA
Sara C. Pryor, USA
Philippe Ricaud, France
Tomeu Rigo, Spain
Filomena Romano, Italy
Haydee Salmun, USA
Pedro Salvador, Spain
Arturo Sanchez-Lorenzo, Spain
Andres Schmidt, USA
Shraddhanand Shukla, USA
Fiona Smith, UK
Francisco J. Tapiador, Spain
Yoshihiro Tomikawa, Japan
Tomoo Ushio, Japan
Rogier Van Der Velde, Netherlands
Francesco Viola, Italy
Alastair Williams, Australia
Olga Zolina, France

Contents

Advances in Remote Sensing and Modeling of Terrestrial Hydrometeorological Processes and Extremes

Ke Zhang, Jingfeng Wang, Iftekhar Ahmed, and Prasanna H. Gowda

Volume 2016, Article ID 4371840, 3 pages

Impact of Climate Change on Hydrologic Extremes in the Upper Basin of the Yellow River Basin of China

Jun Wang, Zhongmin Liang, Dong Wang, Tian Liu, and Jing Yang

Volume 2016, Article ID 1404290, 13 pages

Satellite Retrieval of Surface Evapotranspiration with Nonparametric Approach: Accuracy Assessment over a Semiarid Region

Xin Pan, Yuanbo Liu, and Xingwang Fan

Volume 2016, Article ID 1584316, 14 pages

Accelerating the SCE-UA Global Optimization Method Based on Multi-Core CPU and Many-Core GPU

Guangyuan Kan, Ke Liang, Jiren Li, Liuqian Ding, Xiaoyan He,

Youbing Hu, and Mark Amo-Boateng

Volume 2016, Article ID 8483728, 10 pages

Are GRACE-era Terrestrial Water Trends Driven by Anthropogenic Climate Change?

J. T. Fasullo, D. M. Lawrence, and S. C. Swenson

Volume 2016, Article ID 4830603, 9 pages

Trends in Extreme Precipitation Indices in Iran: 1951–2007

Robert C. Balling Jr., Mohammad Sadegh Keikhosravi Kiany, Shouraseni Sen Roy, and Javad Khoshhal

Volume 2016, Article ID 2456809, 8 pages

Spatial Combination Modeling Framework of Saturation-Excess and Infiltration-Excess Runoff for Semihumid Watersheds

Pengnian Huang, Zhijia Li, Cheng Yao, Qiaoling Li, and Meichun Yan

Volume 2016, Article ID 5173984, 15 pages

Relationship between Evapotranspiration and Land Surface Temperature under Energy- and Water-Limited Conditions in Dry and Cold Climates

Zhigang Sun, Qinxue Wang, Ochirbat Batkhishig, and Zhu Ouyang

Volume 2016, Article ID 1835487, 9 pages

Editorial

Advances in Remote Sensing and Modeling of Terrestrial Hydrometeorological Processes and Extremes

Ke Zhang,^{1,2} Jingfeng Wang,³ Iftekhar Ahmed,⁴ and Prasanna H. Gowda⁵

¹State Key Laboratory of Hydrology-Water Resources and Hydraulic Engineering and College of Hydrology and Water Resources, Hohai University, 1 Xikang Road, Nanjing, Jiangsu 210098, China

²Cooperative Institute for Mesoscale Meteorological Studies, The University of Oklahoma, 120 David L. Boren Boulevard, Norman, OK 73072, USA

³School of Civil and Environmental Engineering, Georgia Institute of Technology, Atlanta, GA 30332, USA

⁴Department of Civil & Environmental Engineering, Prairie View A&M University, Prairie View, TX 77446, USA

⁵Forage and Livestock Production Unit, USDA Agricultural Research Service, El Reno, OK 73036, USA

Correspondence should be addressed to Ke Zhang; kzhang@hhu.edu.cn

Received 12 June 2016; Accepted 13 June 2016

Copyright © 2016 Ke Zhang et al. This is an open access article distributed under the Creative Commons Attribution License, which permits unrestricted use, distribution, and reproduction in any medium, provided the original work is properly cited.

Remote sensing is an indispensable tool for monitoring and detecting the evolution of the Earth's hydrometeorological processes. Fast-growing remote sensing observations and technologies have been a primary impetus to advancing our knowledge of hydrometeorological processes and their extremes over the last decades. Meanwhile, integrating the hydrological-meteorological processes and bridging traditional disciplines are emerging as the frontier of hydrological and meteorological studies. These progresses opened new opportunities to advance the studies of modeling and forecasting climate change related extremes for adaptation and mitigation of hydrometeorological hazards. This special issue gathers a number of contributions in remote sensing and modeling of hydrometeorological processes and extremes, including retrieval methods, validation of satellite retrieval results, hydrological modeling, application of parallel computing in model optimization, and analysis of spatiotemporal changes in hydrological regimes. The investigated hydrologic variables in these studies contain precipitation, evapotranspiration, stream flow, and water storage.

Remote sensing of actual evapotranspiration (ET) has been a hot topic in the past two decades. Many ET retrieval algorithms have emerged and formed many different types of approaches, including the thermal remote sensing based surface energy balance approaches [1, 2], process-based Penman-Monteith methods [3–5], land surface temperature-vegetation index space models [6, 7], maximum entropy

production model [8], and water balance method [9]. In this special issue, a couple of studies are also devoted to this research effort. X. Pan et al. applied a recently developed nonparametric ET retrieval model in a semiarid region of China and evaluated it against observations from six eddy-covariance flux sites that represent desert, Gobi, cropland, orchard, vegetable field, and wetland. The ET retrieval model ingests net radiation, surface air temperature, land surface temperature, and soil heat flux, which can be provided or estimated by satellite remote sensing, to estimate ET without the need of parameterizing surface resistance. This model is simple but generally effective in the study region, making it potentially applicable for a larger region. Z. Sun et al. investigated the relationship between ET and remotely sensed land surface temperature (LST) under energy- and water-limited conditions in Mongolia. Their study demonstrates that ET and LST have a general negative relationship under the water-limited condition in a dry and cold climate, but the relationship between ET and LST varies under the energy-limited condition. This study suggests that LST-based ET retrieval needs to account for different ET behaviors under energy- and water-limited conditions in the dry and cold regions.

It has been about fifteen years since the launch of the Gravity Recover and Climate Experiment (GRACE) satellite in March 2002. It provides the very first global continuous monitoring of near-surface mass, in particular terrestrial water storage, and has revealed major changes across a range

of timescales including strong seasonal shifts, interannual variations, and apparent trends [10]. In this special issue, J. T. Fasullo et al. utilized both GRACE observations and model simulations from the CESM1-CAM5 Large Ensemble (LE) to examine changes in global terrestrial water storage (TWS) during the GRACE era (2003–2014). They found that trends in the LE TWS simulations are dominated by internal variability rather than by the forced response, with TWS anomalies in much of the Americas, eastern Australia, Africa, and southwestern Eurasia largely attributable to the negative phases of the Pacific Decadal Oscillation and Atlantic Multi-decadal Oscillation. They also concluded that it is inappropriate to attribute trends mainly to anthropogenic forcing despite the similarities between observed trends and the model-inferred forced response. Their findings highlight the challenge of detecting anthropogenic climate change in temporally finite satellite datasets and underscore the benefit of utilizing models in the interpretation of the observed record.

Investigation and attribution of changes in the hydrologic regimes and extremes also draw much attention from the hydrometeorology community and are another important study area. R. C. Balling Jr. et al. examined trends in extreme precipitation in Iran from 1951 to 2007 using observation-based APHRODITE daily rainfall data. They used seven different indices of extreme precipitation, including annual precipitation total, number of days above a certain threshold, maximum precipitation received over a certain period of time, maximum one-day precipitation, and number of days with precipitation above the 90th percentile, to quantify the characteristics of the precipitation regime in Iran. They further conducted the trend and principal component analyses of these index time series. Their results show that all seven indices show an upward trend through the study period, indicating increase in total rainfall and rainfall extreme, which may be related to the climate change in this region. Meanwhile, the upward trend in extreme precipitation exhibits a strong southwest-to-northeast gradient across Iran. In another study, J. Wang et al. investigated the impact of projected climate change in the next 50 years on hydrologic extremes in the upper Yellow River Basin of China based on statistical analysis and hydrologic modeling. This basin is an important region in China for providing hydropower. Their results show that the values of different long duration (15, 30, and 60 days) rainfall extremes for several given probabilities in this basin will slightly rise in the future. Correspondingly, long duration flood volume extremes will increase as well. These results suggest that planning for flood control, hydropower production, agriculture irrigation, and ecosystem preservation in this region needs to take these changes into account.

Advances in the runoff generation mechanisms and their representations in the hydrologic and land surface models are important for improving the accuracy of modeling land surface hydrologic fluxes. P. Huang et al. compared the applicability of saturation-excess mechanism, infiltration-excess mechanism, and their combination in a semiarid basin. Based on these runoff yield concepts and GIS and remote sensing techniques, they designed an event-based spatial combination modeling framework and developed

two spatial combination models that account for spatial distribution and variability of runoff generation processes from saturation-excess and infiltration-excess mechanisms. The results demonstrate that delineation and differentiation of different runoff generation processes across the space certainly help to improve the accuracy of simulations relative to applying single runoff yield mechanism.

Utilizing advanced computational technologies to facilitate modeling efficiency and application is another interesting study area. For example, SCE-UA is a well-known, robust global optimization method. However, it has a high computational load, which prohibits the application of SCE-UA to high-dimensional and complex problems. G. Kan et al. proposed two parallel SCE-UA methods and implemented them on Intel multicore CPU and NVIDIA many-core GPU using OpenMP and CUDA Fortran, respectively. The parallel methods are not only reliable but also highly efficient, which can largely reduce the time consumed for model calibration and optimization.

There is no doubt that there are much more studies that represent recent advances and research directions in remote sensing and modeling of terrestrial hydrometeorological processes and extremes. However, the papers collected in this special issue cover a wide range of research topics and shed light on some of recent progresses and ideas in the field. It will serve as valuable asset for the scientists and engineers in hydrometeorology and related fields.

Acknowledgments

We thank all the authors who contributed to this issue and all the reviewers who provide valuable, constructive comments to the manuscripts and help to improve the quality of these papers published in this issue.

Ke Zhang
Jingfeng Wang
Iftexhar Ahmed
Prasanna H. Gowda

References

- [1] J. M. Norman, M. C. Anderson, W. P. Kustas et al., “Remote sensing of surface energy fluxes at 10^1 -m pixel resolutions,” *Water Resources Research*, vol. 39, no. 8, article 1221, 18 pages, 2003.
- [2] R. G. Allen, M. Tasumi, and R. Trezza, “Satellite-based energy balance for mapping evapotranspiration with internalized calibration (METRIC)—model,” *Journal of Irrigation and Drainage Engineering-ASCE*, vol. 133, no. 4, pp. 380–394, 2007.
- [3] K. Zhang, J. S. Kimball, R. R. Nemani et al., “Vegetation greening and climate change promote multidecadal rises of global land evapotranspiration,” *Scientific Reports*, vol. 5, Article ID 15956, 9 pages, 2015.
- [4] Q. Z. Mu, M. S. Zhao, and S. W. Running, “Improvements to a MODIS global terrestrial evapotranspiration algorithm,” *Remote Sensing of Environment*, vol. 115, no. 8, pp. 1781–1800, 2011.
- [5] Y. Q. Zhang, J. L. Peña-Arancibia, T. R. McVicar et al., “Multi-decadal trends in global terrestrial evapotranspiration and its

- components,” *Scientific Reports*, vol. 6, Article ID 19124, 12 pages, 2016.
- [6] O. Merlin, J. Chirouze, A. Olioso, L. Jarlan, G. Chehbouni, and G. Boulet, “An image-based four-source surface energy balance model to estimate crop evapotranspiration from solar reflectance/thermal emission data (SEB-4S),” *Agricultural and Forest Meteorology*, vol. 184, pp. 188–203, 2014.
- [7] Y. T. Yang and S. H. Shang, “A hybrid dual-source scheme and trapezoid framework-based evapotranspiration model (HTEM) using satellite images: algorithm and model test,” *Journal of Geophysical Research-Atmospheres*, vol. 118, no. 5, pp. 2284–2300, 2013.
- [8] J. F. Wang and R. L. Bras, “A model of evapotranspiration based on the theory of maximum entropy production,” *Water Resources Research*, vol. 47, no. 3, Article ID W03521, 2011.
- [9] Z. M. Wan, K. Zhang, X. W. Xue, Z. Hong, Y. Hong, and J. J. Gourley, “Water balance-based actual evapotranspiration reconstruction from ground and satellite observations over the conterminous United States,” *Water Resources Research*, vol. 51, no. 8, pp. 6485–6499, 2015.
- [10] J. T. Reager, A. S. Gardner, J. S. Famiglietti, D. N. Wiese, A. Eicker, and M.-H. Lo, “A decade of sea level rise slowed by climate-driven hydrology,” *Science*, vol. 351, no. 6274, pp. 699–703, 2016.

Research Article

Impact of Climate Change on Hydrologic Extremes in the Upper Basin of the Yellow River Basin of China

Jun Wang,¹ Zhongmin Liang,^{1,2} Dong Wang,¹ Tian Liu,¹ and Jing Yang¹

¹College of Hydrology and Water Resources, Hohai University, Nanjing 210098, China

²State Key Laboratory of Hydrology-Water Resources and Hydraulic Engineering, Hohai University, Nanjing 210098, China

Correspondence should be addressed to Zhongmin Liang; zmlianghhu@126.com

Received 16 October 2015; Revised 21 February 2016; Accepted 17 March 2016

Academic Editor: Jingfeng Wang

Copyright © 2016 Jun Wang et al. This is an open access article distributed under the Creative Commons Attribution License, which permits unrestricted use, distribution, and reproduction in any medium, provided the original work is properly cited.

To reveal the revolution law of hydrologic extremes in the next 50 years and analyze the impact of climate change on hydrologic extremes, the following main works were carried on: firstly, the long duration (15 d, 30 d, and 60 d) rainfall extremes according to observed time-series and forecast time-series by dynamical climate model product (BCC-CSM-1.1) were deduced, respectively, on the basis that the quantitative estimation of the impact of climate change on rainfall extremes was conducted; secondly, the SWAT model was used to deduce design flood with the input of design rainfall for the next 50 years. On this basis, quantitative estimation of the impact of climate change on long duration flood volume extremes was conducted. It indicates that (1) the value of long duration rainfall extremes for given probabilities (1%, 2%, 5%, and 10%) of the Tangnaihai basin will rise with slight increasing rate from 1% to 6% in the next 50 years and (2) long duration flood volume extremes of given probabilities of the Tangnaihai basin will rise with slight increasing rate from 1% to 6% in the next 50 years. The conclusions may provide technical supports for basin level planning of flood control and hydropower production.

1. Introduction

Climate change has affected many fields of nature and human society in recent years and has been one of the most attractive research fields. On the background, the estimation and simulation of the impact of climate change in the hydrology have been becoming a research topic. Many hydrologists [1–4], who have done research on the hydrological response to climate change and human activities, believe that anthropogenic global climate change and human activities have significantly affected hydrologic cycle and resulted in changes in the spatial and temporal distribution of water resources at both global and local scales. It is no doubt that the changes in the hydrological cycle will have serious impacts on ecological, social, and economic situations [5, 6] and bring us severe challenges. To respond to the climate change challenge, one of the most important tasks is to reveal influencing mechanism of hydrologic cycle by climate change and to predict the impact on corresponding fields. Many hydrologists have been working on it; for example, some studies have identified

robust trends over some specific regions [7, 8]. However, there are still many questions unclear and the research should be continued. With the development of society, the demand of scientificity of the basin level and national planning of flood control, hydropower production, agricultural irrigation, and ecosystem preservation are increasing; hence, projecting the future climate and assessing its probable impact on water resources are critical. Many studies on the impacts of climate change on hydrological regimes [9–11] have been conducted. In these studies, global climate models and hydrologic model were usually used to simulate the changes in hydrological regimes at watershed scales.

Most of the previous climate change impact assessment studies on hydrological processes of Yellow River watershed focused on the trend of hydrologic elements [12]. However, the assessment study on revolution law of the hydrologic extremes responding to climate change of Yellow River basin is hardly a blank. To reveal the revolution law of hydrologic extremes and assess the impact of climate change on hydrologic extremes in the upper Yellow River basin,

the objectives of the paper include (1) evaluation of the impact of climate change on precipitation extremes of long duration (15 d, 30 d, and 60 d) for given probabilities (1%, 2%, 5%, and 10%); (2) evaluation of the impact of climate change on flood volume extremes of long duration (15 d, 30 d, and 60 d) for given probabilities (1%, 2%, 5%, and 10%), through hydrologic frequency analysis that deduce the design rainfall for the measured phase and the future by running distributed hydrological model (SWAT) with the input condition of design rainfall to deduce the flood volume extreme of different duration. The paper focuses on revealing the impact of climate change on the hydrologic extremes of the Tangnaihain basin which locates in the upstream of Yellow River; the main content is as follows: the methods applied to study the impact of climate change on hydrologic extreme, including hydrologic frequency analysis method, the bias correction method, and the hydrological model, are described in Section 2. The study area and available data are then introduced in the Section 3. The results of impact of climate change on hydrologic extremes are presented in Section 4. The conclusions are finally remarked in Section 5.

2. Methodologies

2.1. Frequency Analysis of Precipitation Extremes. To reveal the statistical law of the hydrologic extremes, hydrologic time series analysis and modeling are an effective approach. Obviously, hydrologic frequency analysis is one of most popular approaches which are based on time series to analyze the law of hydrologic extremes [13, 14]. The key of hydrologic frequency analysis is to determine the probability distribution of extreme. As we known, there are many functions, including extreme value distribution (Gumbel distribution), generalized extreme value distribution (GEV), log-normal distribution (L-N), the Pearson type III distribution (P-III), and the logarithmic Pierre Johnson III distribution, that could be used as the probability distribution of hydrologic extremes.

In China, Liang [15] showed that the P-III distribution is suitable for description of the statistical law of hydrologic extremes, such as annual maximum rainfall, annual maximum flood peak discharge, and annual maximum flood volume of different duration, based on the application experiences. Therefore, the Pearson type III (P-III) curve has been used for the hydrologic frequency analysis in China.

The P-III curve is known as the γ distribution mathematically (Gamma distribution with three parameters). Its probability density function is expressed as follows:

$$f(x) = \frac{\beta^\alpha}{\Gamma(\alpha)} (x - a_0)^{\alpha-1} e^{-\beta(x-a_0)}, \quad (1)$$

$$x > a_0, \alpha > 0, \beta > 0,$$

where a_0 , β , and α denote the position, scale, and shape parameters of the distribution, respectively. The relation of

these parameters and three moments (Ex , Cv , and Cs) can be expressed as follows:

$$a_0 = Ex \left(1 - \frac{2Cv}{Cs} \right),$$

$$\alpha = \frac{4}{Cs^2}, \quad (2)$$

$$\beta = \frac{2}{ExCvCs},$$

where Ex denotes the mean of hydrologic extreme time series; Cv is the variance of hydrologic extreme time series; and Cs is the variable coefficient of hydrologic extreme time series.

Hydrologic frequency analysis and calculation are to ascertain the random variable x corresponding to the specified frequency p , which can be obtained by the distribution function defined by transcendental probability:

$$p = F(x_p) = P(x \geq x_p) = \int_{x_p}^{\infty} f(x) dx. \quad (3)$$

To simplify the integration solution of (3), the variables of the Pearson type III distribution can be obtained by standard transformation of variable x :

$$\Phi = \frac{x - Ex}{ExCv}, \quad (4)$$

where Φ is known as coefficient of mean deviation. Then the integral operation of x is

$$p = P(\Phi \geq \Phi_p) = \int_{\Phi_p}^{\infty} g(\Phi, \alpha) d\Phi$$

$$= \frac{\alpha^{\alpha/2}}{\Gamma(\alpha)} \int_{\Phi_p}^{\infty} (\Phi + \sqrt{\alpha})^{\alpha-1} e^{-\sqrt{\alpha}(\Phi + \sqrt{\alpha})} d\Phi, \quad (5)$$

where the integrand $g(\Phi, \alpha)$ contains only one unknown parameter α or Cs ($\alpha = 4/Cs^2$). According to hydrologic customary, the relationship of Cs , p , and Φ_p is tabulated in advance, namely, Φ -value hydrographic table. The corresponding x_p can be obtained through the inverse transform of (4) which is expressed as follows:

$$x_p = Ex(1 + Cv\Phi_p). \quad (6)$$

2.2. Frequency Analysis of Flood Volume Extremes with Different Durations. Approach to deduce flood volume extremes with different durations can be divided into two types according to the data condition [16]: one is the so-called direct method when the length of observed discharge time series is relatively long. According to observed maximum discharge time series, the flood volume extremes of different duration with a certain probability can be deduced by hydrologic frequency analysis as shown in Section 2.1; the other one is the so-called indirect method when the length of observed discharge time series is relatively short or there is no observed discharge data. According to observed precipitation

data, the precipitation extremes of different duration with a certain probability can be deduced by hydrologic frequency analysis firstly, on the basis that the flood volume extremes with different durations of corresponding probability can be deduced by rainfall-runoff model on the hypothesis that rainfall with given frequency could generate the flood with the same frequency.

There are many hydrologic models for rainfall-runoff simulation; in the paper, the SWAT model which is famous as distributed hydrologic model and widely applied all over the world was adopted to deduce the flood volume.

2.3. Hydrologic Model: SWAT. To evaluate quantitatively the impact of climate change on the flood extreme, hydrologic model is needed to simulate the flood. There are many rainfall-runoff models such as Xin'anjiang model, TOP-MODEL, and VIC model. In the paper, SWAT model was selected because of its powerful hydrological process simulation capabilities. Known as a famous distributed hydrologic model, SWAT model is a continuous-time, semidistributed, process-based river basin or watershed scale model. SWAT model was developed to predict the impact of land management practices on water, sediment, and chemical yields in agricultural watersheds with varying soils, land use, and management conditions over long period of time [17, 18]. Comparing with other hydrologic models, SWAT has two outstanding features. One is the use of Hydrologic Response Unit (HRU), which is divided according to land use, soil distribution, and slope type, as the calculation unit [19]. SWAT divides a watershed into subbasins. Each subbasin is connected through a stream channel and further each subbasin is divided into HRUs. SWAT simulates hydrology and sediment at the HRU level. Water and sediment from each HRU are summarized in each subbasin and then routed through the stream network to the watershed outlet [18, 20]. The other one is the simulation of surface runoff by using the modified SCS curve number which is deduced based on land use and soil type of watershed [21].

2.4. Bias Correction of Climate Model. Systematic errors of climate models may lead to unrealistic hydrological simulations of river flow [22, 23]; thus, bias correction methods must be implemented to correct the climate product before application and analysis. For adjusting climate model product, the linear scaling, local intensity scaling, power transformation, variance scaling, distribution transfer, and the delta-change approaches are the commonly used bias correction methods [24]. Bias correction methods are based on the assumption that the same correction algorithm applies to both current and future climate conditions. In the study, linear scaling method was employed to correct the daily precipitation and monthly precipitation of climate model.

Based on the precipitation simulated by climate model and the corresponding measured precipitation, correction coefficients of each month were calculated. The precipitation predicted by climate model was modified on the basis of correction coefficients scaling monthly precipitation data

predicted by the model. The correction coefficient can be calculated by

$$\lambda_i = \frac{\overline{P}_i^o}{\overline{P}_i}, \quad (7)$$

where λ_i is the correction coefficient of the i th month, \overline{P}_i^o is the measured monthly mean precipitation of the i th month of reference period, and \overline{P}_i is the monthly mean precipitation simulated by the climate model of the i th month of reference period.

3. Study Area and Base Data

3.1. Study Area. Tangnaihai basin with a drainage area of 122,000 km² is located in the upstream of Yellow River in the western China, accounting for 15% of that of the Yellow River basin. Annual average runoff amount at the Tangnaihai cross section is 205.2 × 10⁸ m³, accounting for 40% of annual mean runoff amount of Yellow River basin. It is a semihumid region with good vegetation and less human activity. In the study, nine meteorological stations and seven hydrologic stations are involved. Figure 1 shows the location of the study area and gauging stations distribution.

3.2. Base Data. Five types of data, including hydrometeorology data, DEM, land use, soil distribution, and climate model data, are involved in the study. The details of data are as follows.

3.2.1. Hydrometeorology Data. Hydrometeorology data used in the study is the information of the elements influencing hydrologic cycle, such as rainfall, evaporation, runoff, and temperature. The basic data mainly comes from two sources: one is the 9 meteorological stations mentioned above which can provide precipitation, temperature, wind speed, solar radiation, relative humidity, and some other meteorological data; the other one is 7 hydrologic stations shown in Figure 2 which can provide precipitation, discharge, and evaporation. The length of the data series ranging from 1960 to 2012 is 53 years.

3.2.2. DEM. DEM is the basis for generating digital watershed system of Tangnaihai basin; in the paper, SRTM (Shuttle Radar Topography Mission) DEM with 90 m × 90 m resolution ratio, which is produced by NASA and NIMA, was utilized.

3.2.3. Land Use and Soil Distribution. Land use and soil distribution which are used to divide the whole basin into different HRUs are the basis of runoff yield calculation of SWAT model and play an important role in hydrologic model structure. In the paper, the dataset of WESTDC_Land_Cover_V.1.0 investigated by Chinese Academy of Sciences with the scale of 1 : 100,000 and the soil distribution data provided by Institute of Soil Science from the second national land survey were chosen to build SWAT model.

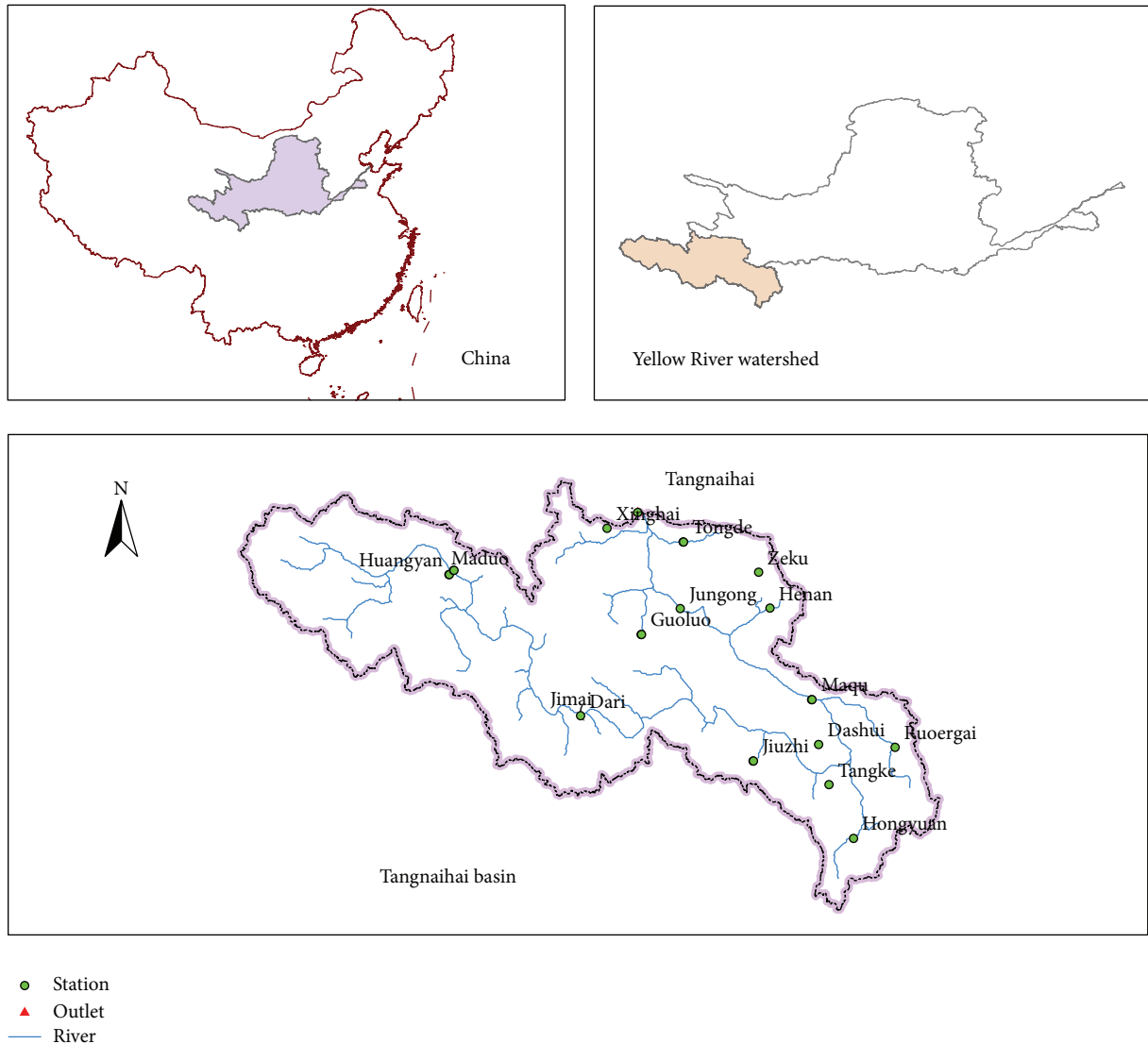


FIGURE 1: Location and hydrometeorological stations of the study area.

3.2.4. Climate Model Product. There are many dynamical climate model products under different climate scenarios and hypothesis released by IPCC AR5. It is unnecessary and unrealistic to analyze every climate model product in this study; one certain climate model product should be focused on instead. In this paper, several climate model products which suit the region where China locates were selected firstly. On the basis, the accuracy of predicted precipitation of the climate model products was analyzed, and the climate model product called BCC-CSM-1.1 is of good prediction effect and chosen as the basic data for conducting the evolution law of hydrologic extreme value of the upstream region of Yellow River basin. BCC-CSM-1.1 is provided by Beijing Climate Center of China Meteorological Administration with a space resolution $1.125^\circ \times 1.125^\circ$.

3.3. Durations of Hydrologic Selection. The longer durations (15 d, 30 d, and 60 d), instead of shorter durations (1 d,

3 d, 5 d, or 7 d), of hydrologic extreme were focused on in the paper. There are two reasons. First, flood volume of longer duration plays a control role in flood control the consequences for larger basin. The Tangnaihai basin is a large basin with drainage area of $122,000 \text{ km}^2$ and its basin flow concentration time is $>15 \text{ d}$. From this view, research on flood extreme of longer durations might be more meaningful for Tangnaihai basin; second, there are many reservoirs built or planned to be built, and flood volume of shorter durations will be influenced greatly by reservoir regulation, while that of longer durations will be maintain natural. Therefore, the time series of flood volume of shorter durations (1 d, 3 d, 5 d, or 7 d) are inconsistent and not suitable for frequency analysis of which theory is built on consistency of time series. In conclusion, evaluation the impact of climate change on hydrologic extreme of longer durations (15 d, 30 d, and 60 d) would be more meaningful and applicative.

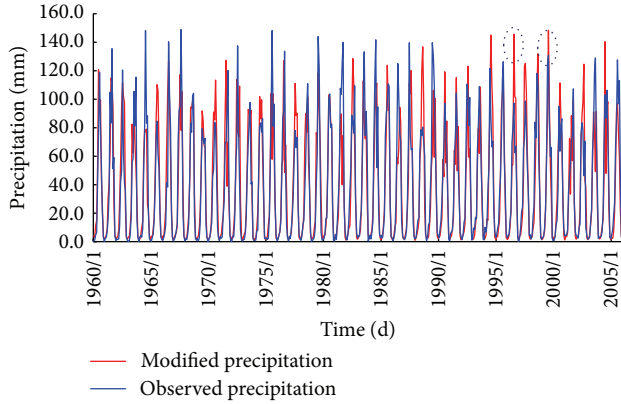


FIGURE 2: Results of precipitation correction (1960–2006) of the Tangnaihahi basin.

4. Results and Discussion

To reveal the revolution law of hydrologic extremes of the Tangnaihahi basin, the observed hydrologic time series from 1960 to 2010 and the predicted precipitation time series from 2011 to 2060 were used. In this paper, the years from 1960 to 2010 are defined as the measured phase while the years from 2011 to 2060 are denoted as the next 50 years.

4.1. Bias Correction of BCC-CSM-1.1. To correct systematic errors of simulated precipitation of BCC-CSM-1.1 of the Tangnaihahi basin, the correction model was built with linear regression relationship between observed and simulated precipitation in synchronized period. In the paper, the precipitation time series range from 1960 to 2006. Figure 2 shows the correction results.

According to the correction results, it is found that there was large correction error in the months of low-water seasons as the position of black circle shows in Figure 2, while the rest of correction results were of high accuracy. Since the paper focused on studying the precipitation extreme, the error of low-water months will have little effect. Therefore, the correction model built can be used to correct the simulation precipitation of BCC-CSM-1.1 of the Tangnaihahi basin.

4.2. Impact of Climate Change on Rainfall Extremes

4.2.1. Rainfall Extremes of Different Duration Analysis Based on Observed Data. The statistical law of rainfall extremes in the measured phase should be revealed first for uncovering the influences of climate on rainfall extremes. In the paper, the series of maximum value of annual rainfall extremes in different durations, such as 15 days, 30 days, and 60 days, was calculated by observed data and utilized to invest the statistical law of rainfall extremes. As mentioned above, the P-III distribution is suited for frequency analysis of hydrologic extremes in China. Therefore, the design rainfall of different durations (15 d, 30 d, and 60 d) of any probability can be deduced. Figure 3 shows the frequency curve of rainfall of different durations fitting by observed data. The parameters

TABLE 1: Results of parameters estimation of P-III distribution for the measured phase.

Duration (d)	Mean (mm)	C_v	C_s/C_v
15	80	0.20	3.5
30	130	0.19	3.5
60	215	0.17	3.5

TABLE 2: Design rainfall in different durations of different return periods for the measured phase (mm).

Duration (d)	Return period (a)			
	100	50	20	10
15	126	119	110	102
30	200	190	175	163
60	316	302	281	264

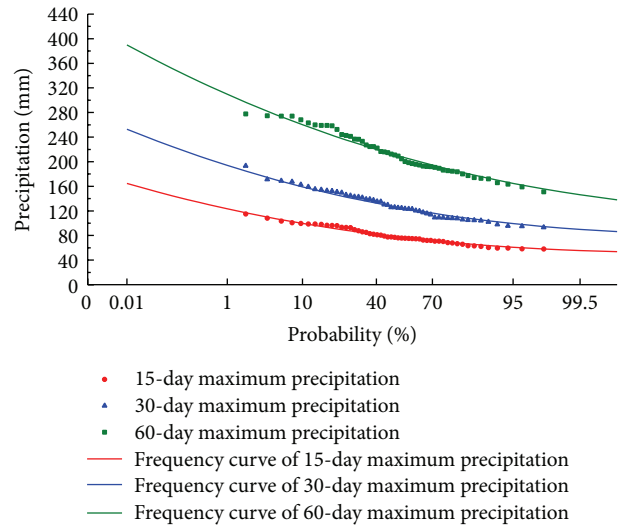


FIGURE 3: Frequency curve-fitting of rainfall extreme in different durations for the measured phase of Tangnaihahi basin.

estimation results of P-III distribution are listed in Table 1 while the design values for given probabilities are listed in Table 2.

4.2.2. Analysis of Rainfall Extremes of Different Durations with BCC-CSM-1.1. Time series of rainfall extremes in different durations (15 d, 30 d, and 60 d) in the next 50 years from 2011 to 2060 can be extracted according to the correction results of BCC-CSM-1.1. Similar to frequency analysis in the measured phase, the parameters estimation of P-III distribution and design value of different durations for next 50 years can be obtained. The corresponding frequency curves are shown in Figure 4, and the parameters estimation results are listed in Table 3 while the design values of several given probabilities are listed in Table 4.

TABLE 3: Results of parameters estimation of P-III distribution for the next 50 years.

Duration (d)	Mean (mm)	C_v	C_s/C_v
15	84	0.18	3.5
30	137	0.17	3.5
60	231	0.15	3.5

TABLE 4: Design rainfall in different durations of different return period for the next 50 years (mm).

Duration (d)	Return period (a)			
	100	50	20	10
15	128	122	113	105
30	201	192	179	168
60	332	318	297	280

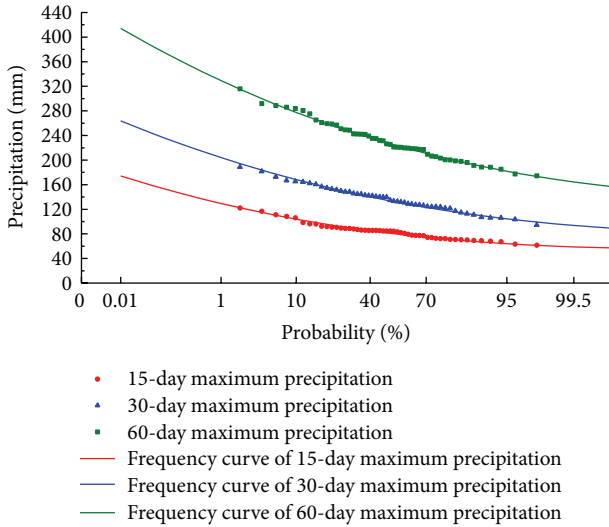


FIGURE 4: The frequency curves of 15-day, 30-day, and 60-day maximum rainfall of Tangnaihahi basin for the next 50 years.

4.2.3. Discussion about the Impact of Climate Change on Rainfall Extremes

(1) *Evaluation of Impact of Climate Change on Design Value.* To make a comparison between the rainfall extremes of Tangnaihahi basin in the measured phase and that in the next 50 years, the two frequency curves were drawn in the same diagram (Figures 5–7).

As shown in Figures 5–7, the frequency curves of annual maximum rainfall in different durations (15 d, 30 d, and 60 d) for the next 50 years are completely higher than that of the measured phase. It indicates that the annual maximum rainfall in different duration would increase with a certain degree due to climate change.

To quantitatively evaluate the impact of climate change on rainfall extreme, the design values of annual maximum in different duration for the measured phase and that for the next 50 year were calculated, and the corresponding results

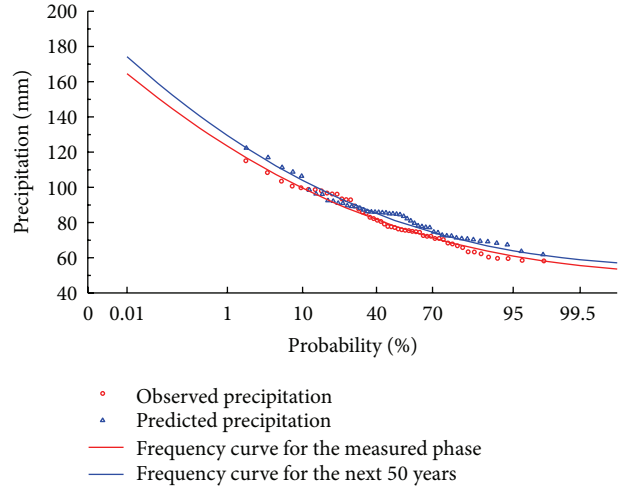


FIGURE 5: Frequency curves of maximum 15-day rainfall of Tangnaihahi basin in the measured phase and the next 50 years (2011–2060).

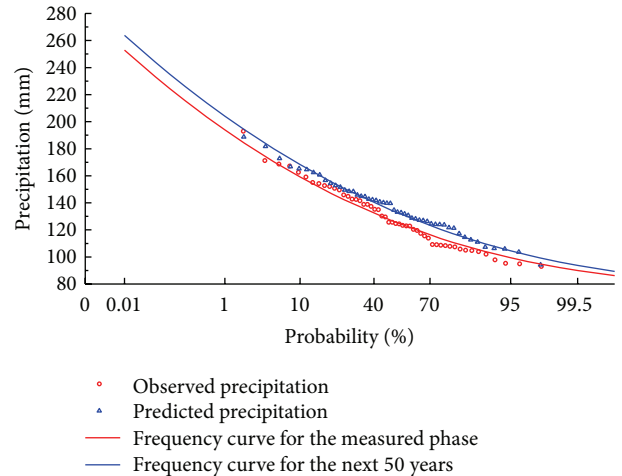


FIGURE 6: Frequency curves of maximum 30-day rainfall of Tangnaihahi basin in the measured phase and the next 50 years (2011–2060).

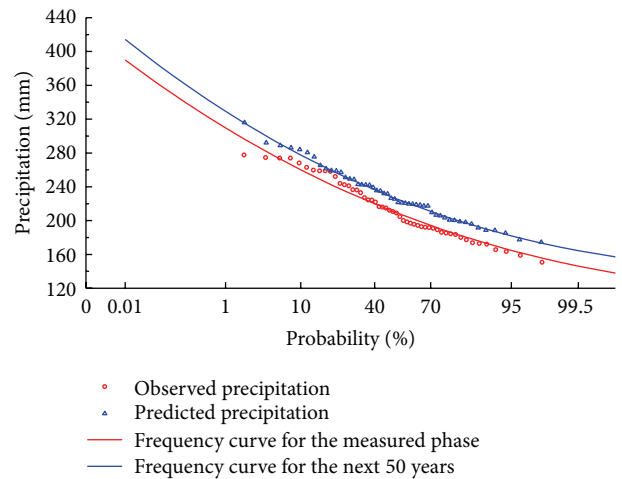


FIGURE 7: Frequency curves of maximum 60-day rainfall of Tangnaihahi basin in the measured phase and the next 50 years (2011–2060).

TABLE 5: Quantitative evaluation results of impact of climate change on annual rainfall extremes for several given probabilities.

Duration (d)	Items	Exceeding probability			
		1%	2%	5%	10%
15	Design value of observed series (mm)	126	119	110	102
	Design value of forecast series (mm)	128	122	113	105
	Change rate (%)	2	2	3	3
30	Design value of observed series (mm)	200	190	175	163
	Design value of forecast series (mm)	201	192	179	168
	Change rate (%)	1	1	2	3
60	Design value of observed series (mm)	316	302	281	264
	Design value of forecast series (mm)	332	318	297	280
	Change rate (%)	5	5	6	6

are listed in Table 5. As Table 5 shows, the change rates of design of 15 d, 30 d, and 60 d annual maximum rainfall, for the given probabilities (1%, 2%, 5% and 10%), are 2%-3%, 1%-3%, and 5%-6%, respectively. It indicates that the climate change has impacts on the rainfall extremes in the all durations (15 d, 30 d, and 60 d) of the Tangnaihah basin, and the change rates vary from 1% to 6%, but the influence degree of the rainfall extremes in study duration is slight.

(2) *Evaluation of Impact of Climate Change on Extreme Events of Given Probabilities.* What is the extreme event? There is no universal definition. According to the fourth assessment report of the IPCC [25], the climatic event with occurrence probability < 10% is defined as the extreme event. Inspired by the IPCC, the hydrologic event with occurrence probability < 10% is defined as the extreme event in the paper. To quantitatively evaluate the impact of climate change on extreme events, the number of extreme events exceeding the given probabilities (5%, 10%, and 20%) can be obtained according to the results of hydrologic frequency analysis and observed or predicted rainfall of different duration (Table 6).

The results of Table 6 show the following:

- (1) For 15-day rainfall, 4 extreme events exceed the given probability of 5% for the next 50 years, accounting for 80% of extreme events exceeding 5% in the whole period (measured phase and the next years, 1960–2060), while 8 extreme events exceed the given probability of 10% for the next 50 years, accounting for 63% of extreme events exceeding 20% in the whole period.
- (2) For 30-day rainfall, 2 extreme events exceed the given probability of 5% for the next 50 years, accounting for 67% of extreme events exceeding 5% in the whole period, while 11 extreme events exceed the given probability of 10% for the next 50 years, accounting

TABLE 6: Number of extreme events exceeding given probabilities for the measured phase and the next 50 years.

Duration (d)	Time range	Exceeding probability		
		5%	10%	20%
15	1960–2010	1	3	11
	2011–2060	4	5	8
30	1960–2010	1	4	9
	2011–2060	2	4	11
60	1960–2010	0	5	11
	2011–2060	5	7	13

for 50% of extreme events exceeding 10% in the whole period.

- (3) For 60-day rainfall, 5 extreme events exceed the given probability of 5% for the next 50 years, accounting for 100% of extreme events exceeding 5% in the whole period, while 13 extreme events exceed the given probability of 10% for the next 50 years, accounting for 58% of extreme events exceeding 10% in the whole period. Generally, the number of extreme events exceeding given probability in the next 50 years is more than that in the measured phase. In other words, the probability of extreme events would increase with different degree in the next 50 years.

On this basis, probability density function of the number of extreme events can be obtained in pattern of the Poisson distribution. Figures 8 and 9 show the diagrams of probability density function of the number of extreme events for the measured phase and the next 50 years. It indicates that the number of extreme events exceeding smaller probability will increase while that exceeding larger probability would decrease. In other words, the extreme events will be more frequent in the next 50 years.

4.3. Impact of Climate Change on Flood Volume Extreme with Different Durations

4.3.1. Model Calibration and Validation

(1) *Model Construction.* The Tangnaihah basin was divided into 27 subbasins according to the DEM data; on this basis, the basin was divided into 105 HRUs further according to the land use and soil distribution. The subbasins of the Tangnaihah are shown in Figure 10.

(2) *Model Calibration and Validation.* In the paper, the observed streamflows for the period of 1995–2004 were used for calibration, and those from 2005 to 2007 were used for the validation of the SWAT model. According to the simulated results of these runoff process mentioned above, the Nash-Sutcliffe coefficient (NS) and deterministic coefficient (R^2) which denote the accuracy of model can be obtained. The NS and R^2 are 0.76 and 0.80, respectively, in the calibration period while they are 0.75 and 0.80, respectively, in the validation period. It indicates that the SWAT model built

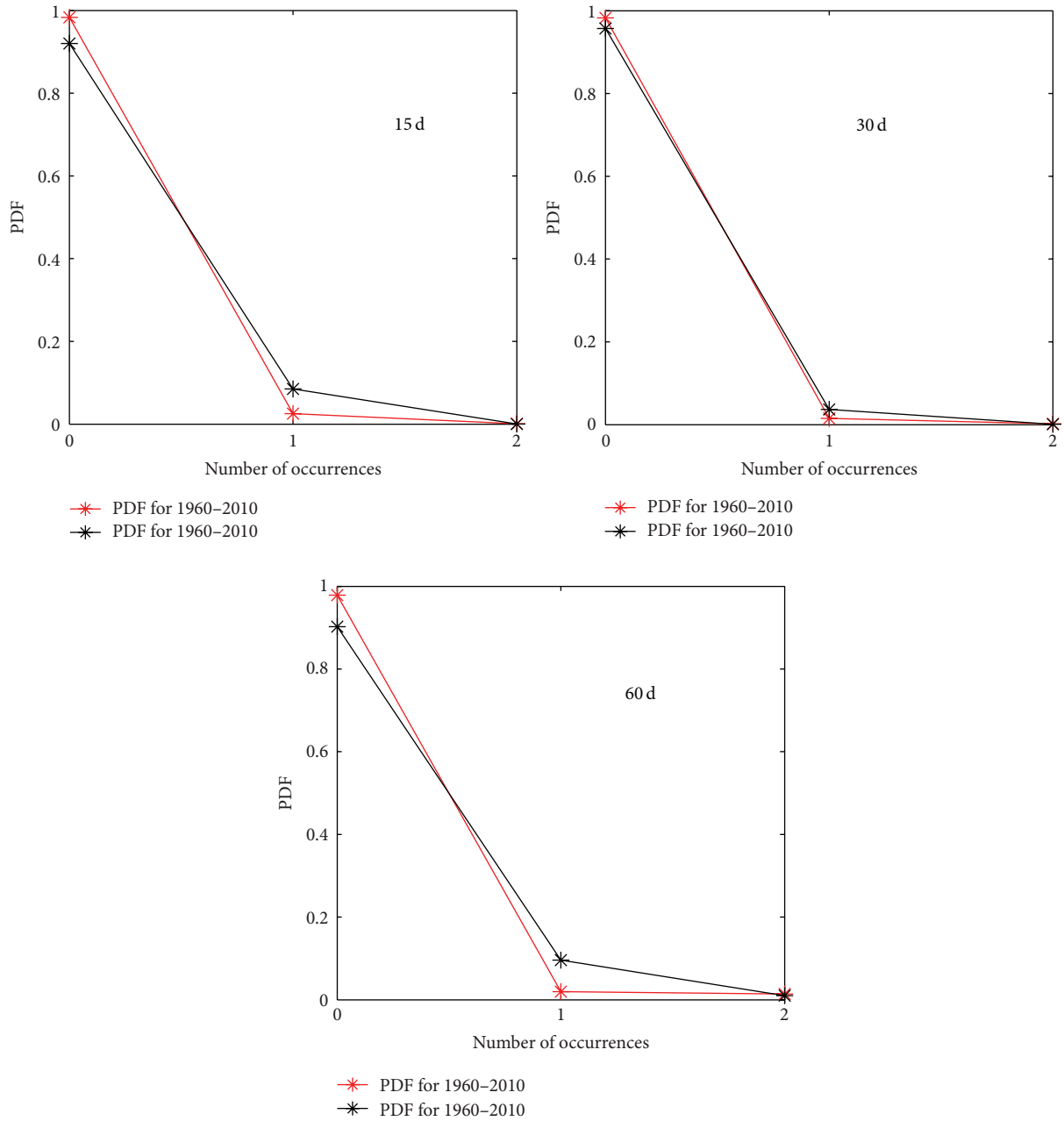


FIGURE 8: Probability density diagram of the precipitation exceeding probability of 5% for the measured phase and the next 50 years of the Tangnaihahi basin.

is of good accuracy and can be adopted to simulate the rainfall-runoff in the study area. Taking several runoff processes as an example, Figures 11 and 12 show the simulation results.

4.3.2. Design Rainfall in Different Durations Deduced for Next 50 Years. Long duration rainfall extremes of certain given probabilities (1%, 2%, 5%, and 10%) of the Tangnaihahi basin for the next 50 years were deduced in Section 4.2.2. However, the results are not enough to meet the requirements for deducing long duration flood volume extremes by SWAT,

and the design rainfall process is also needed. Therefore, the design rainfall process should be deduced firstly.

The basic idea and procedure to deduce design rainfall process in different given probabilities are as follows: (1) selecting one typical storm process with certain principles; (2) magnifying it according to the design rainfall value and keeping the maximum rainfall of given duration and probability of magnified typical storm process equal to the design rainfall of corresponding duration and probability. In the paper, the storm process that occurred from 28/5/1989 to 26/7/1989 was selected as the typical storm. According to

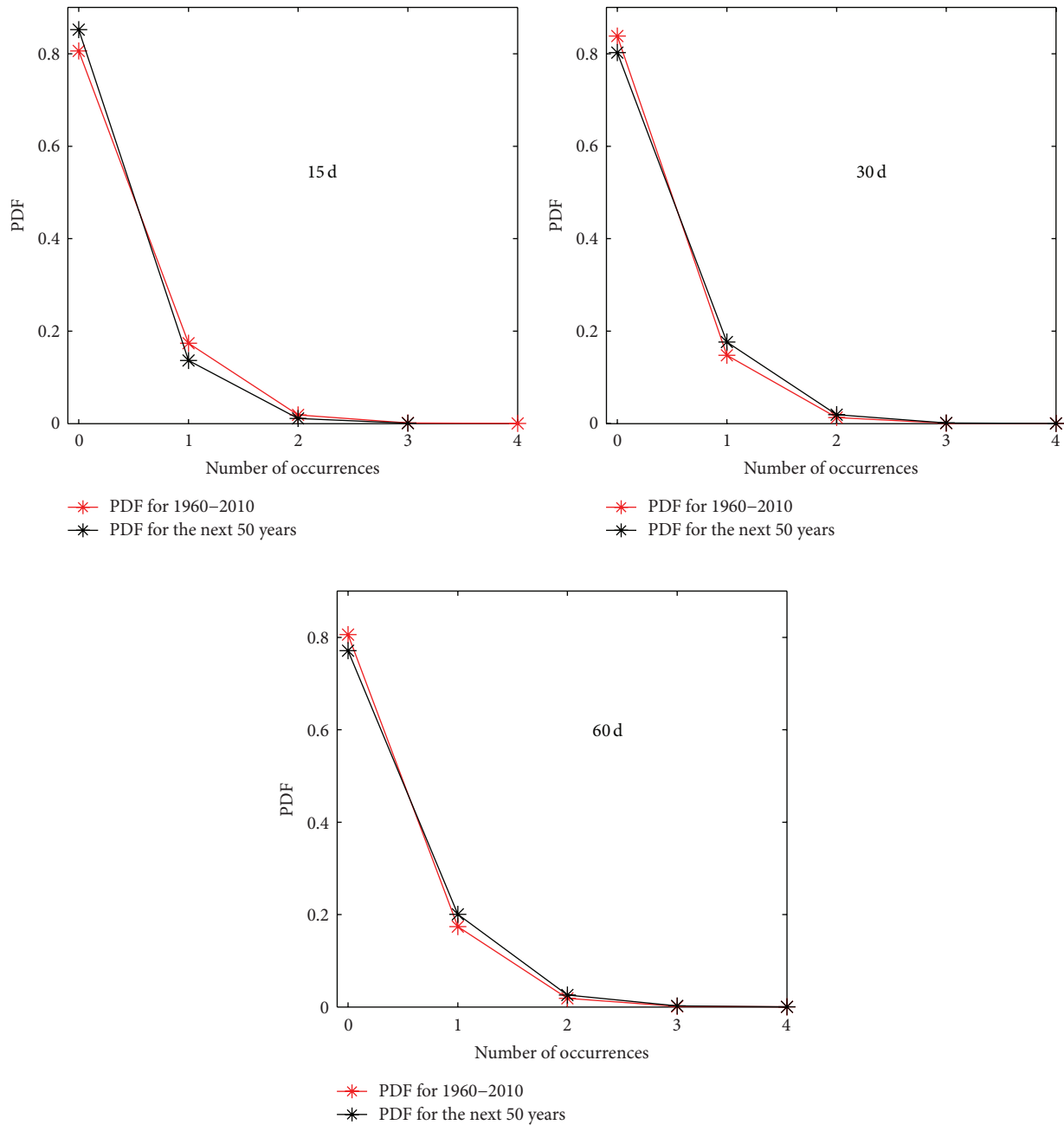


FIGURE 9: Probability density diagram of the rainfall extreme event exceeding probability of 20% for the measured phase and the next 50 years of Tangnaihahi basin.

the magnified method, design rainfall process of different return periods (100 a, 50 a, 20 a, and 10 a) can be obtained. Taking return period of 100 a as an example, Figure 13 shows the process of rainfall.

Similarly, design rainfall process of different return periods (100 a, 50 a, 20 a, and 10 a) for the measured phase can be obtained. Taking return period of 100 a as an example, Figure 14 shows the process of rainfall.

4.3.3. Design Flood Volume in Different Durations Deduced for Next 50 Years. According to the design rainfall process

of given probability, the flood hydrography of corresponding probability was deduced, respectively, by running the SWAT. On this basis, the long duration flood volume of different probabilities for the next 50 years can be obtained. The results are listed in Table 7.

4.3.4. Discussion on Impact of Climate Change on Flood Volume Extreme. Taking the design rainfall process in different probability as input condition for SWAT, the design flood process in corresponding probability can be obtained by running the model. In the paper, design flood process of

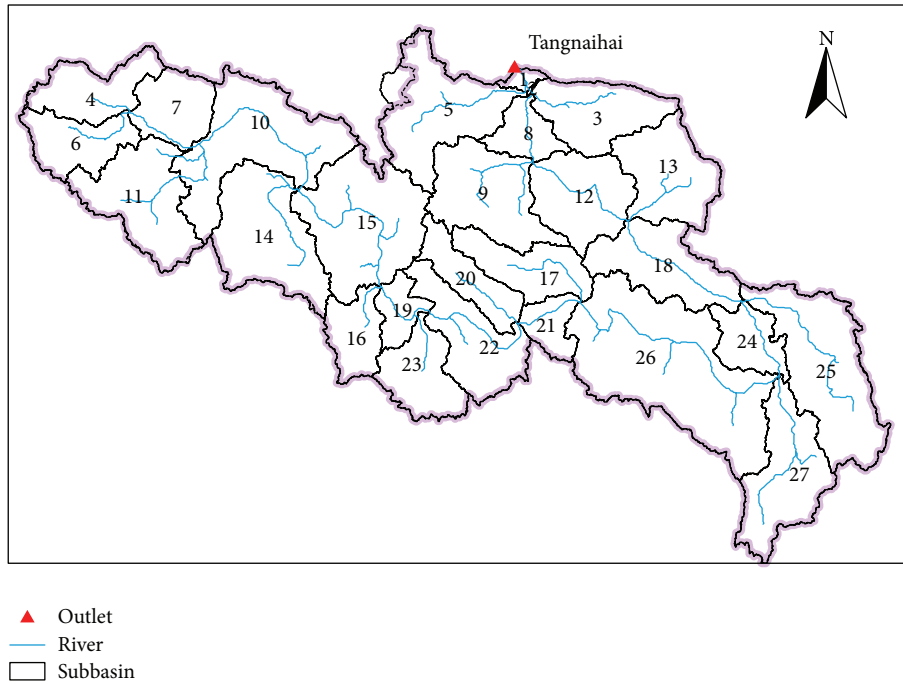


FIGURE 10: Subbasins of Tangnaihai basin.

TABLE 7: Long duration flood volume of different probabilities for the next 50 years of Tangnaihai basin.

Duration (d)	Return period (a)			
	100	50	20	10
15	126	119	110	102
30	200	190	175	163
60	316	302	281	264

TABLE 8: Change rates of design flood volume in different durations of given probabilities (%).

Duration (d)	Return period (a)			
	100	50	20	10
15	3	3	3	1
30	3	2	3	1
60	3	5	6	5

different return period including 100 a, 50 a, 20 a, and 10 a was simulated. Figures 15–18 show the design hydrographs which are of four return periods (100 a, 50 a, 20 a, and 10 a) for the measured phase and the next 50 years, respectively.

According to Figures 15–18, it is obvious that the design flood hydrograph is higher for the next 50 years than that of the measured phase. It indicates that the flood volume extremes show an increasing trend in the Tangnaihai basin. To take a close investigation into the rising trend and make a quantitative estimation, change rates of flood volume in different durations of four kinds of probabilities (1%, 2%, 5%, and 10%) are calculated and listed in Table 8.

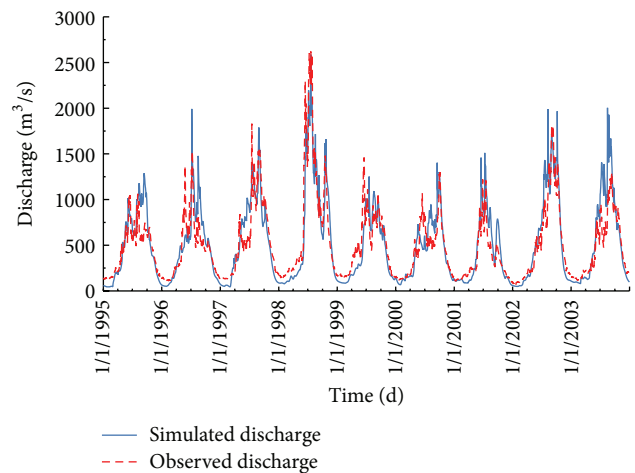


FIGURE 11: Observed and simulated hydrographs of Tangnaihai cross section in calibration period.

According to Table 8, the increasing rates of 15-day flood volume for different return period vary from 1% to 3%; the increasing rates of 30-day flood volume for different return period vary from 1% to 3%; and the increasing rates of 60-day flood volume for different return period vary from 3% to 6%. It indicates that the increasing rates of long duration flood volume of Tangnaihai basin is less than 10%. In other words, the flood volume extremes in long duration of Tangnaihai basin increase slightly in the next 50 years.

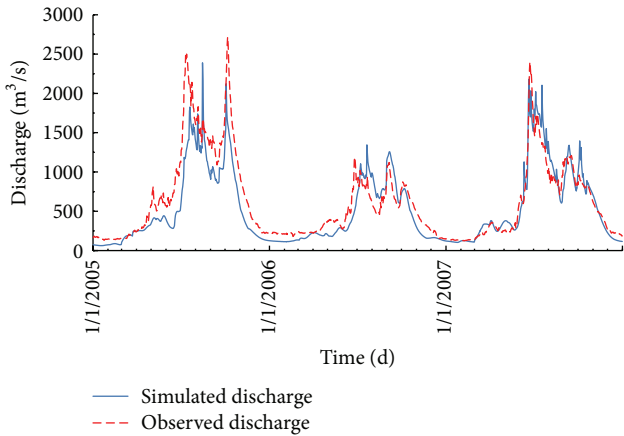


FIGURE 12: Observed and simulated hydrographs of Tangnaihai cross section in validation period.

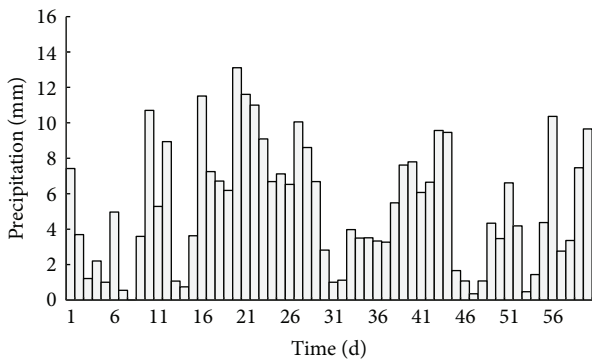


FIGURE 13: The process of 100-year design rainfall of Tangnaihai basin for the next 50 years.

5. Conclusions

To study the impact of climate change on hydrologic extremes in the Tangnaihai basin which locates in the upstream of Yellow River, the BCC-CSM-1.1 released by IPCC 5 was used to forecast rainfall in the next 50 years (2011–2060). On this basis, according to the observed hydrologic data series, the evolution law of long duration hydrologic extremes of Tangnaihai basin is revealed. Main conclusions can be achieved as follows.

- (1) It indicates that the values of long duration (15 d, 30 d, and 60 d) rainfall extremes of Tangnaihai basin will rise by slightly increasing rate in the next 50 years. According to analysis results of rainfall extremes in different durations, 15-day design rainfall of given probabilities (1%, 2%, 5%, and 10%) will increase by 2%–3%; similarly, 30-day design rainfall will increase by 1%–3% and 60-day design rainfall will increase by 5%–6%, respectively. It is obvious that the increasing rates of rainfall extremes in given probabilities are less than 10%; in other words, the rainfall extremes of the Tangnaihai basin would increase with a slight degree.

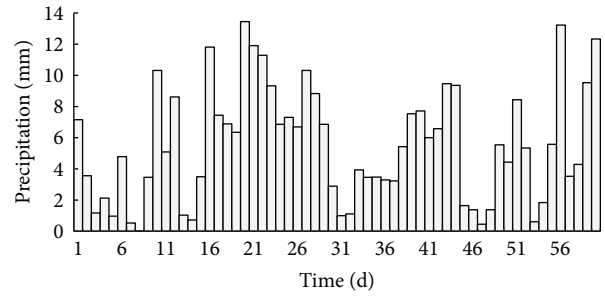


FIGURE 14: The process of 100-year design rainfall of Tangnaihai basin for the measured phase.

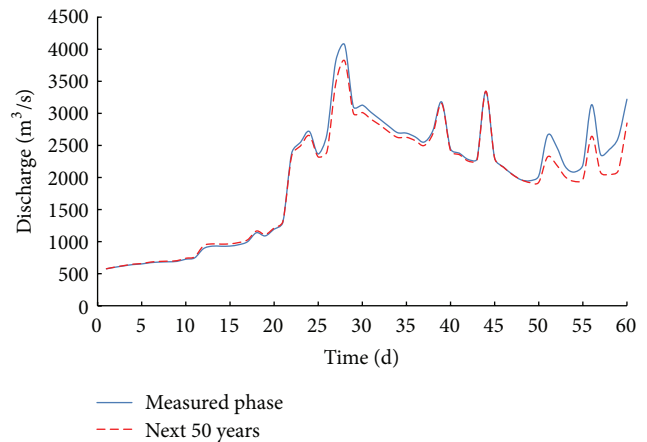


FIGURE 15: 100-year flood hydrograph for the measured phase and the next 50 years of Tangnaihai basin.

- (2) It indicates that the number of extreme events exceeding smaller probability will increase for the next 50 years. According to the analysis of number of extreme events exceeding given probability, it is obvious that the extreme events of long duration rainfall exceeding given probabilities (5%, 10%, and 20%) will get more frequent.
- (3) It indicates that the values of long duration (15 d, 30 d, and 60 d) flood volume extremes of Tangnaihai basin will rise by slightly increasing rate in the next 50 years. On the hypothesis that rainfall of given frequency could generate the flood of the same frequency, SWAT model was used to deduce design flood with the import of design rainfall for the next 50 years, and the long flood volume extremes were achieved. According to the analysis of results of flood volume extremes in different duration, 15-day design flood volume of given probabilities (1%, 2%, 5%, and 10%) is increasing by 1%–3% based on BCC-CSM-1.1; similarly, 30-day design flood volume is increasing by 1%–3% and 60-day design flood volume is increasing by 3%–6%, respectively. It obvious that the increasing rate of flood volume extremes in given probability is less than 10%, in other words, the flood volume

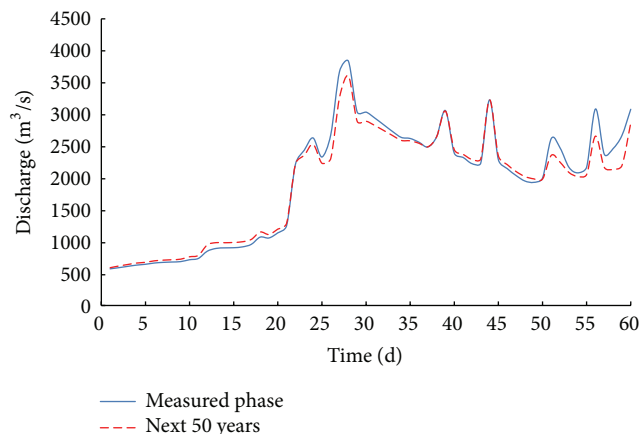


FIGURE 16: 50-year flood hydrograph for the measured phase and the next 50 years of Tangnaihai basin.

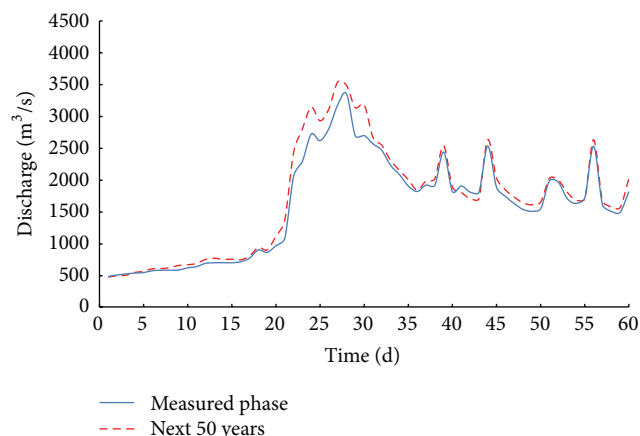


FIGURE 17: 20-year flood hydrograph for the measured phase and the next 50 years of Tangnaihai basin.

extremes of the Tangnaihai basin would increase with a slight degree.

Generally, the long duration hydrologic extremes of the Tangnaihai basin in Yellow River basin would increase by a slight degree in the next 50 years. The conclusions were addressed on the basis of BCC-CSM-1.1. However, if several more suitable climate change model products were adopted, the conclusions on impact of climate change in study area will be more reliable. To improve the study, we will try more GCM outputs and continue in-depth studies on the same theme in the future.

Competing Interests

The authors declare that there are no competing interests regarding the publication of this paper.

Authors' Contributions

The studies were designed by Jun Wang, Zhongmin Liang, Dong Wang, Tian Liu, and Jing Yang. Specifically, Jun Wang

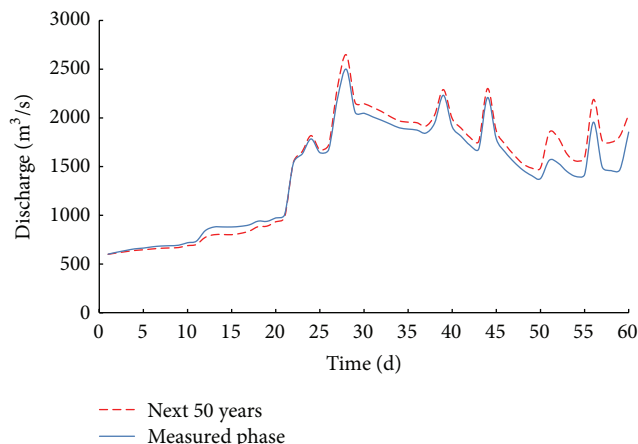


FIGURE 18: 10-year flood hydrograph for the measured phase and the next 50 years of Tangnaihai basin.

and Zhongmin Liang performed the studies and analyzed the data, Dong Wang processed the precipitation simulated by climate model, Tian Liu built the SWAT model and calculated design flood, and Jing Yang helped to hydrologic frequency analysis and helped refine the charts and polish the paper.

Acknowledgments

This study was supported by the Public Welfare Industry Special Fund Project of Ministry of Water Resources of China (nos. 201301066 and 201401034), the National Natural Science Foundation of China (nos. 51109054, 51179046, and 51479061), National Science and Technology Support Plan (no. 2013BAB06B01), and Excellent Ph.D. Training program (no. 2015B05514).

References

- [1] N. S. Christensen, A. W. Wood, N. Voisin, D. P. Lettenmaier, and R. N. Palmer, "The effects of climate change on the hydrology and water resources of the Colorado River basin," *Climatic Change*, vol. 62, no. 1-3, pp. 337-363, 2004.
- [2] M. K. Jha and P. W. Gassman, "Changes in hydrology and streamflow as predicted by a modelling experiment forced with climate models," *Hydrological Processes*, vol. 28, no. 5, pp. 2772-2781, 2014.
- [3] C. Yang, Z. Yu, Z. Hao, J. Zhang, and J. Zhu, "Impact of climate change on flood and drought events in Huaihe River Basin, China," *Hydrology Research*, vol. 43, no. 1-2, pp. 14-22, 2012.
- [4] Z. Yu, T. Yang, and F. W. Schwartz, "Water issues and prospects for hydrological science in China," *Water Science and Engineering*, vol. 7, no. 1, pp. 1-4, 2014.
- [5] A. C. Horrevoets, H. H. G. Savenije, J. N. Schuurman, and S. Graas, "The influence of river discharge on tidal damping in alluvial estuaries," *Journal of Hydrology*, vol. 294, no. 4, pp. 213-228, 2004.
- [6] N. L. Poff, J. D. Allan, M. B. Bain et al., "The natural flow regime: a paradigm for river conservation and restoration," *BioScience*, vol. 47, no. 11, pp. 769-784, 1997.

- [7] N. Y. Krakauer and I. Fung, "Mapping and attribution of change in streamflow in the coterminous United States," *Hydrology and Earth System Sciences*, vol. 12, no. 4, pp. 1111–1120, 2008.
- [8] K. Stahl, H. Hisdal, J. Hannaford et al., "Streamflow trends in Europe: evidence from a dataset of near-natural catchments," *Hydrology and Earth System Sciences*, vol. 14, no. 12, pp. 2367–2382, 2010.
- [9] F. H. S. Chiew, J. Teng, J. Vaze et al., "Estimating climate change impact on runoff across southeast Australia: method, results, and implications of the modeling method," *Water Resources Research*, vol. 45, no. 10, Article ID W10414, 2009.
- [10] A. Senatore, G. Mendicino, G. Smiatek, and H. Kunstmann, "Regional climate change projections and hydrological impact analysis for a Mediterranean basin in Southern Italy," *Journal of Hydrology*, vol. 399, no. 1-2, pp. 70–92, 2011.
- [11] M. V. Shabalova, W. P. A. Van Deursen, and T. A. Buishand, "Assessing future discharge of the river Rhine using regional climate model integrations and a hydrological model," *Climate Research*, vol. 23, no. 3, pp. 233–246, 2003.
- [12] Q. Liu and B. Cui, "Impacts of climate change/variability on the streamflow in the Yellow River Basin, China," *Ecological Modelling*, vol. 222, no. 2, pp. 268–274, 2011.
- [13] C. Cunnane, "Statistical distribution for flood frequency analysis," Operational Hydrology Report (WMO) 781, 1989.
- [14] D. R. Maidment, *Handbook of Hydrology*, McGraw-Hill, New York, NY, USA, 1992.
- [15] Z. M. Liang, *Hydrologic Analysis and Calculation*, China Water Power Press, 2013.
- [16] Y. F. Chen, Ed., *Engineering Hydrology and Flood Control Calculation and Water Resources Analysis*, China Water & Power Press, 2013.
- [17] J. G. Arnold, R. Srinivasan, R. S. Muttiah, and J. R. Williams, "Large area hydrologic modeling and assessment part I: model development," *Journal of the American Water Resources Association*, vol. 34, no. 1, pp. 73–89, 1998.
- [18] S. L. Neitsch, J. G. Arnold, J. R. Kiniry, and J. R. Williams, *SWAT User Manual, Version 2005*, Grassland Soil and Water Research Laboratory, Temple, Tex, USA, 2005.
- [19] J. G. Arnold, J. R. Kiniry, R. Srinivasan, J. R. Williams, E. B. Haney, and S. L. Neitsch, *SWAT Input/Output File Documentation, Version 2009*, Grassland Soil and Water Research Laboratory, Temple, Tex, USA, 2011.
- [20] S. L. Neitsch, J. G. Arnold, J. R. Kiniry, and J. R. Williams, "SWAT user manual, version 2009," Texas Water Resources Institute Technical Report, Texas A&M University, College Station, Tex, USA, 2011.
- [21] USDA Soil Conservation Service, *National Engineering Handbook. Hydrology Section 4*, chapter 4–10, 1972.
- [22] S. Bergström, B. Carlsson, M. Gardelin, G. Lindström, A. Pettersson, and M. Rummukainen, "Climate change impacts on runoff in Sweden assessments by global climate models, dynamical down-scaling and hydrological modelling," *Climate Research*, vol. 16, pp. 101–112, 2001.
- [23] L. P. Graham, J. Andréasson, and B. Carlsson, "Assessing climate change impacts on hydrology from an ensemble of regional climate models, model scales and linking methods—a case study on the Lule River basin," *Climatic Change*, vol. 81, no. 1, pp. 293–307, 2007.
- [24] C. Teutschbein and J. Seibert, "Bias correction of regional climate model simulations for hydrological climate-change impact studies: review and evaluation of different methods," *Journal of Hydrology*, vol. 456–457, pp. 12–29, 2012.
- [25] IPCC, *Climate Change 2007: The Physical Basis. Contribution of Working Group I to the Fourth Assessment Report of the IPCC*, Cambridge University Press, New York, NY, USA, 2007.

Research Article

Satellite Retrieval of Surface Evapotranspiration with Nonparametric Approach: Accuracy Assessment over a Semiarid Region

Xin Pan,^{1,2} Yuanbo Liu,¹ and Xingwang Fan¹

¹Key Laboratory of Watershed Geographic Sciences, Nanjing Institute of Geography and Limnology, Chinese Academy of Sciences, 73 East Beijing Road, Nanjing 210008, China

²University of Chinese Academy of Sciences, 19 Yuquan Road, Beijing 100049, China

Correspondence should be addressed to Yuanbo Liu; ybliu@niglas.ac.cn

Received 2 December 2015; Revised 7 March 2016; Accepted 18 April 2016

Academic Editor: Iftekhar Ahmed

Copyright © 2016 Xin Pan et al. This is an open access article distributed under the Creative Commons Attribution License, which permits unrestricted use, distribution, and reproduction in any medium, provided the original work is properly cited.

Surface evapotranspiration (ET) is one of the key surface processes. Reliable estimation of regional ET solely from satellite data remains a challenge. This study applies recently proposed nonparametric (NP) approach to retrieve surface ET, in terms of latent heat flux (LE), over a semiarid region. The involved input parameters are surface net radiation, land surface temperature, near-surface air temperature, and soil heat flux, all of which are retrievals or products of the Moderate-Resolution Imaging Spectroradiometer (MODIS). Field observations are used as ground references, which were obtained from six eddy covariance (EC) sites with different land covers including desert, Gobi, village, orchard, vegetable field, and wetland. Our results show that the accuracy of LE retrievals varies with EC sites with a determination of coefficient from 0.02 to 0.76, a bias from -221.56 W/m^2 to 143.77 W/m^2 , a relative error from 8.82% to 48.35%, and a root mean square error from 67.97 W/m^2 to 239.55 W/m^2 . The error mainly resulted from the uncertainties from MODIS products or the retrieval of net radiation and soil heat flux in nonvegetated region. It highlights the importance of accurate retrieval of the input parameters from satellite data, which are the ongoing tasks of remote sensing community.

1. Introduction

Evapotranspiration (ET) includes evaporation from various land surfaces and transpiration from vegetation [1]. ET is interchangeable to the associated latent energy (LE) [2]. It is a key land surface process in regulating regional hydrological and climatic characteristics. As the only way back to the atmosphere, global land ET returns about 60% of annual land precipitation to the atmosphere [3]. Accurate estimation of ET is important for regional water resources management, especially in arid regions.

ET is intrinsically difficult to measure and predict especially at a large spatial scale. Various approaches are proposed to estimate ET in succession after the 18th century, including the Penman evaporation equation [4], the Penman-Monteith (P-M) combination equation [5], and the Priestley and Taylor approach [6]. Traditional measurement or estimation of LE

is mostly applicable at a point-scale [7–9], including eddy covariance (EC) techniques [10]. However, representativeness of the point-scale measurement for a large area is generally problematic, and the dense coverage of point measurements is not feasible [11].

Alternatively, remote sensing technology can efficiently solve the representation limitation of the point measurement. However, it cannot observe LE directly, whereas it provides retrievals of geophysical parameters to estimate LE at a regional scale [12]. Several retrieval algorithms appeared in the last two decades [13, 14], including the triangle approach [15–17], the simplified surface energy balance index (S-SEBI) [18], the surface energy balance system (SEBS) [19], the three-temperature model [20–22], the MOD16 algorithm [23, 24], and other P-M remote sensing methods [25, 26]. They are widely applied to estimate regional or global ET from remotely sensed data [25–31]. The existing algorithms have

a relative error from 10% to 40% [32, 33] in their validation sites. For example, Gillies et al. [34] used aircraft scanner data and the triangle approach to retrieve LE in an area covered with grasslands, steppe-shrub, and tall-grass prairie. The LE retrievals had a root mean square error (RMSE) value of 22~55 W/m² and a relative error (RE) of 10%~30%, in reference to field measures by EC techniques and Bowen-ratio approaches. Verstraeten et al. [28] used the advanced very high resolution radiometer (AVHRR) and the S-SEBI approach to retrieve LE in forestland. This achieved a RMSE (RE) of 35 W/m² (24%), compared to EC measures. Su [19] used the Moderate-Resolution Imaging Spectroradiometer (MODIS) data and the SEBS approach to estimate LE in wheat, corn, and rainforest areas. The LE retrievals had a RE of 25%, compared to EC measures. Xiong and Qiu [22] used the three-temperature approach and Landsat Thematic Mapper (TM) data to retrieve instantaneous LE in grassland and hills. Relative to Bowen ratio systems, LE had a RE of 4.65%~100% or 0.02~0.20 mm h⁻¹ during the satellite overpassing time. Mu et al. [23] evaluated the MOD16 products and reported an average bias (RE) of 0.31 mm day⁻¹ (24.1%) for daily ET at FLUXNET-EC sites. Zhang et al. [25] applied normalized difference vegetation index- (NDVI-) based ET algorithm to assess global terrestrial LE using AVHRR GIMMS NDVI data. The daily results had a favorable accuracy with RMSE of about 10~40 W/m² at 34 flux tower sites. Similarly, Leuning et al. [26] introduced a remotely sensed leaf area index- (LAI-) based P-M algorithm to calculate regional daily average evaporation using MODIS LAI products. At 15 flux sites globally, the systematic RMSE in daytime mean evaporation was in the range of 0.09~0.50 mm day⁻¹, whereas the unsystematic component was in the range of 0.28~0.71 mm day⁻¹.

A nonparametric approach (NP) has been recently proposed for estimating surface evapotranspiration [35]. It uses net radiation, surface air temperature, land surface temperature, and soil heat flux as the inputs, without the need of parameterizing surface resistance. All the necessary inputs are measurable, offering a novel but simple approach for practical use. The approach has been validated at 24 EC sites, yet it was not tested with remote sensing application. This paper applies the NP approach to estimate regional LE covering different surfaces, evaluates the accuracy of LE retrievals from MODIS data only, and identifies the error sources which are useful for improving retrieval accuracy.

2. Methodology

2.1. The Nonparametric Evapotranspiration Approach. Surface net radiation (R_n) is the net amount of radiation entering and leaving the Earth's surface. A part of R_n is transformed into surface soil heat flux (G_s), and another part controls LE and sensible heat flux (H_s). In NP approach, a homogeneous terrestrial ground surface layer is assumed for a macrostate system, and Hamiltonian (potential energy plus kinetic energy) is the total energy of this system. R_n serves as the potential energy, whereas G_s , H_s , and LE serve as kinetic energy. The land surface temperature (LST) serves

as a generalized coordinate in this system. The approach calculates the partial differential equations of Hamiltonian with LST (T_s). The final forms are [35]

$$\begin{aligned} H_{T_s} &= \frac{\gamma}{\Delta + \gamma} (R_n - G_s) + \varepsilon \sigma (T_s^4 - T_a^4) - G_s \ln \left(\frac{T_s}{T_a} \right), \\ LE_{T_s} &= \frac{\Delta}{\Delta + \gamma} (R_n - G_s) - \varepsilon \sigma (T_s^4 - T_a^4) + G_s \ln \left(\frac{T_s}{T_a} \right), \end{aligned} \quad (1)$$

where ε is land surface emissivity (LSE), T_a is near-surface air temperature (AT), Δ is the slope of saturated vapor pressure at temperature T_a , γ is the psychrometric constant, and σ is the Stefan-Boltzmann's constant ($5.67 \times 10^{-8} \text{ Wm}^{-2} \text{ K}^{-4}$). γ can be estimated by the near-surface pressure (P).

2.2. Retrieval Algorithms for Net Radiation and Soil Heat Flux as Inputs to the NP Approach. Bisht's R_n retrieval algorithm [36] is simple and accurate to estimate instantaneous R_n over large heterogeneous areas under clear sky days. R_n is calculated in Bisht's algorithm:

$$\begin{aligned} R_n &= (1 - \alpha) R_{sd} + \varepsilon \sigma (\varepsilon_a T_a^4 - T_d^4), \\ R_{sd} &= \frac{S_0 \cos^2 \theta}{d}, \\ d &= 1.085 \cos \theta + e_0 (2.7 + \cos \theta) \times 10^{-3} + 0.1, \\ \varepsilon &= 0.273 + 1.778 \varepsilon_{31} - 1.807 \varepsilon_{31} \varepsilon_{32} - 1.037 \varepsilon_{32} \\ &\quad + 1.774 \varepsilon_{32}^2, \\ \varepsilon_a &= \begin{cases} 1 \\ - \left(1 + \frac{46.5 e_0}{T_a} \right) \exp \left\{ - \left(1.2 + 3 \cdot \frac{46.5 e_0}{T_a} \right)^{1/2} \right\} \end{cases}, \\ e_0 &= 6.11 \exp \left[\frac{L_v}{R_v (1/273 - 1/T_d)} \right], \end{aligned} \quad (2)$$

where S_0 is the solar constant at the top of the atmosphere (about 1367 W/m²), α is the surface albedo, θ is the solar zenith angle (SZA), e_0 is the water vapor pressure, ε_a is the air emissivity, and ε_{31} and ε_{32} denote the emissivity in bands 31 and 32 of MODIS, respectively. R_{sd} is the downwell shortwave radiation. L_v is the latent heat of vaporization ($2.5 \times 10^6 \text{ J/kg}$), R_v is the gas constant for water vapor ($461 \text{ J kg}^{-1} \text{ K}^{-1}$), and T_d is the dew point temperature at screen level. For the surface albedo, it is derived by the following equation [37]:

$$\begin{aligned} \alpha &= 0.160 \alpha_1 + 0.291 \alpha_2 + 0.243 \alpha_3 + 0.116 \alpha_4 + 0.112 \alpha_5 \\ &\quad + 0.081 \alpha_7, \end{aligned} \quad (3)$$

where α_1 , α_2 , α_3 , α_4 , α_5 , and α_7 are the nadir BRDF-adjusted albedos in bands 1, 2, 3, 4, 5, and 7 of MODIS, respectively.

At long time scales, G_s is commonly assumed to be negligible. But at subdaily scale, the G_s varies with the time

of day, and the values of G_s are not always negligible. It can be parameterized with the following equation [38]:

$$G_s = 0.583 \exp(-2.13\text{NDVI}) R_n. \quad (4)$$

Obviously, G_s is regarded as a function of normalized difference vegetation index (NDVI) and R_n .

2.3. Correction of EC Measures Used as Reference for Accuracy Assessment. Although EC is the most accurate technique to measure the turbulent fluxes of sensible and latent heat, the energy balance can not be closed with EC data at the Earth surface with a closure of the energy balance of approximately 80% [39, 40]. In addition, relative to the fluctuations of LE accuracy, H_s is measured in more reliable accuracy [41–43]. So it is necessary to correct LE directly measured by EC for validation.

A preferred method can be derived from energy balance [44, 45]. On the large-scale homogeneous surface and steady-state condition, the corrected LE (ERLE) is

$$\text{ERLE} = R_n - G_s - H_{\text{EC}}, \quad (5)$$

where H_{EC} is H_s measured by EC. The ERLE is the reference of validation for remote sensing retrieved LE (RSLE).

2.4. Metrics for Accuracy Assessment. The linear regression approach is used to describe the accordance between RSLE and ERLE. The determination of coefficient (R^2), slope, and intercept of the linear fit between RSLE and ERLE are subsequently obtained. The accordance is more satisfactory when the regression line is nearer to 1:1 line and R^2 is higher.

Their definitions are described as follows [46]:

$$\begin{aligned} R^2 &= 1 - \frac{\sum_{i=1}^n (s_i - o_i)^2}{\sum_{i=1}^n (s_i - \bar{o})^2}, \\ \text{Slope} &= \frac{\sum_{i=1}^n s_i \cdot (o_i - \bar{o})^2}{\sum_{i=1}^n (o_i - \bar{o})^2}, \\ \text{Intercept} &= \frac{\sum_{i=1}^n (s_i - \text{Slope} \cdot o_i)}{n}, \end{aligned} \quad (6)$$

where s_i means retrieve values, o_i means reference values, \bar{o} means the average of o_i , $i = 1, \dots, n$, and n is the number of pair data for comparison.

In addition, bias, relative error (RE), and RMSE are used to quantify errors of RSLE. Bias quantifies the average absolute difference between retrieve values and reference values. RE is the absolute value of the bias divided by the magnitude of the reference values. RMSE is the standard deviation of the retrieve values around reference values. Basically, the RMSE represents a combination of standard deviation and bias.

Their definitions are described as follows [47]:

$$\begin{aligned} \text{Bias} &= \frac{\sum_{i=1}^n (s_i - o_i)}{n}, \\ \text{RE} &= \frac{|\text{Bias}|}{(1/n) \sum_{i=1}^n o_i} \times 100\%, \\ \text{RMSE} &= \sqrt{\frac{\sum_{i=1}^n (s_i - o_i)^2}{n}}. \end{aligned} \quad (7)$$

3. Study Materials and Data Processing

3.1. Study Area and Ground Sites. As a typical inland river basin in the northwest of China, the Heihe River Basin is located between $97^\circ 24' \sim 102^\circ 10' \text{E}$ and $37^\circ 41' \sim 42^\circ 42' \text{N}$ and covers an area of approximately $130\,000 \text{ km}^2$. The selected 6 ground observation sites are parts of multiscale EC observation matrices belonging to Heihe Watershed Allied Telemetry Experimental Research (HiWATER) [48, 49], and they are acquired over the Zhangye region ($100^\circ 25' \text{E}$, $38^\circ 51' \text{N}$, 1519 m) in the middle reaches of Heihe River Basin (Figure 1). A total of 6 EC sites measuring LE and H_s are used for data analysis and accuracy assessment (Table 1), accompanied by 6 automatic weather stations (AWS) which are used to measure the near-surface meteorological parameters. In view of spatial homogeneity and underlying representativeness, observations focus on six different areas with landscapes ranging from moist vegetated surfaces (vegetable, orchard, and wetland) to arid nonvegetated surfaces (village, desert, and Gobi). The locations of sites imply the similar climatic conditions. The underlying surfaces are homogeneous at all sites excepted for orchard and village sites. Based on the field visit, the fruit trees grow with bean seeding at orchard site. At village site, the underlying surface is composed of the bare soil, house, road, and trees.

All instruments were intercompared over the Gobi between 14 and 24 May, 2012 [43]. The intercompared and well agreed instruments, accompanied by the uniform data processing steps and standards, ensured data consistency, which guaranteed the reliability of validation [50]. All selected sites were covered by different land cover types. Thus, for convenience, the site names were replaced by the types of underlying surfaces here.

3.2. Data Description

3.2.1. Meteorological and Surface Flux Data. Acquired from the HiWATER, the EC and AWS data span from June 25 to September 15 in 2012, the overlapping time span of EC data at all sites (Table 2). All AWS and EC data were produced, archived, and made available to the scientific community by the Cold and Arid Regions Science Data Center at Lanzhou [43, 51]. They were used for validation and error source analysis of RSLE. All LE validation references were obtained by H_s (directly measured by EC), R_n , and G_s (measured by AWS) (see (5)).

The parameters obtained by AWS were averaged every 10 minutes, whereas the temporal resolution of EC was 30

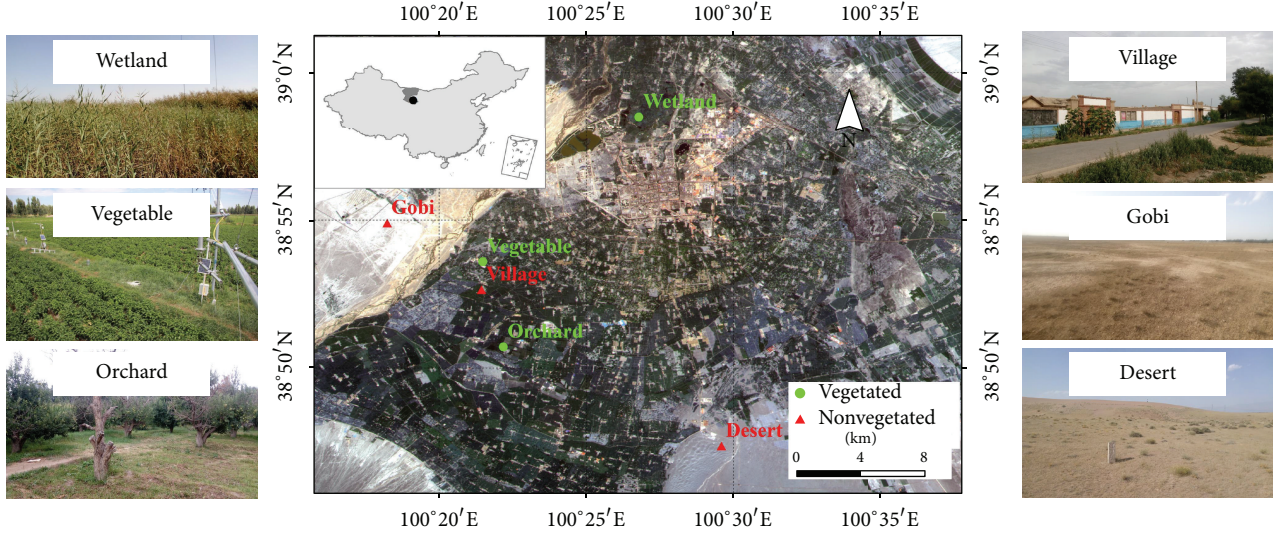


FIGURE 1: Geolocation of EC observation sites and illustration of land surface.

TABLE 1: Descriptive information of EC sites.

Type	Sites	Longitude (°)	Latitude (°)	Altitude (m)	EC height (m)
Vegetated	Wetland	100.446	38.975	1460	5.2
	Vegetable	100.358	38.893	1552	3.8
	Orchard	100.370	38.845	1559	7.0
Nonvegetated	Village	100.358	38.878	1561	4.2
	Gobi	100.304	38.915	1562	4.6
	Desert	100.493	38.789	1594	4.6

TABLE 2: Datasets for analysis.

Datasets	Parameters	Temporal-spatial resolution	Data types	Data purpose
EC	LE/H_s	30 minutes, hundreds of meters	Meteorology	Validation
AWS	$P/R_{ld}/R_{lu}/T_a/R_n/G_s$	10 minutes, several meters to hundreds of meters	Meteorology	Validation
ASTER	ϵ	10–20 days, 90 m	Remote sensing	Validation
MYD07	$P/T_d/T_a/\theta$	Daily, 5 km	Remote sensing	Retrieval
MCD43	α	8 days, 1 km	Remote sensing	Retrieval
MYD11	T_s/ϵ	Daily, 1 km	Remote sensing	Retrieval
MYD13	NDVI	16 days, 1 km	Remote sensing	Retrieval

minutes. So we need to average the parameters derived from AWS to the mean in 30 minutes. In addition, consider that the time of satellite overpassing, AWS, and EC data at the nearest moment were regarded as the actual values of input parameters. Except for LST, other actual values were measured directly by AWS. The actual LST was estimated from the upwelling and downwelling longwave radiation measured by AWS using the following equation:

$$T_s = \left[\frac{R_{lu} - (1 - \epsilon) \cdot R_{ld}}{\epsilon \cdot \sigma} \right], \quad (8)$$

where R_{lu} (R_{ld}) is the surface upwelling (downwell) longwave radiation.

3.2.2. Remote Sensing Data. Remote sensing data were obtained from the MODIS and Advanced Spaceborne Thermal Emission and Reflection Radiometer (ASTER) products. The pixels located at the sites were obtained to retrieve LE. All chosen images were acquired under clear sky during 13:00 to 15:00 (local time) from June 25 to September 15, 2012. The temporal and spatial resolutions of these products were listed in Table 2.

MODIS are onboard NASA's Earth Observation System TERRA and AQUA satellites [52]. As mentioned above, various products (MOD, MYD, and MCD) are provided by MODIS. They have been produced, archived, and made available to the scientific community by the Level 1 and

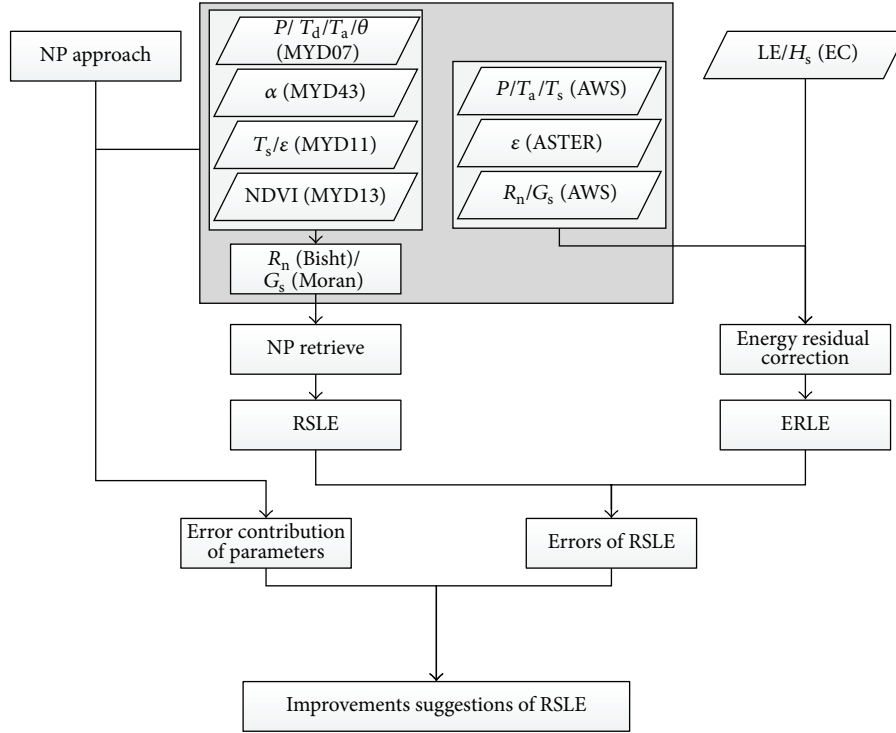


FIGURE 2: Schematic representation of the procedure for analysis in our study.

Atmosphere Archive and Distribution System (LAADS), the National Aeronautics and Space Administration (NASA). In our study, both MYD and MCD (MYD07, MYD11, MYD13, and MCD43) were selected to retrieve LE. MYD07 provided the profile of air temperature and moisture to obtain the near-surface atmospheric temperature and dew temperature [53]. MYD11 provided the land surface temperature and emissivity [54]. MYD13 provided the 16-day NDVI [55, 56]. MCD43 provided 8-day nadir BRDF-adjusted albedos [57, 58], including the albedo in band 1 to band 7.

ASTER radiometer has 5 thermal infrared (TIR) bands to provide TIR spectral emissivity variations at 90 m spatial resolution [59]. LSE product is produced by the Temperature and Emissivity Separation (TES) algorithm [60]. In our study, ASTER product was also provided by the Cold and Arid Regions Science Data Center at Lanzhou [61, 62]. ASTER product was used to estimate LSE. LSE can be represented by the ASTER narrowband emissivities using the following linear equation [63]:

$$\varepsilon = 0.197 + 0.025\varepsilon_{10} + 0.057\varepsilon_{11} + 0.237\varepsilon_{12} + 0.333\varepsilon_{13} + 0.146\varepsilon_{14}, \quad (9)$$

where $\varepsilon_{10} \sim \varepsilon_{14}$ are the five ASTER narrowband emissivities. It was regarded as the real value of LSE because of the high accuracy and spatial resolution.

3.3. Data Processing. Aiming to ascertain the applicability of LE retrieve algorithm, the validation and error source analysis of RSLE were made at the different sites (Figure 2). Firstly,

the LE obtained by EC was corrected by R_n , G_s (obtained by AWS), and H_s (obtained by EC) in the way of energy residual correction (see (5)). Secondly, R_n and G_s were retrieved by MODIS product in Bisht's and Moran's algorithm ((2) and (4)), respectively. Then, RSLE can be estimated in NP approach (see (1)). The errors of RSLE were derived from the discrepancies between RSLE and ERLE. Thirdly, to qualify the error contribution due to the input error of one parameter, that parameter (derived from MODIS) and the other actual parameters (measured by AWS/ASTER) were brought in NP approach to get LE estimation (see (1)). Similarly, all actual input parameters (measured by AWS/ASTER) were brought in NP approach to get LE estimation, too. The difference among these two estimations was regarded as the error contribution of the parameter at the retrieval moment [64]. Fourthly, according to the error analysis, we searched for the probable ways to improve the retrieve accuracy.

4. Results

4.1. Data Features at the Sites. Table 3 showed energy fluxes and environmental parameters measured by surface observations at the six sites. In the order of decreasing surface moistures, these sites were listed as wetland, vegetable, orchard, village, Gobi, and desert sites. The decreasing order matched pretty well with the vegetation abundances at these sites. Generally, there were higher LE in vegetated region with higher R_n /LSE and lower G_s /LST. In detail, R_n was higher at vegetated than nonvegetated sites. Mean amount of R_n was 625~735 W/m² for vegetated sites, and it decreased to

TABLE 3: Average of fluxes and environment parameters derived from AWS/ASTER at the six sites in the EC matrices, including net radiation (R_n), soil heat flux (G_s), land surface temperature (T_s), near-surface air temperature (T_a), land surface emissivity (LSE), near-surface pressure (P), latent heat (LE), and sensible heat (H_s). The energy residual corrected (ER) LE is also revealed.

Parameters	Types	Wetland	Vegetable	Orchard	Village	Gobi	Desert
R_n (W/m^2)	AWS	625.12	646.55	735.09	543.48	489.84	519.40
G_s (W/m^2)	AWS	96.39	64.34	62.35	86.95	90.06	90.40
T_s (K)	AWS	305.35	304.08	301.20	315.46	316.68	320.71
T_a (K)	AWS	299.78	299.18	298.72	300.02	298.29	299.58
LSE	ASTER	0.981	0.978	0.980	0.975	0.958	0.932
P (kpa)	AWS	89.11	88.32	83.89	83.28	84.02	84.10
LE (W/m^2)	ER	496.51	482.68	575.93	297.33	184.96	212.54

TABLE 4: Average of input parameters derived by MODIS products at the six sites, including land surface temperature (T_s), near-surface air temperature (T_a), land surface emissivity (LSE), near-surface pressure (P), dew point temperature (T_d), albedo, and NDVI. The retrieved net radiation (R_n), soil heat flux (G_s), and latent heat flux (LE) are also shown.

Parameters	Wetland	Vegetable	Orchard	Village	Gobi	Desert
T_s (K)	301.64	301.39	301.46	300.73	307.61	309.33
LSE	0.965	0.972	0.973	0.973	0.964	0.963
P (kpa)	79.80	78.73	77.96	78.47	79.15	77.06
T_d (K)	277.33	279.07	279.35	279.55	278.28	278.08
T_a (K)	298.15	298.58	291.75	296.16	299.10	289.44
Albedo	0.193	0.171	0.171	0.165	0.207	0.186
NDVI	0.713	0.701	0.717	0.790	0.143	0.117
R_n (W/m^2)	654.26	685.18	650.64	685.19	616.08	572.75
G_s (W/m^2)	84.46	89.46	83.35	73.91	264.77	257.16
LE (W/m^2)	425.07	452.25	354.37	441.10	233.28	120.48

490~540 W/m^2 for nonvegetated sites. The difference was probably due to high surface albedo at nonvegetated sites. G_s increased from vegetated (down to 62.34 W/m^2 for vegetable) to nonvegetated sites (up to 90.40 W/m^2 for desert). After energy residual correction, ERLE was higher at vegetated sites (483~576 W/m^2) than at nonvegetated sites (185~297 W/m^2). Mean LSE was in the range of 0.978~0.981 and 0.932~0.975 for vegetated and nonvegetated sites. On the contrary, LST was considerably lower at vegetated sites with typical values of 300~305 K, compared to 315~320 K at nonvegetated sites. The near-surface pressure was higher at vegetated sites than at nonvegetated sites (up to 89.11 kpa for wetland, and down to 83.28 kpa for desert). The difference of AT was little, and there was about 299 K of AT at all sites. These environmental parameters were the background of LE retrieve.

4.2. MODIS Retrievals of R_n , G_s , and LE. R_n , G_s , and LE were all derived from satellite retrieve. Table 4 showed input parameters obtained by satellite retrieve at the six sites. The dew point temperature, pressure, and LSE were similar among all sites, with values of about 278 K, 78 kpa, and 0.96, respectively. Other parameters were different among sites. In detail, AT were 296~299 K at all sites except for orchard (292 K) and desert (289 K) sites. Low LST appeared at vegetated sites (about 301 K), whereas high LST occurred at nonvegetated sites (300~309 K). Similarly, albedo was slightly lower at vegetated sites with value of about 0.17, compared to

about 0.19 at nonvegetated sites. Thus, generally, the retrieved R_n was higher in vegetated region (650~685 W/m^2) than in the nonvegetated region (570~685 W/m^2). Considering the lower NDVI at nonvegetated sites (less than 0.2), the higher retrieved G_s (more than 250 W/m^2) appeared there. On the basis of the retrieved R_n and G_s , RSLE was higher at vegetated sites (350~450 W/m^2) than at the nonvegetated sites (120~440 W/m^2).

The instantaneous retrieve results of R_n , G_s , and LE in a part of Zhangye region at 05:55 (UTC) in August 20, 2012, were shown in Figure 3. The distribution of LE, R_n , and G_s was in good accordance with the oasis-desert ecosystem. The desert (the east and south of the region) had lower R_n because of the high albedo here. The desert also had higher G_s because of bare surface. In addition, the oasis (the middle of the region) and wetland (the north of the region) had more evaporation than desert because of the irrigation. In view of retrieve values, the LE was up to 300~400 W/m^2 in the region of oasis, whereas the LE decreased to 150~250 W/m^2 in the region of desert. In general, the distribution of retrieve results was deemed to be reliable.

4.3. Accuracy Assessment of MODIS-Retrieved LE. Figure 4 revealed the relationship between ERLE (donated by x -axis) and RSLE (donated by y -axis) at the retrieval moment. In general, relative to ERLE in 30 minutes, the RSLE was generally accurate and underestimated with bias, RMSE, RE,

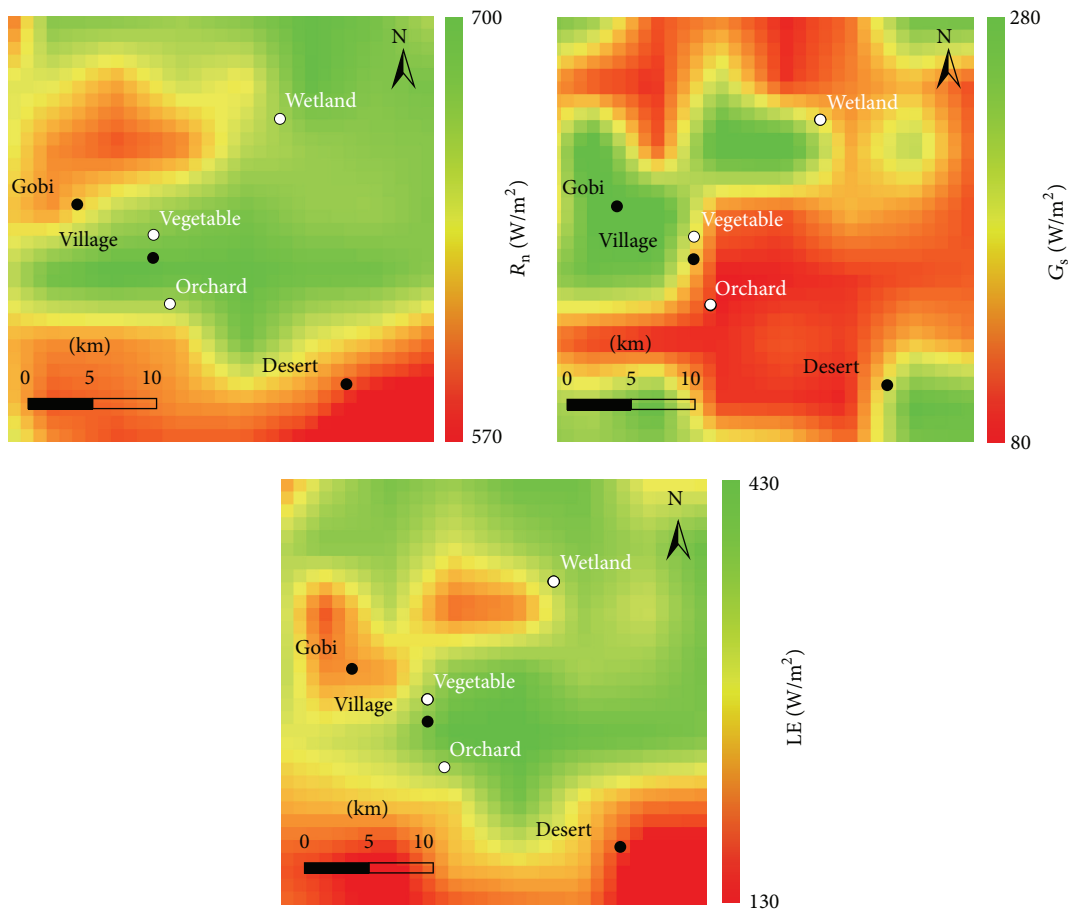


FIGURE 3: Distributions of the retrieved net radiation (R_n), soil heat flux (G_s), and latent heat flux (LE) in a part of Zhangye region at 05:55 (UTC) in August 20, 2012.

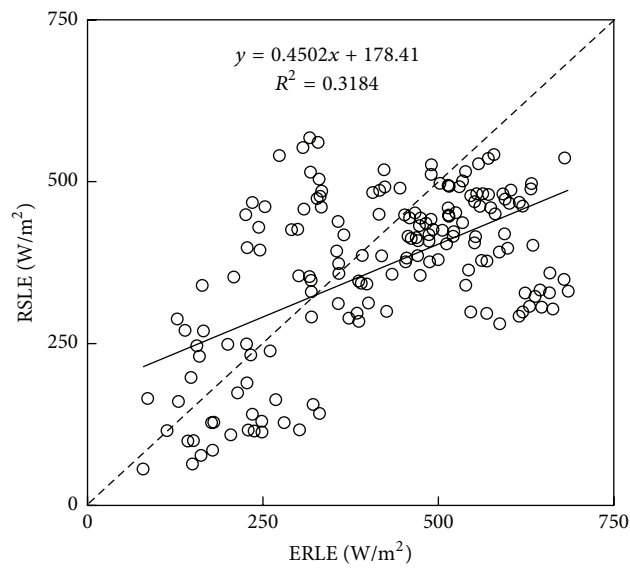


FIGURE 4: Overall comparison between ERLE and RSLE.

TABLE 5: Errors of RSLE at 6 sites; statistics include the bias, RMSE, and RE.

Sites	Bias (W/m ²)	RMSE (W/m ²)	RE (%)
Wetland	-71.44	79.77	14.39
Vegetable	-43.77	73.62	8.82
Orchard	-221.56	239.55	38.47
Village	143.77	160.14	48.35
Gobi	48.33	67.97	26.13
Desert	-92.32	105.64	43.44
Overall	-49.64	144.20	11.97

slope, and R^2 of -49.64 W/m^2 , 144.20 W/m^2 , 11.97% , 0.45 , and 0.32 , respectively (Table 5).

At the site scale, Figure 5 also showed the comparison between RSLE and ERLE at all 6 sites. RSLE was generally underestimated, and it was in relatively good agreement with ERLE at most of the sites, with R^2 of $0.11\sim 0.76$, bias of $-222\sim 49 \text{ W/m}^2$, RE of $9\sim 49\%$, and RMSE of $68\sim 240 \text{ W/m}^2$. The highest accuracy occurred at vegetable, wetland, and Gobi sites, with RE (RMSE) value of 8.82% (73.62 W/m^2), 14.39% (79.77 W/m^2), and 26.13% (67.97 W/m^2), respectively. The RSLE was less satisfactory at orchard and village sites, with RE of about $40\sim 50\%$ and RMSE of more than 160 W/m^2 .

To validate the retrieved LE further, the LE directly observed by EC (ECLE) was also compared with RSLE in Figure 6. Similarly, the RSLE was in relatively good agreement with ECLE with R^2 of $0.11\sim 0.36$ at vegetated sites. Nevertheless, at the nonvegetated sites, the accordance disappeared with R^2 of $0.05\sim 0.23$. Relative to the ECLE in Figure 6, the ERLE matched better with retrieved surface LE in Figure 5, especially at nonvegetated sites. Thus, at least, the RSLE had a satisfactory accuracy at vegetated sites, and it also probably had a relatively good accuracy at nonvegetated sites.

4.4. Error Sources and Their Contributions to MODIS-Retrieved LE. To reveal the error contributions of input error, the input error of each parameter was showed firstly (Figure 7). R_n was retrieved with low accuracy at village, orchard, and Gobi sites with bias value of more than 80 W/m^2 . There was a low accuracy of retrieved G_s at almost all sites, especially at Gobi and desert sites (bias values of about 170 W/m^2). The large difference (about 10 kpa) of surface pressure appeared at Gobi and desert sites. At most sites, the biases of AT were $2\sim 5 \text{ K}$, except for orchard (-7 K) and desert (-10 K) sites. Similarly, the biases of LST were also $0\sim 4 \text{ K}$ at vegetated sites, whereas they were more than 9 K at nonvegetated sites. The LSE difference between MODIS and ASTER products was less than 0.01 at all sites except for Gobi (-0.036) and desert sites (0.031).

On the basis of input errors, the error contribution can be revealed. Figure 8 showed the error contributions of each factor (shown as the line) and the error of RSLE (shown as the columns) at 6 sites. Except for orchard and village sites, the RSLE were in relatively satisfactory accuracy, and the biases were within $-90\sim 50 \text{ W/m}^2$ at the other 4 sites. Based on the analysis of error sources, it was clear that the major error sources (inducing more than 40 W/m^2 RSLE error)

were R_n , G_s , LST, and AT at nonvegetated sites, with error contributions of $40\sim 110 \text{ W/m}^2$, $-120\sim 10 \text{ W/m}^2$, $>60 \text{ W/m}^2$, and $-100\sim 10 \text{ W/m}^2$, respectively. At vegetated sites, input errors were not the dominant error sources of RSLE.

In detail, the large G_s error contribution (causing more than 100 W/m^2 RSLE error) appeared at Gobi and desert sites. About 100 W/m^2 RSLE error caused by the R_n error occurred at village and Gobi sites. The influence of AT and LST error on LE error was below 40 W/m^2 at most of sites, except for the LST at village and Gobi sites, the AT and LST at desert site, and AT at orchard site. The error contribution of LSE accounted for RSLE error as a small part (leading to less than 10 W/m^2 LE error). Similarly, the input errors of pressure affected RSLE error quite little (mostly less than 1 W/m^2). In addition, according to validation, the accuracy of RSLE was unsatisfactory at orchard and village with a bias of -221.56 W/m^2 and 143.77 W/m^2 , respectively. At these two sites, the main errors sources (inducing more than 100 W/m^2 RSLE error) were AT and R_n .

5. Discussion

The improvement of input data can possibly benefit LE retrieve in the future. R_n and G_s are not the direct input parameters of algorithms but the indirect parameters retrieved by Bisht's and Moran's algorithm [36, 38]. The improvement of R_n and G_s retrieval algorithms is helpful to the improvement of RSLE. In our study, the Bisht's algorithm under clear sky [36] is selected as R_n retrieval algorithm. Considering the widespread cloud, Bisht's algorithm under all sky [65] can be chosen to broaden applications. Besides, the accuracy of retrieved R_n is especially unsatisfactory in arid nonvegetated region [36]. It is suitable to replace the retrieved R_n by the observation directly measured by the Clouds and the Earth's Radiant Energy System (CERES) project [66]. CERES's accuracy meets the demand of R_n input in the region of desert [67, 68]. For G_s , because of the subtle temporal variation of NDVI in the arid region, G_s retrieved by Moran's algorithm varies slightly. Thus, some more sensitive algorithm can be chosen for G_s , such as the G_s retrieval algorithm in SEBS model or in the way of thermal inertia [19, 27].

AT and the dew point temperature are derived from the atmospheric profile data of MYD07 in our study. They are not the values at the near-surface but the values of the atmospheric profile nearest to the surface. It is evident that the more accurate atmospheric information contributes to the retrieve of R_n and LE. So the other Earth observations with the high accuracy (e.g., the Goddard Earth Observing System Model, Version 5 (GEOS-5)) are optional substitutions [69]. For LST and LSE, they are derived from the MYD11 in the split-windows algorithm [54]. Wan et al. [70] have reported that just the average of bands 31 and 32 emissivities could lead to an overestimation of LSE, especially in arid and semiarid region. Accordingly, LST is underestimated in these regions. The MYD21 C6 is estimated to be published in 2016, and it can supply the more accurate LST and LSE based on TES algorithm [71], especially in the arid and semiarid region. That means the remarkable improvement of R_n and LE retrieve if we replace MYD11 by MYD21.

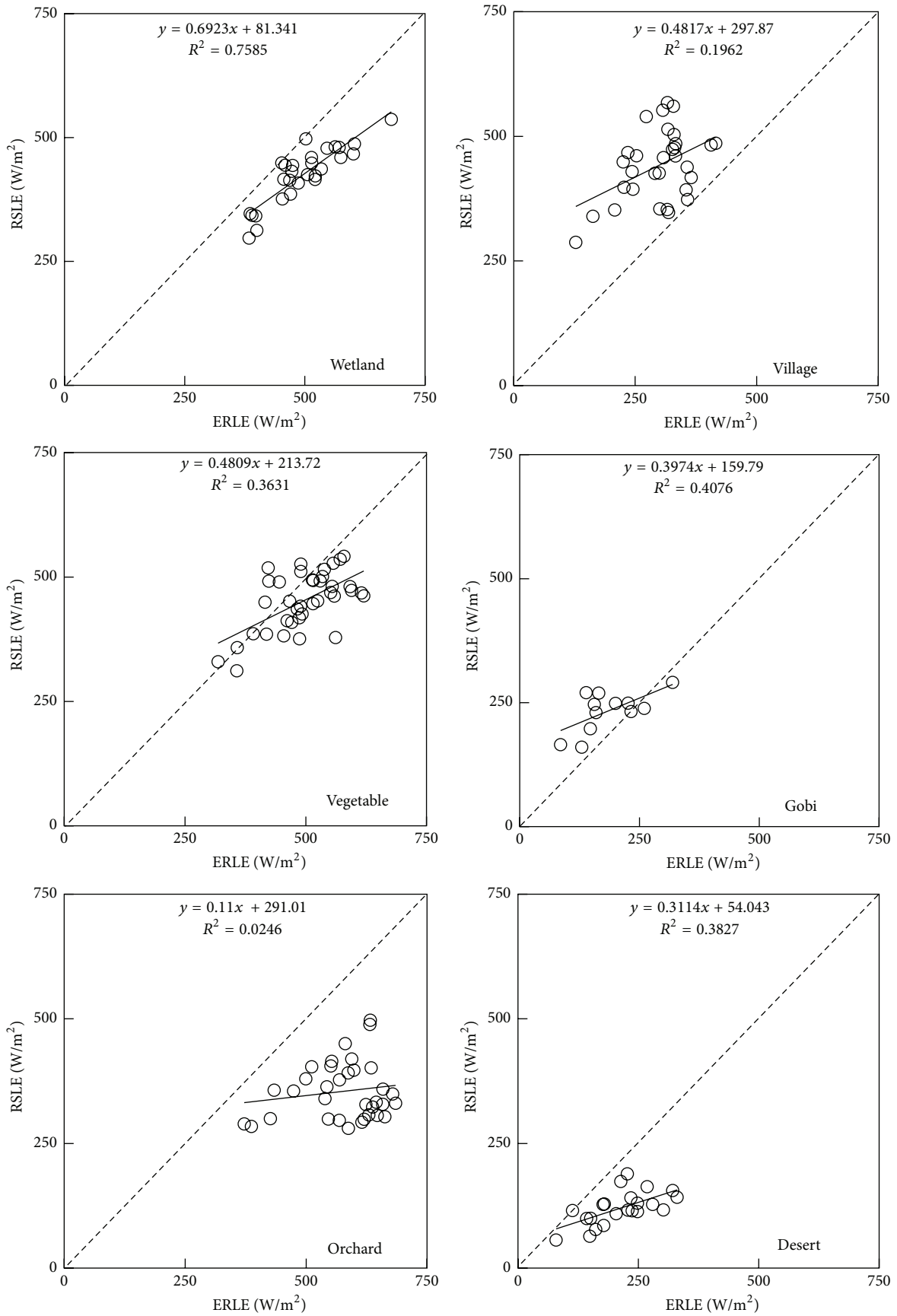


FIGURE 5: Comparisons between ERLE and RSLE at 6 sites.

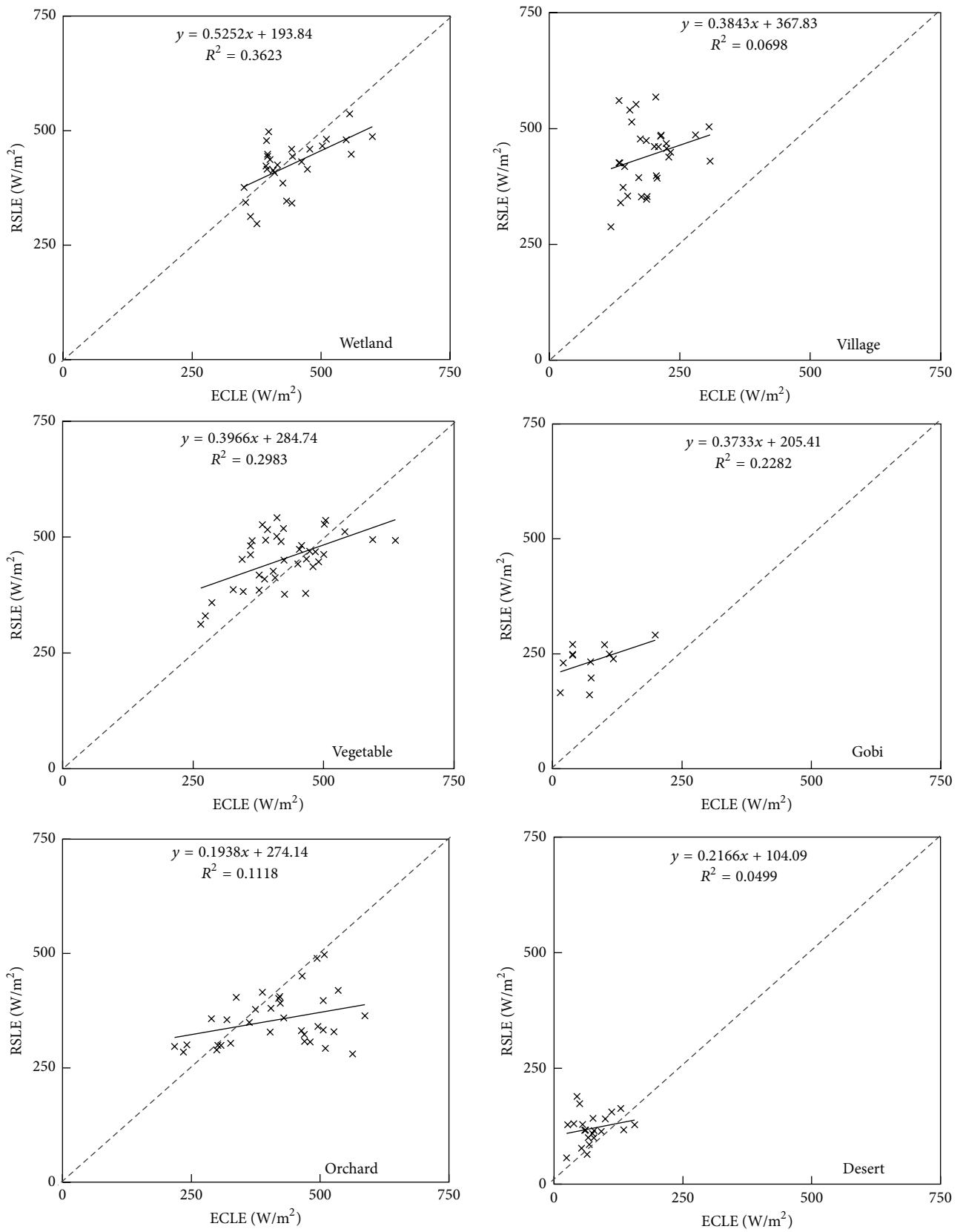


FIGURE 6: Comparisons between ECLE and RSLE at 6 sites.

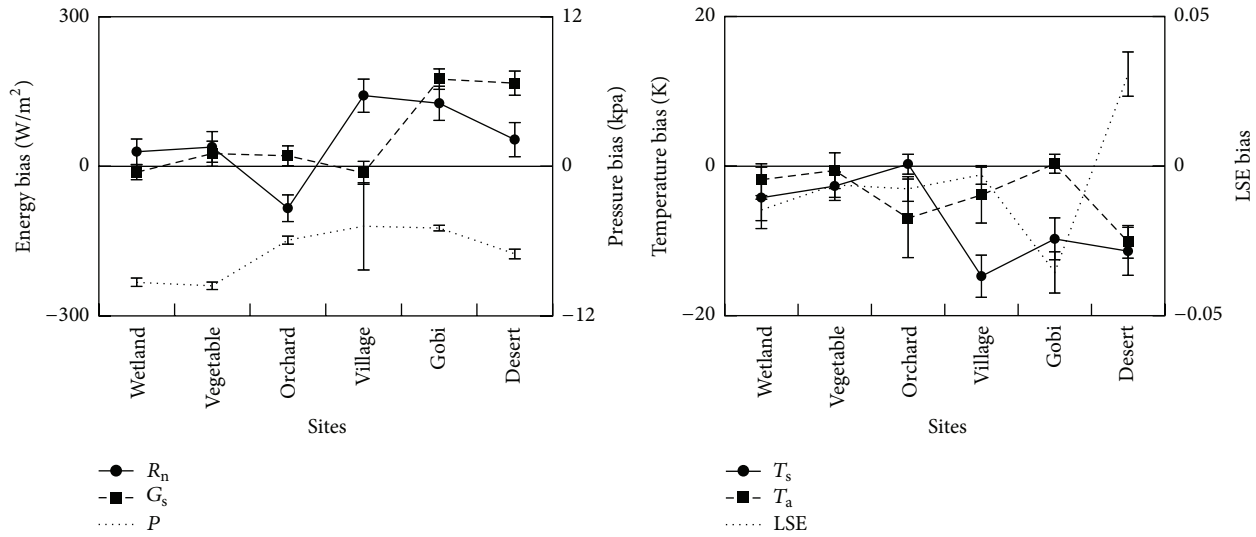


FIGURE 7: Average (line) and standard deviation (bar) of input parameter errors at 6 sites, including net radiation (R_n), soil heat flux (G_s), land surface temperature (T_s), near-surface air temperature (T_a), land surface emissivity (LSE), and near-surface pressure (P).

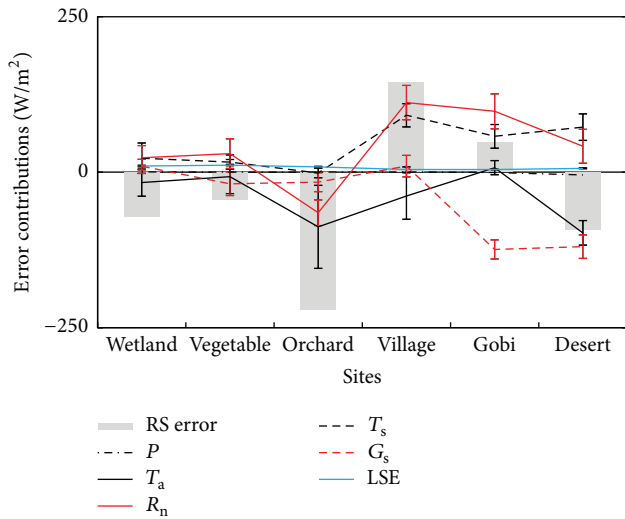


FIGURE 8: Error contributions of each factor, including the averages (line) and standard deviation (bar), along with errors of RSLE (column).

Other datasets with a higher spatial and temporal resolution can be also used to retrieve LE, such as NDVI and albedo products. In our study, the NDVI/albedo is assumed to be invariant in 16/8 days. There is a way to improve the temporal consistency by using other NDVI and albedo products with 1km and 5-day resolution [72–74]. Furthermore, the correction based on digital elevation models should be considered in the region with undulant surfaces [31, 75].

6. Conclusions

NP approach provides a novel but simple method to estimate LE. In our study, NP approach attempts to develop a LE

retrieval algorithm under clear sky which primarily uses remote sensing information and eliminates the need for ground information as model input, by using various land and atmospheric data products available from MODIS. The validation of retrieval result and the exploration of error sources were analyzed in succession.

At the temporal and spatial scales, the result of RSLE is within a reliable range. At the retrieve moment, RSLE is generally accurate. The instantaneous RSLE is underestimated with bias, R^2 , RE, and RMSE values of -49.64 W/m^2 , 0.32, 11.97%, and 144.20 W/m^2 , respectively. At the site scale, RSLE is in relatively good accuracy at all sites, with $R^2 = 0.11\sim 0.76$, bias = $-222\sim 49 \text{ W/m}^2$, RE = 9~49%, and RMSE = $68\sim 240 \text{ W/m}^2$. Nevertheless, the accuracy of RSLE is unsatisfactory at orchard and village sites. In view of error source, in arid nonvegetated region, the dominant error contributions (causing 40 W/m^2 error of RSLE) are R_n , G_s , LST, and AT. In vegetated region, the input errors are not the dominant error sources of RSLE. In order to improve the accuracy of RSLE, some improvement recommendations of input parameters can be considered in the future. The future research work would aim to improve the accuracy of LE estimation.

Competing Interests

The authors declare that they have no competing interests.

Acknowledgments

This work is supported by the National Natural Science Foundation of China (no. 91125004). The authors thank the Cold and Arid Regions Science Data Center at Lanzhou for providing observation data (<http://westdc.westgis.ac.cn>) and the LAADS for providing MOIDS products (<http://ladsweb.nascom.nasa.gov>). They also thank Professor Liu S. M. and

Dr. Xu Z. W. for their kind assistance in providing field data and help in field visit.

References

- [1] R. Burman and L. O. Pochop, *Evaporation, Evapotranspiration and Climatic Data*, Elsevier Science, Amsterdam, The Netherlands, 1994.
- [2] W. Brutsaert, *Evaporation into the Atmosphere: Theory, History, and Applications*, Springer, Dordrecht, The Netherlands, 1982.
- [3] T. Oki and S. Kanae, "Global hydrological cycles and world water resources," *Science*, vol. 313, no. 5790, pp. 1068–1072, 2006.
- [4] H. L. Penman, "Natural evaporation from open water, bare soil and grass," *Proceedings of the Royal Society A: Mathematical, Physical and Engineering Sciences*, vol. 193, no. 1032, pp. 120–145, 1948.
- [5] J. L. Monteith, "Evaporation and environment," *Symposia of the Society for Experimental Biology*, vol. 19, pp. 205–234, 1965.
- [6] C. H. Priestley and R. J. Taylor, "On the assessment of surface heat flux and evaporation using large-scale parameters," *Monthly Weather Review*, vol. 100, no. 2, pp. 81–92, 1972.
- [7] T. A. Howell, A. D. Schneider, D. A. Dusek, T. H. Marek, and J. L. Steiner, "Calibration and scale performance of Bushland weighing lysimeters," *Transactions of the American Society of Agricultural Engineering*, vol. 38, no. 4, pp. 1019–1024, 1995.
- [8] M. Ibáñez and F. Castellví, "Simplifying daily evapotranspiration estimates over short full-canopy crops," *Agronomy Journal*, vol. 92, no. 4, pp. 628–632, 2000.
- [9] D. A. Zeweldi, M. Gebremichael, J. Wang, T. Sammis, J. Kleissl, and D. Miller, "Intercomparison of sensible heat flux from large aperture scintillometer and eddy covariance methods: field experiment over a homogeneous semi-arid region," *Boundary-Layer Meteorology*, vol. 135, no. 1, pp. 151–159, 2010.
- [10] D. Baldocchi, E. Falge, L. Gu et al., "FLUXNET: a new tool to study the temporal and spatial variability of ecosystem-scale carbon dioxide, water vapor, and energy flux densities," *Bulletin of the American Meteorological Society*, vol. 82, pp. 2415–2434, 2001.
- [11] B. Mueller, S. I. Seneviratne, C. Jimenez et al., "Evaluation of global observations-based evapotranspiration datasets and IPCC AR4 simulations," *Geophysical Research Letters*, vol. 38, no. 6, Article ID L06402, 2011.
- [12] K. Wang and R. E. Dickinson, "A review of global terrestrial evapotranspiration: observation, modeling, climatology, and climatic variability," *Reviews of Geophysics*, vol. 50, no. 2, Article ID RG2005, 2012.
- [13] D. Courault, B. Seguin, and A. Olioso, "Review on estimation of evapotranspiration from remote sensing data: from empirical to numerical modeling approaches," *Irrigation and Drainage Systems*, vol. 19, no. 3-4, pp. 223–249, 2005.
- [14] Z.-L. Li, R. Tang, Z. Wan et al., "A review of current methodologies for regional evapotranspiration estimation from remotely sensed data," *Sensors*, vol. 9, no. 5, pp. 3801–3853, 2009.
- [15] L. Jiang and S. Islam, "A methodology for estimation of surface evapotranspiration over large areas using remote sensing observations," *Geophysical Research Letters*, vol. 26, no. 17, pp. 2773–2776, 1999.
- [16] L. Jiang and S. Islam, "Estimation of surface evaporation map over southern Great Plains using remote sensing data," *Water Resources Research*, vol. 37, no. 2, pp. 329–340, 2001.
- [17] T. Carlson, "An overview of the 'triangle method' for estimating surface evapotranspiration and soil moisture from satellite imagery," *Sensors*, vol. 7, no. 8, pp. 1612–1629, 2007.
- [18] G. J. Roerink, Z. Su, and M. Menenti, "S-SEBI: a simple remote sensing algorithm to estimate the surface energy balance," *Physics and Chemistry of the Earth, Part B: Hydrology, Oceans and Atmosphere*, vol. 25, no. 2, pp. 147–157, 2000.
- [19] Z. Su, "The Surface Energy Balance System (SEBS) for estimation of turbulent heat fluxes," *Hydrology and Earth System Sciences*, vol. 6, no. 1, pp. 85–99, 2002.
- [20] G. Y. Qiu, T. Yano, and K. Momii, "Estimation of plant transpiration by imitation leaf temperature. I. Theoretical consideration and field verification," *Transaction of the Japanese Society of Irrigation, Drainage and Reclamation Engineering*, vol. 64, pp. 401–410, 1996.
- [21] G. Y. Qiu, T. Yano, and K. Momii, "An improved methodology to measure evaporation from bare soil based on comparison of surface temperature with a dry soil," *Journal of Hydrology*, vol. 210, no. 1-4, pp. 93–105, 1998.
- [22] Y. J. Xiong and G. Y. Qiu, "Estimation of evapotranspiration using remotely sensed land surface temperature and the revised three-temperature model," *International Journal of Remote Sensing*, vol. 32, no. 20, pp. 5853–5874, 2011.
- [23] Q. Mu, F. A. Heinsch, M. Zhao, and S. W. Running, "Development of a global evapotranspiration algorithm based on MODIS and global meteorology data," *Remote Sensing of Environment*, vol. 111, no. 4, pp. 519–536, 2007.
- [24] Q. Mu, M. Zhao, and S. W. Running, "Improvements to a MODIS global terrestrial evapotranspiration algorithm," *Remote Sensing of Environment*, vol. 115, no. 8, pp. 1781–1800, 2011.
- [25] K. Zhang, J. S. Kimball, R. R. Nemani, and S. W. Running, "A continuous satellite-derived global record of land surface evapotranspiration from 1983 to 2006," *Water Resources Research*, vol. 46, no. 9, Article ID W09522, 2010.
- [26] R. Leuning, Y. Q. Zhang, A. Rajaud, H. Cleugh, and K. Tu, "A simple surface conductance model to estimate regional evaporation using MODIS leaf area index and the Penman-Monteith equation," *Water Resources Research*, vol. 44, no. 10, Article ID W10419, 2008.
- [27] L. Jia, Z. Su, B. van den Hurk et al., "Estimation of sensible heat flux using the Surface Energy Balance System (SEBS) and ATSR measurements," *Physics and Chemistry of the Earth*, vol. 28, no. 1-3, pp. 75–88, 2003.
- [28] W. W. Verstraeten, F. Veroustraete, and J. Feyen, "Estimating evapotranspiration of European forests from NOAA-imagery at satellite overpass time: towards an operational processing chain for integrated optical and thermal sensor data products," *Remote Sensing of Environment*, vol. 96, no. 2, pp. 256–276, 2005.
- [29] R. K. Singh, A. Irmak, S. Irmak, and D. L. Martin, "Application of SEBAL model for mapping evapotranspiration and estimating surface energy fluxes in South-Central Nebraska," *Journal of Irrigation and Drainage Engineering*, vol. 134, no. 3, pp. 273–285, 2008.
- [30] F. Tian, G. Qiu, Y. Yang, Y. Lü, and Y. Xiong, "Estimation of evapotranspiration and its partition based on an extended three-temperature model and MODIS products," *Journal of Hydrology*, vol. 498, pp. 210–220, 2013.
- [31] X. Zhao and Y. Liu, "Relative contribution of the topographic influence on the triangle approach for evapotranspiration estimation over mountainous areas," *Advances in Meteorology*, vol. 2014, Article ID 584040, 16 pages, 2014.

- [32] J. D. Kalma, T. R. McVicar, and M. F. McCabe, "Estimating land surface evaporation: a review of methods using remotely sensed surface temperature data," *Surveys in Geophysics*, vol. 29, no. 4-5, pp. 421-469, 2008.
- [33] Z. Jia, S. Liu, D. Mao, Z. Wang, Z. Xu, and R. Zhang, "A study of the validation method of remotely sensed evapotranspiration based on observation data," *Advances in Earth Science*, vol. 11, pp. 1248-1260, 2010.
- [34] R. R. Gillies, W. P. Kustas, and K. S. Humes, "A verification of the 'triangle' method for obtaining surface soil water content energy fluxes from remote measurements of the normalized difference vegetation index (NDVI) and surface radiant temperature," *International Journal of Remote Sensing*, vol. 18, no. 15, pp. 3145-3166, 1997.
- [35] Y. Liu, T. Hiyama, T. Yasunari, and H. Tanaka, "A nonparametric approach to estimating terrestrial evaporation: validation in eddy covariance sites," *Agricultural and Forest Meteorology*, vol. 157, pp. 49-59, 2012.
- [36] G. Bisht, V. Venturini, S. Islam, and L. Jiang, "Estimation of the net radiation using MODIS (Moderate Resolution Imaging Spectroradiometer) data for clear sky days," *Remote Sensing of Environment*, vol. 97, no. 1, pp. 52-67, 2005.
- [37] S. Liang, A. H. Strahler, and C. Walthall, "Retrieval of land surface albedo from satellite observations: a simulation study," *Journal of Applied Meteorology*, vol. 38, no. 6, pp. 712-725, 1999.
- [38] M. S. Moran, R. D. Jackson, L. H. Raymond, L. W. Gay, and P. N. Slater, "Mapping surface energy balance components by combining Landsat Thematic Mapper and ground-based meteorological data," *Remote Sensing of Environment*, vol. 30, no. 1, pp. 77-87, 1989.
- [39] K. Wilson, A. Goldstein, E. Falge et al., "Energy balance closure at FLUXNET sites," *Agricultural and Forest Meteorology*, vol. 113, no. 1-4, pp. 223-243, 2002.
- [40] T. Foken, "The energy balance closure problem: an overview," *Ecological Applications*, vol. 18, no. 6, pp. 1351-1367, 2008.
- [41] M. Mauder, C. Liebethal, M. Göckede, J.-P. Leps, F. Beyrich, and T. Foken, "Processing and quality control of flux data during LITFASS-2003," *Boundary-Layer Meteorology*, vol. 121, no. 1, pp. 67-88, 2006.
- [42] M. Mauder, S. P. Oncley, R. Vogt et al., "The energy balance experiment EBEX-2000. Part II: intercomparison of eddy-covariance sensors and post-field data processing methods," *Boundary-Layer Meteorology*, vol. 123, no. 1, pp. 29-54, 2007.
- [43] Z. Xu, S. Liu, X. Li et al., "Intercomparison of surface energy flux measurement systems used during the HiWATER-MUSOEXE," *Journal of Geophysical Research Atmospheres*, vol. 118, no. 23, pp. 13140-13157, 2013.
- [44] P. Schotanus, F. T. M. Nieuwstadt, and H. A. R. De Bruin, "Temperature measurement with a sonic anemometer and its application to heat and moisture fluxes," *Boundary-Layer Meteorology*, vol. 26, no. 1, pp. 81-93, 1983.
- [45] R. G. Allen, L. S. Pereira, T. A. Howell, and M. E. Jensen, "Evapotranspiration information reporting: I. Factors governing measurement accuracy," *Agricultural Water Management*, vol. 98, no. 6, pp. 899-920, 2011.
- [46] G. L. Squires, *Practical Physics*, Cambridge University Press, Cambridge, UK, 2001.
- [47] J. R. Nagol, E. F. Vermote, and S. D. Prince, "Effects of atmospheric variation on AVHRR NDVI data," *Remote Sensing of Environment*, vol. 113, no. 2, pp. 392-397, 2009.
- [48] Z. Jia, S. Liu, Z. Xu, Y. Chen, and M. Zhu, "Validation of remotely sensed evapotranspiration over the Hai River Basin, China," *Journal of Geophysical Research: Atmospheres*, vol. 117, no. 13, 2012.
- [49] X. Li, G. Cheng, S. Liu et al., "Heihe watershed allied telemetry experimental research (HiWATER): scientific objectives and experimental design," *Bulletin of the American Meteorological Society*, vol. 94, pp. 1145-1160, 2013.
- [50] J. Wang, J. Zhuang, W. Wang, S. Liu, and Z. Xu, "Assessment of uncertainties in eddy covariance flux measurement based on intensive flux matrix of HiWATER-MUSOEXE," *IEEE Geoscience and Remote Sensing Letters*, vol. 12, no. 2, pp. 259-263, 2015.
- [51] S. M. Liu, Z. W. Xu, W. Z. Wang et al., "A comparison of eddy-covariance and large aperture scintillometer measurements with respect to the energy balance closure problem," *Hydrology and Earth System Sciences*, vol. 15, no. 4, pp. 1291-1306, 2011.
- [52] A. Savtchenko, D. Ouzounov, S. Ahmad et al., "Terra and Aqua MODIS products available from NASA GES DAAC," *Advances in Space Research*, vol. 34, no. 4, pp. 710-714, 2004.
- [53] W. P. Menzel, S. W. Seemann, J. Li, and L. E. Gumley, "MODIS atmospheric profile retrieval algorithm theoretical basis document," Version 6, Reference Number: ATBD-MOD-07, http://modis.gsfc.nasa.gov/data/atbd/atbd_mod07.pdf.
- [54] Z. Wan and J. Dozier, "A generalized split-window algorithm for retrieving land-surface temperature from space," *IEEE Transactions on Geoscience and Remote Sensing*, vol. 34, no. 4, pp. 892-905, 1996.
- [55] A. Huete, K. Didan, T. Miura, E. P. Rodriguez, X. Gao, and L. G. Ferreira, "Overview of the radiometric and biophysical performance of the MODIS vegetation indices," *Remote Sensing of Environment*, vol. 83, no. 1-2, pp. 195-213, 2002.
- [56] A. R. Huete, K. Didan, Y. E. Shimabukuro et al., "Amazon rainforests green-up with sunlight in dry season," *Geophysical Research Letters*, vol. 33, no. 6, Article ID L06405, 2006.
- [57] C. B. Schaaf, F. Gao, A. H. Strahler et al., "First operational BRDF, albedo nadir reflectance product from MODIS," *Remote Sensing of Environment*, vol. 83, pp. 135-148, 2003.
- [58] J. G. Salomon, C. B. Schaaf, A. H. Strahler, F. Gao, and Y. Jin, "Validation of the MODIS Bidirectional Reflectance Distribution Function and albedo retrievals using combined observations from the Aqua and Terra platforms," *IEEE Transactions on Geoscience and Remote Sensing*, vol. 44, no. 6, pp. 1555-1564, 2006.
- [59] Y. Yamaguchi, A. B. Kahle, H. Tsu, T. Kawakami, and M. Pniel, "Overview of advanced space-borne thermal emission and reflection radiometer (ASTER)," *IEEE Transactions on Geoscience and Remote Sensing*, vol. 36, no. 4, pp. 1062-1071, 1998.
- [60] A. Gillespie, S. Rokugawa, T. Matsunaga, J. S. Cothren, S. Hook, and A. B. Kahle, "A temperature and emissivity separation algorithm for Advanced Spaceborne Thermal Emission and Reflection Radiometer (ASTER) images," *IEEE Transactions on Geoscience and Remote Sensing*, vol. 36, no. 4, pp. 1113-1126, 1998.
- [61] H. Li, D. Sun, Y. Yu et al., "Evaluation of the VIIRS and MODIS LST products in an arid area of Northwest China," *Remote Sensing of Environment*, vol. 142, pp. 111-121, 2014.
- [62] H. Li, H. S. Wang, Y. M. Du, Q. Xiao, and Q. H. Liu, "HiWATER: ASTER LST and LSE dataset in 2012 in the middle reaches of the Heihe River Basin," *Cold and Arid Regions Science Data Center at Lanzhou*, 2015.
- [63] J. Cheng, S. Liang, Y. Yao, and X. Zhang, "Estimating the optimal broadband emissivity spectral range for calculating surface

- longwave net radiation,” *IEEE Geoscience and Remote Sensing Letters*, vol. 10, no. 2, pp. 401–405, 2013.
- [64] J. C. Jiménez-Muñoz and J. A. Sobrino, “A generalized single-channel method for retrieving land surface temperature from remote sensing data,” *Journal of Geophysical Research: Atmospheres*, vol. 108, p. D22, 2003.
- [65] G. Bisht and R. L. Bras, “Estimation of net radiation from the MODIS data under all sky conditions: Southern Great Plains case study,” *Remote Sensing of Environment*, vol. 114, no. 7, pp. 1522–1534, 2010.
- [66] B. A. Wielicki, B. R. Barkstrom, E. F. Harrison, R. B. Lee III, G. Louis Smith, and J. E. Cooper, “Clouds and the Earth’s Radiant Energy System (CERES): an earth observing system experiment,” *Bulletin of the American Meteorological Society*, vol. 77, no. 5, pp. 853–868, 1996.
- [67] Atmospheric Science Data Center, *CERES Aqua Edition3A SSF Surface Fluxes—Accuracy and Validation*, 2010, https://eosweb.larc.nasa.gov/sites/default/files/project/ceres/quality_summaries/ssf_surface_flux_aqua_ed3A.pdf.
- [68] X. Pan, Y. Liu, and X. Fan, “Comparative assessment of satellite-retrieved surface net radiation: an examination on CERES and SRB datasets in China,” *Remote Sensing*, vol. 7, no. 4, pp. 4899–4918, 2015.
- [69] M. J. Suarez, M. M. Rienecker, R. Todling et al., *The GEOS-5 Data Assimilation System—Documentation of Versions 5.0. 1, 5.1. 0, and 5.2. 0*, vol. 27 of *Technical Report Series on Global Modeling and Data Assimilation*, NASA, 2008.
- [70] Z. Wan, Y. Zhang, Q. Zhang, and Z.-L. Li, “Validation of the land-surface temperature products retrieved from terra moderate resolution imaging spectroradiometer data,” *Remote Sensing of Environment*, vol. 83, no. 1-2, pp. 163–180, 2002.
- [71] G. Hulley, S. Veraverbeke, and S. Hook, “Thermal-based techniques for land cover change detection using a new dynamic MODIS multispectral emissivity product (MOD21),” *Remote Sensing of Environment*, vol. 140, pp. 755–765, 2014.
- [72] Z. Jiao, H. Zhang, Y. Dong, Q. Liu, Q. Xiao, and X. Li, “An algorithm for retrieval of surface albedo from small view-angle airborne observations through the use of BRDF archetypes as prior knowledge,” *IEEE Journal of Selected Topics in Applied Earth Observations and Remote Sensing*, vol. 8, no. 7, pp. 3279–3293, 2015.
- [73] J. Li, Y. L. Zeng, Q. H. Liu, B. Zhong, S. L. Wu, and J. J. Peng, *1km NDVI Dataset in China and ASEAN (2013) (MuSyQ-NDVI-1km-2013)*, Global Change Research Data Publisher and Repository, 2015.
- [74] B. Zhong, S. L. Wu, Q. H. Liu, X. J. Shan, A. X. Yang, and J. J. Peng, “1 km and 5 daily surface albedo dataset in China and ASEAN, 2013, (MuSyQ-REF-1 km-, 2013),” *Global Change Research Data Publisher and Repository*, 2015.
- [75] X. Zhao, Y. Liu, D. Zhao, and J. Peng, “Estimating evapotranspiration using triangle method with topographic correction from MODIS data in Taihu Basin, China,” in *Proceedings of the 6th International Conference on Wireless Communications Networking and Mobile Computing (WiCOM '10)*, pp. 1–5, IEEE, Chengdu City, China, September 2010.

Research Article

Accelerating the SCE-UA Global Optimization Method Based on Multi-Core CPU and Many-Core GPU

Guangyuan Kan,¹ Ke Liang,² Jiren Li,¹ Liuqian Ding,¹ Xiaoyan He,¹ Youbing Hu,³ and Mark Amo-Boateng²

¹State Key Laboratory of Simulation and Regulation of Water Cycle in River Basin, Research Center on Flood & Drought Disaster Reduction of the Ministry of Water Resources, China Institute of Water Resources and Hydropower Research, Beijing 100038, China

²College of Hydrology and Water Resources, Hohai University, Nanjing 210098, China

³Hydrologic Bureau (Information Center) of the Huaihe River Commission, Bengbu 233001, China

Correspondence should be addressed to Guangyuan Kan; kanguangyuan@126.com

Received 5 January 2016; Revised 17 February 2016; Accepted 2 March 2016

Academic Editor: Adel Hanna

Copyright © 2016 Guangyuan Kan et al. This is an open access article distributed under the Creative Commons Attribution License, which permits unrestricted use, distribution, and reproduction in any medium, provided the original work is properly cited.

The famous global optimization SCE-UA method, which has been widely used in the field of environmental model parameter calibration, is an effective and robust method. However, the SCE-UA method has a high computational load which prohibits the application of SCE-UA to high dimensional and complex problems. In recent years, the hardware of computer, such as multi-core CPUs and many-core GPUs, improves significantly. These much more powerful new hardware and their software ecosystems provide an opportunity to accelerate the SCE-UA method. In this paper, we proposed two parallel SCE-UA methods and implemented them on Intel multi-core CPU and NVIDIA many-core GPU by OpenMP and CUDA Fortran, respectively. The Griewank benchmark function was adopted in this paper to test and compare the performances of the serial and parallel SCE-UA methods. According to the results of the comparison, some useful advises were given to direct how to properly use the parallel SCE-UA methods.

1. Introduction

There are a large number of intelligent optimization algorithms in the field of parameter optimization of the environmental models, such as the genetic algorithm (GA) [1] and the particle swarm optimization (PSO) [2, 3]. Among these algorithms, the shuffled complex evolution method developed at The University of Arizona (SCE-UA) is recognized as an effective and robust global optimization technique for calibrating environmental models [4–9]. However, for problems with high dimensionality, complex objective function response surface, and high objective function computational load, it is resource-demanding and time-consuming. This disadvantage evokes the need for efficient acceleration of the SCE-UA method. The SCE-UA method is inherently parallel and should be accelerated at algorithm level. Besides, the parallel algorithm needs to be properly implemented on powerful parallel computation hardware. With the development of the parallel computing technology, the best way

is the utilization of the heterogeneous computing system, which is composed by the multi-core central processing units (CPUs) and the many-core graphics processing units (GPUs). However, in previous literatures, the algorithm level parallelization analysis and the parallelization based on the heterogeneous computing system for the SCE-UA method are rare.

Parallel computing has been more and more popular in one form or another for many decades. In the early stages it was generally restricted to practitioners who had access to large and expensive machines. Today, things are quite different. Almost all consumer desktop and laptop computers have CPUs with multiple cores. Multi-core CPU hardware systems are build up on a set of processors which have access to a common memory. This architecture is recognized as shared-memory system. By placing several cores on a chip, multi-core processors offer a way to improve the performance of microprocessors. In the programming model of the multi-core processors, the parallelization is implemented by creating “threads” which represent separate tasks run by different

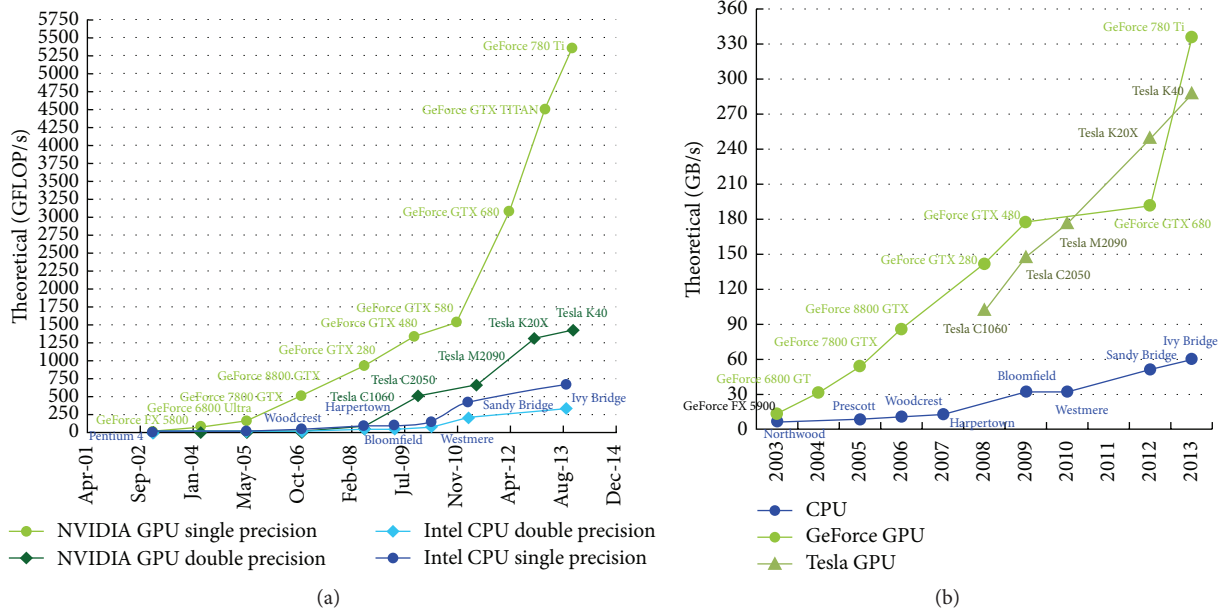


FIGURE 1: Comparison of computation capability of CPU and GPU: (a) floating-point operations per second (FLOP/s) for the CPU and GPU; (b) memory bandwidth for the CPU and GPU [13].

CPU cores. With multi-core CPUs, several existing or new programming models and environments can help users [10]. For example, OpenMP, Pthread, Cilk [11], and even MATLAB can be considered tools to help users implement programs on multi-core CPUs. Among those tools, OpenMP is adopted for the parallelization of the SCE-UA method on multi-core CPU systems owing to its simplicity and good efficiency.

Many-core GPU and multi-core CPU are two kinds of completely different hardware systems. The GPU is a highly parallel, multithreaded, many-core processor with tremendous computational horsepower and very high memory bandwidth, as illustrated by Figures 1(a) and 1(b) [12, 13]. NVIDIA introduced CUDA (compute unified device architecture), a general purpose parallel computing platform and programming model that leverages the parallel compute engine in NVIDIA GPUs to solve complex computational problems. CUDA guides the programmer to partition the problem into coarse subproblems that can be solved independently in parallel by blocks of threads and each subproblem into finer pieces that can be solved cooperatively in parallel by all threads within the block [13]. Therefore, we adopted CUDA Fortran as the tool for the parallelization of the SCE-UA method on many-core NVIDIA GPU systems.

The objectives of this paper are the following. (1) Rare previous literature is about the parallelization and acceleration of the SCE-UA method. We analyze which part of the SCE-UA method could be parallelized. We redesigned and accelerated the SCE-UA method in the algorithm level and made the method highly suited to the multi-core CPU and many-core GPU. (2) The multi-core CPUs and many-core GPUs have not been applied for the parallelization and acceleration of the SCE-UA method previously. We implement parallel SCE-UA on these two kinds of hardware systems by utilizing the OpenMP and CUDA Fortran.

(3) The Griewank benchmark function is used in this paper to test and compare the performances of the serial and parallel SCE-UA methods. According to the results of the comparison, some useful advises are given to direct how to properly use the parallel SCE-UA methods.

2. Methodology

2.1. The Serial SCE-UA Method (Serial-SCE-UA). The SCE-UA method is specifically designed to deal with the peculiarities encountered in environmental model calibration. The method is based on a synthesis of four concepts: (1) combination of deterministic and probabilistic approaches; (2) systematic evolution of a “complex” of points spanning the parameter space, in the direction of global improvement; (3) competitive evolution; (4) complex shuffling. The synthesis of these elements makes the SCE-UA method effective and robust, and also flexible and efficient. A detailed presentation of the theory underlying the SCE-UA algorithm could be found in Duan’s papers [5, 14]. Duan provides MATLAB and Fortran 77 SCE-UA codes on his official website. These two versions are serial codes and are implemented on single core CPU. They can be recognized as the standard SCE-UA codes. In this paper, the serial SCE-UA CPU code is revised from Duan’s MATLAB version and is implemented in Fortran 90. This serial SCE-UA CPU code is utilized as the base line for the performance comparisons.

2.2. The Parallel SCE-UA Method on Multi-Core CPUs

(OMP-SCE-UA) and Many-Core GPUs (CUDA-SCE-UA)

2.2.1. Overall Description. In this study, we proposed a parallel SCE-UA method and implement it on multi-core CPU

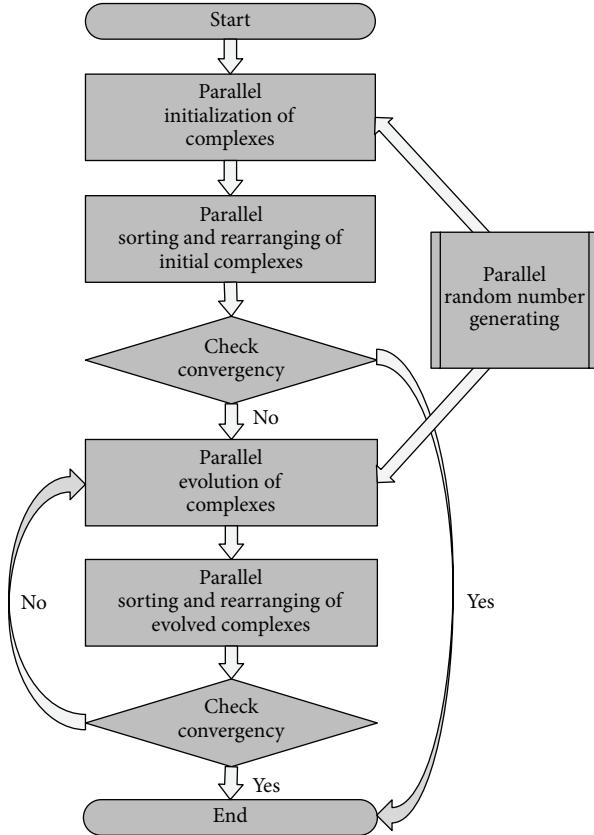


FIGURE 2: Flowchart of the parallel SCE-UA method.

by OpenMP and many-core GPU by CUDA Fortran, respectively. The SCE-UA method is inherently parallel and should be redesigned to implement the parallelization. According to the computation flow path of the SCE-UA algorithm, the following parts of the SCE-UA method are parallelizable: (1) initialization of complexes, (2) evolution of complexes, (3) random number generating, and (4) sorting and rearranging of complexes. The flowchart of the parallel SCE-UA method is shown in Figure 2.

2.2.2. Parallel Initialization of Complexes. Before the evolution of complexes, the SCE-UA method randomly generates a set of initial points to constitute the initial complexes where each point represents a potential solution for the problem. The generation steps include the generation of initial points and the computation of objective function value of each point. The generation of initial points can be parallelized and requires a parallel random number generator which will be described in Section 2.2.4. The computation of objective function value for each initial point is unrelated to other points and can also be parallelized. Supposing we need to generate n_{pt} initial points and their corresponding objective function values, we create n_{pt} threads on the CPU or GPU. In each thread, we compute the objective function value for the corresponding randomly generated point. By using multi-core CPU and many-core GPU, the n_{pt} threads can be executed in parallel to obtain the objective function values.

2.2.3. Parallel Evolution of Complexes. The evolution of complexes improves the objective function values by evolving n_{gs} complexes towards the global optimum. The process of complex evolution is inherently parallel and should be parallelized. For each complex evolution loop, we create n_{gs} threads to represent n_{gs} complexes and evolve these threads in parallel on the CPU or GPU to implement the parallel evolution. When the stopping criterion is satisfied, the complex evolution is stopped. In each complex evolution loop, for each complex, we perform the CCE (complex competitive evolution) and the points sequence rearranging for $nspl$ steps. The CCE contains three typical operations to imitate the genetic algorithm and the downhill simplex algorithm, which includes simplex choosing (the selection), the worst point reflection (the crossover), and the reflection failed point random regeneration (the mutation). In the mutation step, we need a parallel random number generator which is described in Section 2.2.4. The points sequence rearranging utilizes the quick sort algorithm to sort the evolved points in increasing objective function values and rearranges the point sequence according to the objective function values. After that, the algorithm is ready for the next round CCE operation.

2.2.4. Parallel Random Number Generating. During the initialization and evolution of complexes, we need to generate uniformly distributed random numbers for each thread. Because the initialization and evolution process is parallel, the random number generating process should be run in parallel. We design the following parallel random number generating method:

- (1) For each thread, we generate a random number sequence, respectively [15–17]. This method promises that the generation process for each thread is unrelated to other threads and guarantees the high quality of the generated random number sequence.
- (2) In order to avoid the correlation between different random number sequences and obtain better random characteristics, we adopt different randomly generated seeds for each thread and utilize the Mersenne twister random number generator instead of the widely used linear congruential generator [18, 19]. For each thread, a separately generated random seed is adopted and catered for the Mersenne twister random number generator to generate a random number sequence for the corresponding thread.

2.2.5. Parallel Sorting and Rearranging of Complexes. After the initialization or the shuffling evolution loop, the initial or evolved complexes should be sorted in increasing objective function values and rearranged according to their corresponding objective function values. Because the sorting and rearranging processes are inherently parallel, we should parallelize these processes by using the radix parallel sorting method [20, 21] and the parallel rearranging method. The parallel sorting and rearranging are also implemented on the multi-core CPU and the many-core GPU.

TABLE 1: Total execution time (seconds) of the Serial-SCE-UA.

n_{opt}	n_{gs}								
	4	8	16	32	64	128	256	512	1024
10	43.95	96.14	185.58	358.38	719.08	1388.17	2804.75	5688.64	11225.29
20	79.00	162.72	320.67	619.09	1201.86	2441.35	4880.35	9849.35	19492.42
30	130.04	252.29	484.13	919.92	1850.08	3697.84	7207.62	14263.88	28609.81
40	193.28	360.20	670.29	1238.20	2505.45	4777.02	9627.71	19040.44	37697.98
50	243.67	420.27	833.65	1580.19	3081.36	6235.98	12190.24	23760.53	46559.85

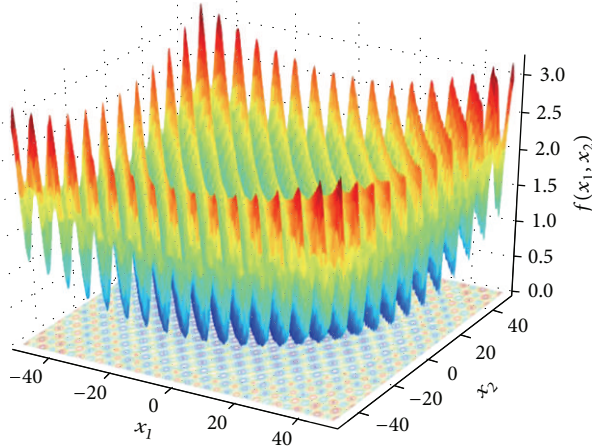


FIGURE 3: The two-dimensional Griewank function.

2.3. Experimental Studies of the Serial and Parallel SCE-UA

2.3.1. The Griewank Benchmark Function. The performance comparison of serial and parallel SCE-UA methods is based on the Griewank benchmark function. The Griewank global optimization problem is a multimodal minimization problem defined as follows:

$$f(x_1, x_2, \dots, x_n) = \frac{1}{4000} \sum_{i=1}^n x_i^2 - \prod_{i=1}^n \cos\left(\frac{x_i}{\sqrt{i}}\right) + 1. \quad (1)$$

Here, n represents the number of dimensions (i.e., the number of decision variables) and $x_i \in [-100, 100]$ for $i = 1, 2, \dots, n$. The global optimum of the Griewank problem is $f(x_1, x_2, \dots, x_n) = 0$ for $x_i = 0$ for $i = 1, 2, \dots, n$. As a simple example, the two-dimensional Griewank function is demonstrated in Figure 3. The Griewank problem is complex enough to test the global property of the SCE-UA and the dimension can be changed to test the performance of the SCE-UA. Therefore, we adopt it as the benchmark function in this study.

2.3.2. Settings for the Hardware and Software Utilized in This Study

(1) The Hardware Utilized in This Study. In this study, we utilized the Intel Core i7-4710HQ CPU with hyperthreading (4 CPU cores with 8 threads) and the NVIDIA Geforce GTX 850M (DDR3 version) (see Figure 4). We can see from Figure 4 that the i7-4710HQ CPU has 8 logical CPU cores and

the GTX 850M GPU has 640 CUDA GPU cores, which means the CPU and GPU can make full use of their computation capability by using 8 and 640 threads in parallel, respectively.

(2) Software Settings for This Study. The SCE-UA method has several algorithm parameters which control the convergence behavior of the algorithm. They are $maxn$, maximum number of objective function trials allowed before optimization is terminated; $kstop$, number of shuffling loops in which the objective function must improve by the specified percentage $pcento$ or else optimization will be terminated; $pcento$, percentage by which the objective function must change in the specified number of shuffling loops $kstop$ or else the optimization is terminated; $peps$, minimum parameter space allowed before optimization is terminated. For the purpose of fair comparison, we set the parameters as follows: $maxn =$ positive infinity; $kstop = 5$; $pcento = 0.1$; $peps = 0.000001$.

In order to analyze the performance of the serial and parallel SCE-UA algorithm, we need to adjust settings for the serial and parallel algorithm to test how the algorithm performs. These settings are n_{opt} , number of decision variables; n_{gs} , number of complexes; n_{obj} , loop number which is used to test the objective function computation overhead (each loop contains four floating-point arithmetic operations, i.e., including one addition, one subtraction, one multiplication, and one division. Larger n_{obj} corresponds to higher computation overhead). There is one thing that must be noted for the purpose of fair comparison, the time consumed by memory allocation on GPU, transfer between CPU and GPU, and deallocation from GPU that is also considered in this research. All the SCE-UA methods are implemented in single floating-point precision.

3. Results and Discussion

3.1. Performance Comparison Based on Total Execution Time. In this section, we test the performances of the serial and parallel SCE-UA methods based on the total execution time (in seconds). For the purpose of fair comparison, we set the $n_{obj} = 1000000$ for these comparisons. We adjust the n_{opt} and n_{gs} to test how the algorithm performs.

3.1.1. Serial-SCE-UA. The total execution time of the serial SCE-UA is demonstrated in Figure 5 and Table 1. As we can see, with the increasing of the n_{opt} , the total execution time increases. As for the increasing of the n_{gs} , the execution time varies from 43.95 s to 46559.85 s in proportion. Let $n_{opt} = 30$ as an example (the bolded line of Table 1); the n_{gs}

TABLE 2: Total execution time (seconds) of the OMP-SCE-UA.

<i>nopt</i>	<i>ngs</i>									
	4	8	16	32	64	128	256	512	1024	
10	13.32	14.96	26.51	50.48	96.56	189.85	366.68	729.57	1451.04	
20	23.63	24.60	43.21	81.76	162.38	321.86	638.98	1270.75	2530.29	
30	34.02	36.80	65.99	125.92	243.61	474.52	944.30	1877.73	3737.83	
40	49.39	47.56	88.61	165.91	337.02	641.63	1278.80	2488.18	4945.17	
50	74.37	63.01	112.41	210.94	420.48	798.60	1595.91	3177.03	6186.20	

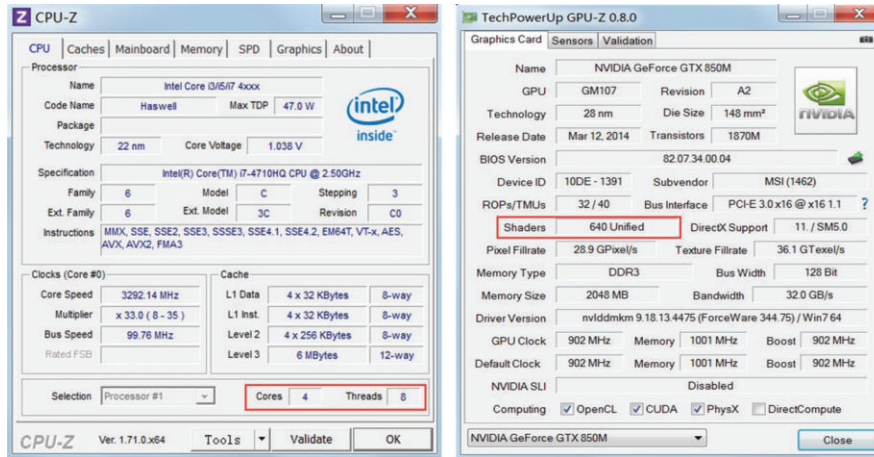


FIGURE 4: The CPU and GPU used in this study.

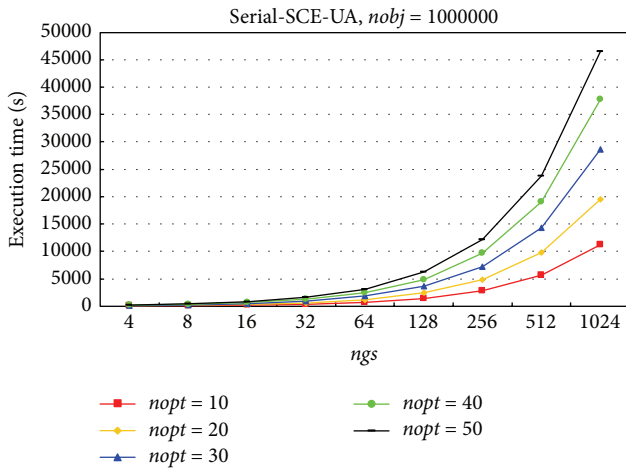


FIGURE 5: Total execution time (seconds) of the Serial-SCE-UA.

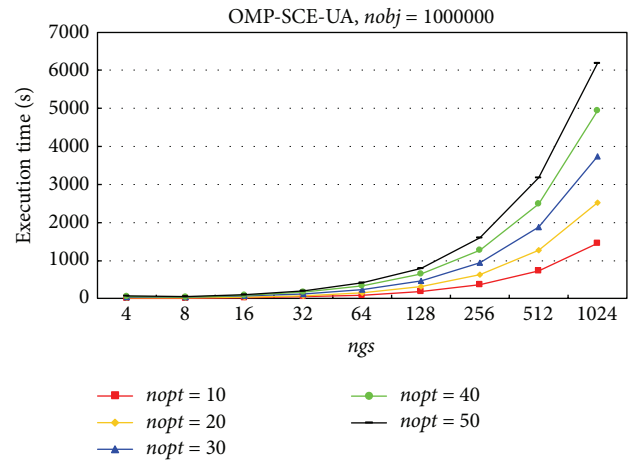


FIGURE 6: Total execution time (seconds) of the OMP-SCE-UA.

increases from 4 to 1024 with a multiple of two. We can observe that the total execution time increases from 130.04 s to 28609.81 s with approximately the same multiple of two. This is because the serial version only utilizes one CPU core; with the increasing of *ngs*, the total execution time of course increases with approximately the same proportion. For *ngs* < 16, the execution time is not doubled. This is mainly because of less computational overhead; the CPU resources used for the thread dispatch are relatively higher than the computation. The dispatch of threads cost relatively more time which makes the execution time not doubled.

3.1.2. *OMP-SCE-UA*. The total execution time of the OpenMP SCE-UA is demonstrated in Figure 6 and Table 2. As we can see, with the increasing of the *nopt*, the total execution time increases. As for the increasing of the *ngs*, the total execution time varies from 13.32 s to 6186.20 s. The time consumed by the OpenMP version is much less than the serial version. Different from the serial version, with the increasing of the *ngs* and when the *ngs* is smaller than 16, the total execution time increases not according to the same increasing multiple of the *ngs*. Let *nopt* = 30 as an example (the bolded line of Table 2); the *ngs* increases from 4 to 1024 with a multiple of

TABLE 3: Total execution time (seconds) of the CUDA-SCE-UA.

<i>nopt</i>	<i>ngs</i>								
	4	8	16	32	64	128	256	512	1024
10	224.62	228.95	241.62	251.60	245.62	247.45	260.40	264.61	267.10
20	406.99	412.23	409.77	412.14	414.13	396.97	416.59	420.15	424.20
30	670.82	648.42	604.67	626.22	629.26	611.52	619.27	623.42	624.14
40	980.73	937.47	886.81	860.83	805.71	814.37	814.33	818.35	839.48
50	1400.51	1173.31	1081.71	1078.16	1115.32	1046.00	1080.26	1053.03	1064.78

TABLE 4: Speed-up ratio of the OMP-SCE-UA versus the Serial-SCE-UA.

<i>nopt</i>	<i>ngs</i>								
	4	8	16	32	64	128	256	512	1024
10	3.30	6.43	7.00	7.10	7.45	7.31	7.65	7.80	7.74
20	3.34	6.61	7.42	7.57	7.40	7.59	7.64	7.75	7.70
30	3.82	6.86	7.34	7.31	7.59	7.79	7.63	7.60	7.65
40	3.91	7.57	7.56	7.46	7.43	7.45	7.53	7.65	7.62
50	3.28	6.67	7.42	7.49	7.33	7.81	7.64	7.48	7.53

TABLE 5: Speed-up ratio of the CUDA-SCE-UA versus the Serial-SCE-UA.

<i>nopt</i>	<i>ngs</i>								
	4	8	16	32	64	128	256	512	1024
10	0.20	0.42	0.77	1.42	2.93	5.61	10.77	21.50	42.03
20	0.19	0.39	0.78	1.50	2.90	6.15	11.72	23.44	45.95
30	0.19	0.39	0.80	1.47	2.94	6.05	11.64	22.88	45.84
40	0.20	0.38	0.76	1.44	3.11	5.87	11.82	23.27	44.91
50	0.17	0.36	0.77	1.47	2.76	5.96	11.28	22.56	43.73

two. We can observe that the total execution time increases from 34.02 s to 3737.83 s. When *ngs* is smaller than 16, the increasing multiple of total execution time is not two (less than two). When *ngs* is equal to or larger than 16, the increasing multiple is approximately equal to two. This is because the OpenMP version can utilize at most 8 CPU cores (the CPU used in this study has at most 8 cores). When the *ngs* is less than 16, the number of threads equals the CPU cores used. Larger *ngs* requires more CPU cores and the CPU can provide enough cores for the OMP-SCE-UA (when *ngs* is less than 16) to boost the performance. Therefore, the increasing multiple of total execution time is not two (less than two). However, when the *ngs* is equal to or larger than 16, with the increasing of *ngs*, the OMP-SCE-UA requires more CPU cores to boost the performance. However, there are only 8 CPU cores and the CPU cannot provide more computation resources for the OMP-SCE-UA to boost the performance. Therefore, the execution time increases with the same increasing multiple of the *ngs* (when *ngs* is equal to or larger than 16).

3.1.3. CUDA-SCE-UA. The total execution time of the CUDA SCE-UA is demonstrated in Figure 7 and Table 3. As we can see, with the increasing of the *nopt*, the total execution time increases. As for the increasing of the *ngs*, the total execution time varies from 224.62 s to 1400.51 s. The performance of the CUDA version is completely different from the serial and OpenMP version. With the increasing of the *ngs*, the execution time changes little and decreases a little. This is because

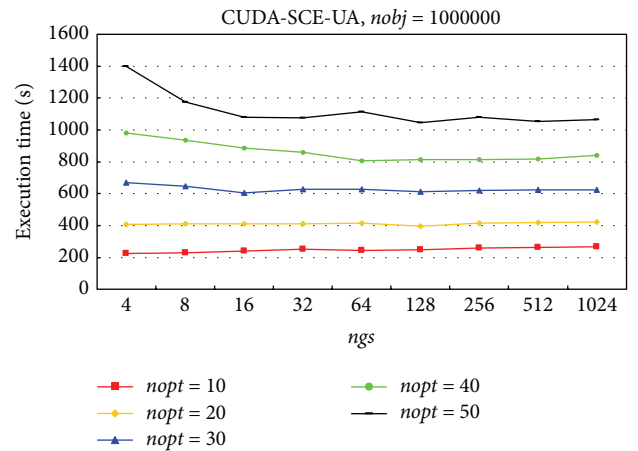


FIGURE 7: Total execution time (seconds) of the CUDA-SCE-UA.

with less *ngs* (i.e., less GPU threads) the GPU cannot hide the latency of the global memory access. The latency slows down the performance of the algorithm. With larger *ngs*, the GPU can hide the latency by launching many threads simultaneously and therefore boost the performance of the algorithm.

3.2. Speedup Ratio Analysis. The speedup ratio statistics are demonstrated in Figure 8 and Tables 4 and 5. As shown in figure and tables, the speedup ratio of the OpenMP version

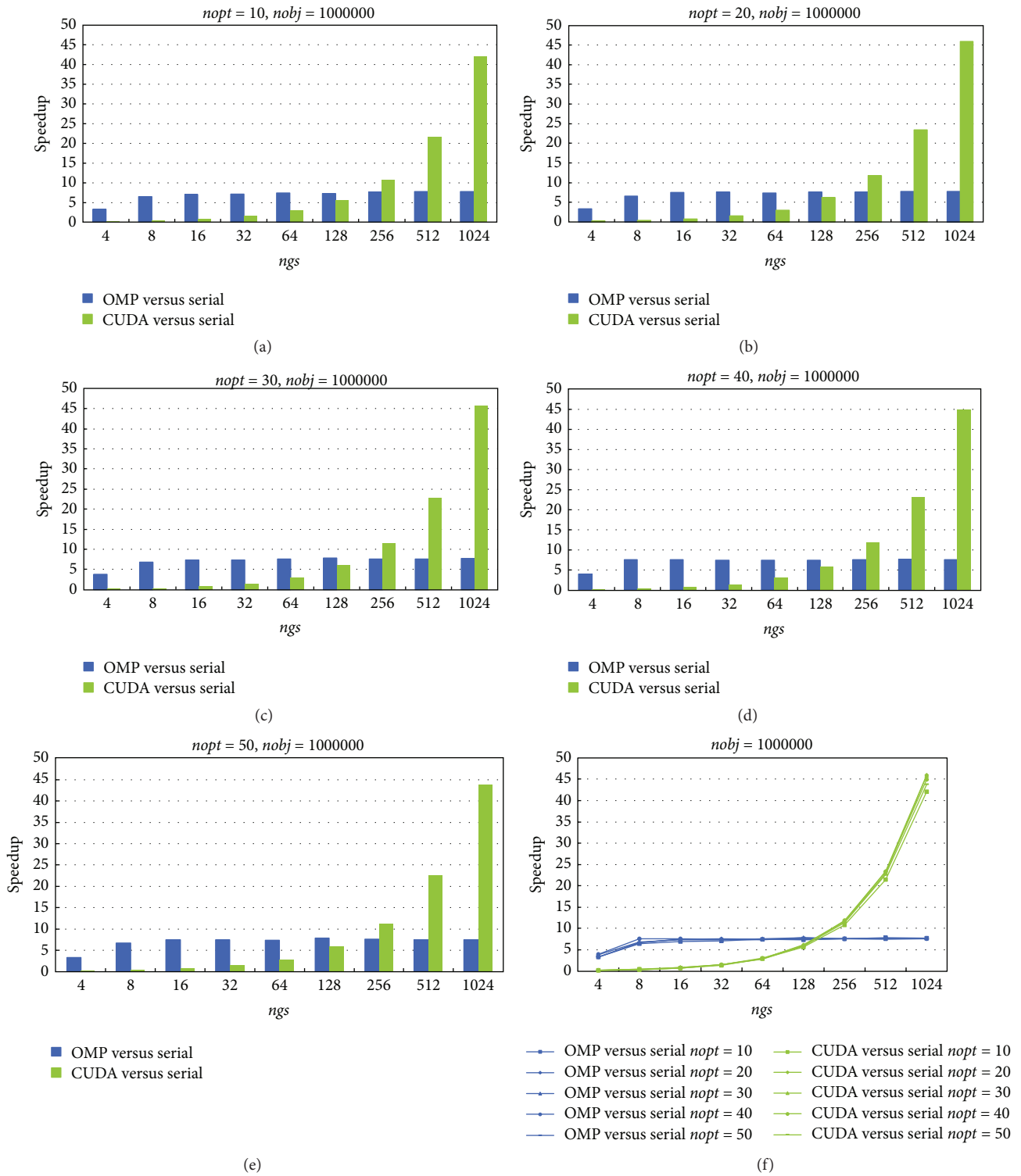


FIGURE 8: Speedup ratio of the parallel SCE-UA versus the serial SCE-UA.

varies from 3.28x to 7.81x, and the speedup ratio of the CUDA version varies from 0.17x to 45.95x. The speedup ratio of the OpenMP version is all less than 8x. The reason is as follows. The OpenMP program creates as many threads as possible to make full use of all the CPU cores. When the number of threads becomes larger than 8, because the CPU

utilized in this study has only 8 CPU cores, the creation, management, dispatching, and destroying of CPU threads consume more CPU resources and prevent the speedup ratio from being larger than 8x. As for the CUDA version, when ngs (that equals the number of threads created by the GPU) is small, the speedup ratio of the CUDA version is less than

the OpenMP version. This is because the clock speed of the CPU core is 2.5 GHz which is much higher than the clock speed of the GPU core (902 MHz). However, when ngs is very large ($ngs > 128$), the speedup ratio of the CUDA version becomes much higher than the OpenMP version. This is because the GPU has much more cores (640 CUDA GPU cores) than the CPU (only 8 CPU cores) and can launch much more parallel threads to boost the performance. As for the OpenMP version, the speedup ratio nearly reaches maximum value when ngs equals 8 and 16, and the speedup ratio cannot become larger by increasing the ngs . As for the CUDA version, the speedup ratio can become very large by increasing the ngs and the performance becomes much more satisfactory than the OpenMP version. At last, we can observe from Figure 8(f) that the $nopt$ (i.e., the number of decision variables) has very little impact on the speedup ratio. This means that although the total execution time increases with the increasing of the $nopt$, the speedup ratio has very little relationship with the $nopt$.

3.3. Analysis of the Impact of the Objective Function Computational Overhead. The relationship between the $nobj$ and the speedup ratio is demonstrated in Figure 9. We set $nopt = 20$. The ngs varies from 4 to 1024. We can see that with the increasing of the $nobj$ (i.e., the increasing of the objective function computational overhead), the speedup ratio becomes larger. There is one difference between the OpenMP and the CUDA version. With the increasing of the ngs and the $nobj$, the optimization problem becomes more complex and the computational overhead becomes heavier. The increasing extent of the speedup ratio of the OpenMP version is not very wide, and the speedup ratio is not higher than 8x. With the increasing of the ngs , the speedup ratio of the CUDA version becomes much higher than the OpenMP version, up to approximately 45x. These results show that the CUDA version performs much better than the OpenMP version under the condition of solving the problem with complex and high computational load objective function.

3.4. Optimization Accuracy Comparison. After checking the optimization results, we found that all the optimization problems converge to the global optimum. This fact shows that the parallel SCE-UA can find the global optimum with the same accuracy as the serial SCE-UA.

3.5. Some Useful Advices on How to Properly Utilize the Parallel SCE-UA Method. After carefully checking the results, we give some useful advices on how to properly utilize the parallel SCE-UA methods:

- (1) Both of the serial and parallel versions can give the correct optimization result. Therefore, for normal problems, the serial and parallel versions are both applicable and can converge to the global optimum. For simple problems ($ngs < 256$), the serial and parallel versions are all good to use but the parallel version may not obtain satisfactory speedup ratio because the overhead of creating, dispatching, and destroying of the threads is usually higher than the computation

overhead of the optimization algorithm. Therefore, for simple problems ($ngs < 256$), we recommend using the serial version.

- (2) The parallel version runs faster than the serial version especially for complex ($ngs > 128$) and high dimensional problems ($nopt > 40$). Therefore, we recommend using the parallel version for these problems. For complex problem with relatively small ngs ($ngs < 256$), we recommend using the OpenMP version to obtain a better performance. For complex problem with large ngs ($ngs > 128$), the CUDA version is a better choice. As for problems with very high objective function computational load, we recommend to use the CUDA version.
- (3) We should announce that the parallel version needs more memory than the serial version. This is because the parallel version needs to create arrays and vectors separately for each thread to ensure the correctness of parallel execution. Therefore, for very complex and very high dimensional problems, the parallel version may need much more memory and cause the memory overflow. We recommend using the 64-bit exe on 64-bit operating systems to cope with these kinds of problems because that 64-bit program can utilize more memory than the 32-bit program. The dimensionality of the problem ($nopt$) do not affect the speedup ratio very much; the only constraint is the memory size. Larger $nopt$ need more memory to store the large and complex population. Therefore, for these problems we recommend installing more CPU memory for the OpenMP version or adopting the Tesla GPU card (usually has more GPU memory) for the CUDA version to provide more memory to ensure the successful execution of the optimization.

4. Conclusions

In this paper, we proposed parallel SCE-UA method and implemented it on Intel multi-core CPU and NVIDIA many-core GPU by OpenMP and CUDA Fortran. The serial and parallel SCE-UA codes were optimized at the same level to ensure a fair comparison. The Griewank benchmark function was adopted in this paper to test and compare the performances of the serial and parallel SCE-UA methods. According to the results of the comparison, some useful advices were given to direct how to properly use the parallel SCE-UA. Three conclusions can be stated here:

- (1) Both of the serial and parallel versions can obtain the global optimum with a satisfactory probability. We can now produce reliable estimates of global optima for large complex optimization problems by both the serial and parallel versions of the SCE-UA methods.
- (2) The experimental studies were carried out by using the Griewank benchmark function. This benchmark function embodies many typical problems encountered in the global optimization. Therefore, the recommendations for the parallel SCE-UA derived

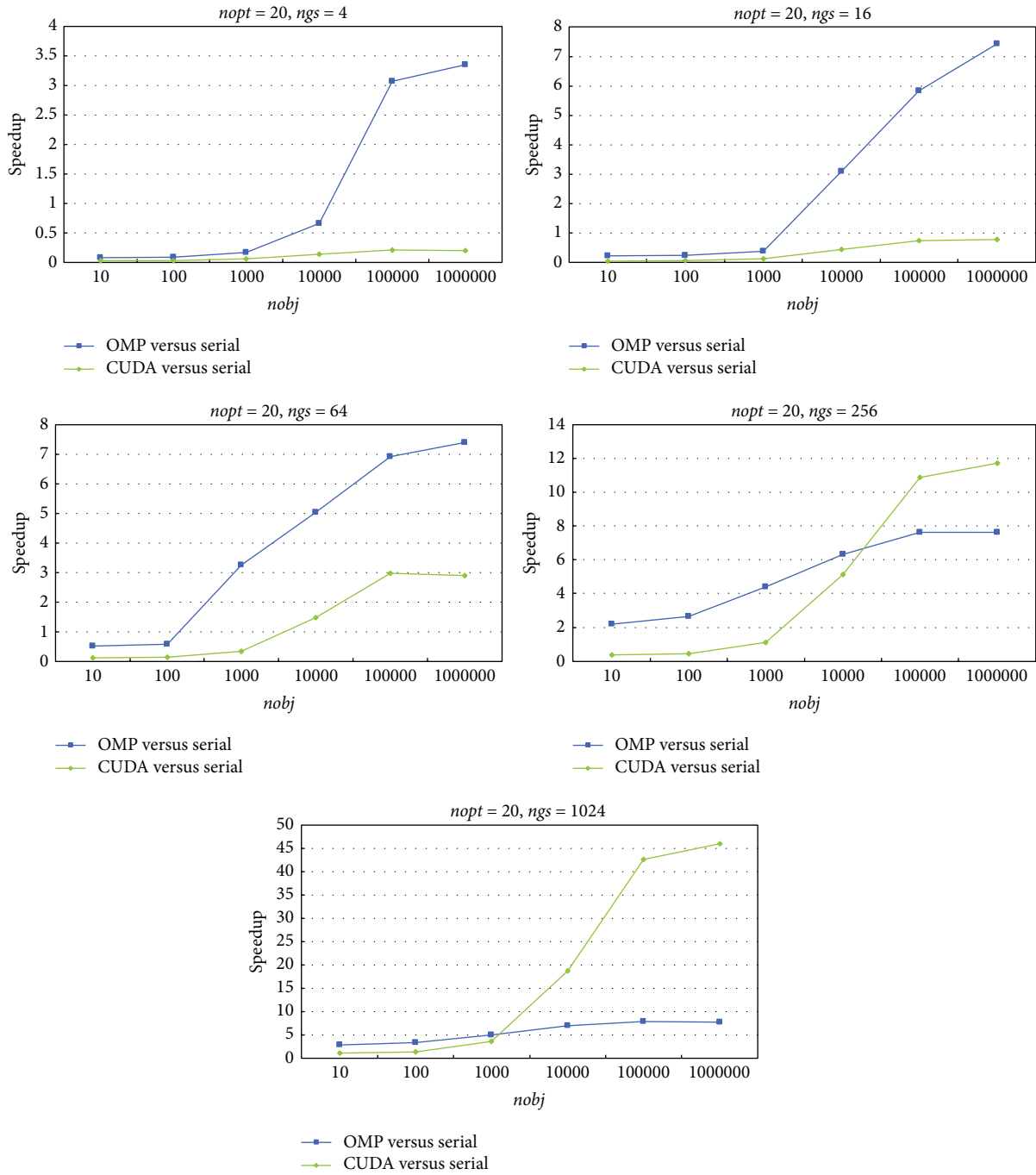


FIGURE 9: Relationship between the $nobj$ and the speedup ratio.

here can be recognized as guidelines for most applications.

- (3) With the advent of the newly developed parallel SCE-UA methods, we can now produce reliable and much faster estimates of global optima for large complex optimization problems by using the parallel SCE-UA methods. The OpenMP version is recommended to be used on medium problems and the CUDA version is recommended to be used on large problems.

Competing Interests

The authors declare that they have no competing interests.

Acknowledgments

This research was funded by the IWHR Scientific Research Projects of Outstanding Young Scientists “Research and Application on the Fast Global Optimization Method for the Xinanjiang Model Parameters Based on the High

Performance Heterogeneous Computing” (no. KY1605, JZ0145B052016), Specific Research of China Institute of Water Resources and Hydropower Research (Grant no. Fangji 1240), the Third Sub-Project: Flood Forecasting, Controlling and Flood Prevention Aided Software Development-Flood Control Early Warning Communication System and Flood Forecasting, Controlling and Flood Prevention Aided Software Development for Poyang Lake Area of Jiangxi Province (0628-136006104242, JZ0205A432013, and SLXMB200902), the NNSF of China, Numerical Simulation Technology of Flash Flood Based on Godunov Scheme and Its Mechanism Study by Experiment (no. 51509263), the NNSF of China, Study on the Integrated Assessment Model for Risk and Benefit of Dynamic Control of Reservoir Water Level in Flood Season (no. 51509268), and the NNSF of China, Estimation of Regional Evapotranspiration Using Remotely Sensed Data Based on the Theoretical VFC/LST Trapezoid Space (no. 41501415). The authors gratefully acknowledge the support of NVIDIA Corporation with the donation of the Tesla K40 GPU used for this research.

References

- [1] J. H. Holland, *Adaptation in Natural and Artificial Systems*, MIT Press, Cambridge, Mass, USA, 1992.
- [2] J. Kennedy and R. Eberhart, “Particle swarm optimization,” in *Proceedings of IEEE International Conference on Neural Networks*, pp. 1942–1948, Perth, Australia, December 1995.
- [3] Y. Shi and R. C. Eberhart, “Modified particle swarm optimizer,” in *Proceedings of the IEEE International Conference on Evolutionary Computation (ICEC ’98)*, pp. 69–73, May 1998.
- [4] S. Sorooshian, Q. Duan, and V. K. Gupta, “Calibration of rainfall-runoff models: application of global optimization to the Sacramento soil moisture accounting model,” *Water Resources Research*, vol. 29, no. 4, pp. 1185–1194, 1993.
- [5] Q. Duan, S. Sorooshian, and V. K. Gupta, “Effective and efficient global optimization for conceptual rainfall-runoff models,” *Water Resources Research*, vol. 28, no. 4, pp. 1015–1031, 1992.
- [6] Q. Duan, S. Sorooshian, and V. K. Gupta, “Optimal use of the SCE-UA global optimization method for calibrating watershed models,” *Journal of Hydrology*, vol. 158, no. 3–4, pp. 265–284, 1994.
- [7] P. O. Yapo, H. V. Gupta, and S. Sorooshian, “Automatic calibration of conceptual rainfall-runoff models: sensitivity to calibration data,” *Journal of Hydrology*, vol. 181, no. 1–4, pp. 23–48, 1996.
- [8] V. A. Cooper, V. T. V. Nguyen, and J. A. Nicell, “Evaluation of global optimization methods for conceptual rainfall-runoff model calibration,” *Water Science and Technology*, vol. 36, no. 5, pp. 53–60, 1997.
- [9] K. Eckhardt and J. G. Arnold, “Automatic calibration of a distributed catchment model,” *Journal of Hydrology*, vol. 251, no. 1–2, pp. 103–109, 2001.
- [10] L. Zheng, Y. Lu, M. Guo, S. Guo, and C.-Z. Xu, “Architecture-based design and optimization of genetic algorithms on multi- and many-core systems,” *Future Generation Computer Systems*, vol. 38, pp. 75–91, 2014.
- [11] R. D. Blumofe, C. F. Joerg, B. C. Kuszmaul, C. E. Leiserson, K. H. Randall, and Y. Zhou, “Cilk: an efficient multithreaded runtime system,” *Journal of Parallel and Distributed Computing*, vol. 37, no. 1, pp. 55–69, 1996.
- [12] G. Ruetsch and M. Fatica, *CUDA Fortran for Scientists and Engineers: Best Practices for Efficient CUDA Fortran Programming*, Morgan Kaufmann, 2013.
- [13] NVIDIA, *CUDA C Programming Guide: Design Guide*, PG-02829-001.v6.5, NVIDIA, Santa Clara, Calif, USA, 2014.
- [14] Q. Y. Duan, V. K. Gupta, and S. Sorooshian, “Shuffled complex evolution approach for effective and efficient global minimization,” *Journal of Optimization Theory and Applications*, vol. 76, no. 3, pp. 501–521, 1993.
- [15] L. Y. Barash and L. N. Shchur, “RNGSSELIB: program library for random number generation. More generators, parallel streams of random numbers and Fortran compatibility,” *Computer Physics Communications*, vol. 184, no. 10, pp. 2367–2369, 2013.
- [16] S. Gao and G. D. Peterson, “GASPRNG: GPU accelerated scalable parallel random number generator library,” *Computer Physics Communications*, vol. 184, no. 4, pp. 1241–1249, 2013.
- [17] K. G. Savvidy, “The MIXMAX random number generator,” *Computer Physics Communications*, vol. 196, pp. 161–165, 2015.
- [18] V. Demchik, “Pseudo-random number generators for Monte Carlo simulations on ATI graphics processing units,” *Computer Physics Communications*, vol. 182, no. 3, pp. 692–705, 2011.
- [19] S. Harase, “On the \mathbb{F}_2 -linear relations of Mersenne twister pseudorandom number generators,” *Mathematics and Computers in Simulation*, vol. 100, pp. 103–113, 2014.
- [20] S.-J. Lee, M. Jeon, D. Kim, and A. Sohn, “Partitioned parallel radix sort,” *Journal of Parallel and Distributed Computing*, vol. 62, no. 4, pp. 656–668, 2002.
- [21] T. Thanakulwarapas and J. Werapun, “An optimized bitonic sorting strategy with midpoint-based dynamic communication,” *Journal of Parallel and Distributed Computing*, vol. 84, pp. 37–50, 2015.

Research Article

Are GRACE-era Terrestrial Water Trends Driven by Anthropogenic Climate Change?

J. T. Fasullo,^{1,2} D. M. Lawrence,¹ and S. C. Swenson¹

¹National Center for Atmospheric Research, Boulder, CO 80301, USA

²Department of Atmospheric and Oceanic Sciences, University of Colorado, Boulder, CO 80309, USA

Correspondence should be addressed to J. T. Fasullo; fasullo@ucar.edu

Received 30 November 2015; Accepted 21 February 2016

Academic Editor: Sergio M. Vicente-Serrano

Copyright © 2016 J. T. Fasullo et al. This is an open access article distributed under the Creative Commons Attribution License, which permits unrestricted use, distribution, and reproduction in any medium, provided the original work is properly cited.

To provide context for observed trends in terrestrial water storage (TWS) during GRACE (2003–2014), trends and variability in the CESM1-CAM5 Large Ensemble (LE) are examined. Motivated in part by the anomalous nature of climate variability during GRACE, the characteristics of both forced change and internal modes are quantified and their influences on observations are estimated. Trends during the GRACE era in the LE are dominated by internal variability rather than by the forced response, with TWS anomalies in much of the Americas, eastern Australia, Africa, and southwestern Eurasia largely attributable to the negative phases of the Pacific Decadal Oscillation (PDO) and Atlantic Multidecadal Oscillation (AMO). While similarities between observed trends and the model-inferred forced response also exist, it is inappropriate to attribute such trends mainly to anthropogenic forcing. For several key river basins, trends in the mean state and interannual variability and the time at which the forced response exceeds background variability are also estimated while aspects of global mean TWS, including changes in its annual amplitude and decadal trends, are quantified. The findings highlight the challenge of detecting anthropogenic climate change in temporally finite satellite datasets and underscore the benefit of utilizing models in the interpretation of the observed record.

1. Introduction

Changes in water availability are a fundamental driver of impacts related to both climate variability and change, yet quantifying and understanding these variations remain a major challenge, in part due to the complexities inherent to their observation, simulation, and attribution on regional and global scales. While depletion of ground water can arise from a range of factors, including groundwater pumping, irrigation, and other agricultural and water management practices (e.g., [1]), changes in rainfall and temperature also exert a fundamental influence. As Earth warms and the atmosphere moistens, changes in the water cycle are anticipated including the spatial redistribution of precipitation favoring tropical and high latitudes, with potential deficits in many subtropical and midlatitude regions (e.g., [2]). An increasingly variable water cycle is also anticipated, with enhanced frequencies of flooding and drought (e.g., [3, 4]). From a practical perspective, these changes pose significant risks for water resources management and for ensuring future water availability [3, 5].

Motivated by the importance of these issues, the Gravity Recover and Climate Experiment (GRACE) satellite constellation was launched in March 2002 to monitor changes in near-surface mass, which over land relate primarily to the accumulation or depletion of terrestrial water storage (TWS). Providing the first global estimates at monthly resolution, GRACE revealed major changes across a range of timescales including strong seasonal shifts, interannual variations, and apparent trends [6]. While it is clear that both atmospheric and terrestrial hydrologic processes play central roles in these variations, many questions remain, chief amongst which is the potential role of anthropogenic climate change on GRACE-era trends.

Here, the roles of both internal variability (i.e., arising from interactions and chaotic variability within the climate system) and the anthropogenic forced response (i.e., driven primarily by human induced changes in atmospheric composition) are therefore investigated. This analysis is timely in that the GRACE record is likely nearing its end of life, with weakening of the satellite's batteries currently requiring

the instrument to be shut off for extended periods. Major questions nonetheless remain unanswered, such as whether the GRACE era is representative of recent decades generally. There are reasons to question whether this is the case given the strong negative phase of the Pacific Decadal Oscillation (PDO) that prevailed through much of the 2000s, accompanying a slowdown in global mean surface warming (e.g., [7]). The role of this and other modes such as the El Niño/Southern Oscillation (ENSO) and Atlantic Multidecadal Oscillation (AMO), in influencing regional TWS, remains similarly unexplored. A range of questions related to climate change can also be asked. Is an intensifying water cycle likely to result in a detectable increased annual cycle in TWS due to enhanced winter snow accumulation, advanced spring melt, and increased summer aridity? Changes in precipitation frequency and seasonality may also occur (e.g., [4]), if so, what is the expected magnitude of associated trends and how do they compare with internal variability? What is the capacity of trends in TWS to be sustained for decades and mitigate sea level rise, a question of particular relevance to the interpretation of the altimeter record [8]?

Addressing these questions solely through observations remains challenging due to the limited duration and accuracy of the global water cycle record and so here a hybrid approach is adopted in which model simulations are validated against available observations and then used to estimate the spatial patterns and magnitude of internal and forced variability on longer timescales. Section 2 describes the methods and data used, including the rationales for their selection, while Section 3 documents observed trends and modes of climate variability. Section 4 addresses questions raised by observed variability and documents patterns associated with the El Niño/Southern Oscillation (ENSO), the Pacific Decadal Oscillation (PDO), the Atlantic Multidecadal Oscillation (AMO), and the forced response under anthropogenic climate change. Section 5 documents simulated variability in key regions while Section 6 addresses characteristics of present-day and future global budgets, followed by a discussion of key findings and conclusions in Section 7.

2. Data and Methods

2.1. GRACE. GRACE fields are used from several sources including the recently released mass concentration solutions (Mascon, [9]) and various unconstrained spherical harmonic solutions [10–12]. The currently available GRACE Mascon record extends from April 2002 through November 2014 while spherical harmonic solutions extend through April 2015. The Mascon fields are provided on a 0.5° grid at quasi-monthly resolution while the spherical harmonic solutions are on a 1° grid, though the resolution of the grids on which these fields are reported is higher than the 300–400 km resolution of the GRACE retrievals. Due to battery management-related instrument outages starting in 2011, a few GRACE months are either missing or partially averaged across multiple months. The fields are thus converted to monthly means to allow for the removal of the climatological annual cycle prior to computing trends. Ice sheet surface mass variations in GRACE are not evaluated.

2.2. The CESM1-CAM5 Large Ensemble. The CESM1-CAM5 Large Ensemble (LE, [13]) consists presently of a 40-member set of simulations spanning 1920–2100 (with member 1 beginning in 1850). A round-off error magnitude (order 10^{-14} K) adjustment to tropospheric temperature is used to generate the ensemble spread in a series of branch runs that began in 1920. An extended 2000-yr coupled control run is also included as part of the ensemble. The LE is a unique resource for studying the terrestrial water budget's internal variability and distinguishing it from the forced response as, unlike many multimodel archives, it provides all terms necessary to compute the full terrestrial water budget and allows for an estimation of the forced response from the average of its ensemble members (whereas structural contrasts in multimodel archives preclude doing so). Moreover, the CESM consistently scores among the best models in representing the major modes of climate variability (e.g., [14]). Terrestrial water storage (TWS) is calculated from the LE's land component, version 4 of the Community Land Model (CLM4, [15]). TWS is calculated in CLM4 as the combination of soil liquid and ice, canopy water, snow water, river, and ground water fields. The annual cycle of TWS is captured reasonably in CLM4 [16]. As one of the limitations faced by GRACE is its inability to distinguish between these near-surface contributors to the mass budget, the CLM4 offers additional guidance as to how the various land water reservoirs contribute to observed variability. CLM4 does not include the effects of groundwater pumping, irrigation, or dams in its simulation of surface hydrology.

As an example of the fidelity of the CESM in representing internal variability, ENSO teleconnections are explored in Figure 1, where rainfall, near-surface winds, and 500 hPa vertical velocity (w_{500}) are regressed against Niño3.4 sea surface temperature (SST) for the LE 2000-yr control run and compared with fields from the European Center for Medium Range Weather Forecasts Interim Reanalysis [17]. The fields shown are based on the linear regression of 12-month means averaged from July through June (to account for the seasonality of ENSO) after removing any long-term trends. The general character of the observed and simulated patterns is very similar to anomalously strong rainfall in the central equatorial Pacific accompanied by deep convective vertical motion ($w_{500} < 0$) surrounded by regions of enhanced subsidence ($w_{500} > 0$) and suppressed rainfall, particularly over South America and Australia in a manner that is qualitatively consistent with recent observed variability (e.g., [18]). Extratropical rainfall associations are also generally consistent with those observed as positive regressions prevail over the Mediterranean, the southern tier of the North America, and southern South America. The major region of disagreement resides in Africa and the southern Atlantic Ocean, where regressed wind associations are too weak and rainfall regressions are positively biased in the CESM.

2.3. Indices of Variability. Key to understanding reported changes during the GRACE record is quantifying the character of internal climate modes. Here, indices are employed

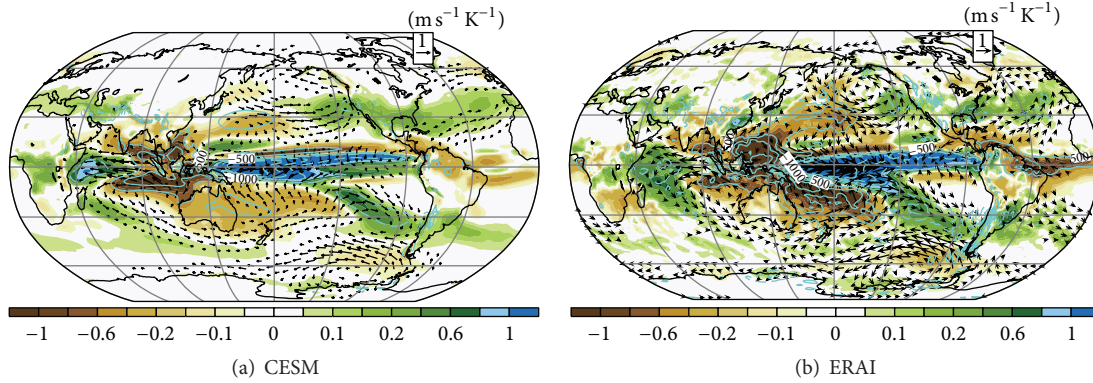


FIGURE 1: Niño3.4-regressed rainfall (colors, $\text{mm day}^{-1} \text{K}^{-1}$), near-surface winds (vectors), and midtropospheric vertical velocity (lines, $\text{mb day}^{-1} \text{K}^{-1}$) for (a) the CESM control run and (b) the ERA-Interim (ERA-I) reanalyses.

to characterize ENSO, the AMO, and the PDO in a consistent fashion across observations and models using methods employed in NCAR’s Climate Variability Diagnostics Package [14]. ENSO state is estimated from sea surface temperature in the Niño3.4 region (5°N – 5°S , 190°E – 120°W). The AMO index is computed by first removing the monthly global mean SST in ice-free regions (60°S – 60°N) to separate the Atlantic Multidecadal Oscillation (AMO) from global mean forced changes [19]. The index is calculated by averaging detrended annual mean SST anomalies over the North Atlantic Ocean (0° – 60°N , 80° – 0°W). This approach differs somewhat from earlier approaches in which the global mean was not considered, a distinction that is of particular relevance for the GRACE period as discussed in Section 3. The PDO index is derived from the standardized leading PC for the first EOF of detrended SST anomalies in the North Pacific Ocean (20°N – 70°N , 110°E – 80°W , [20, 21]).

3. Observed Trends and Variability

The GRACE-era TWS trends from 2003 to 2014 based on Mascon solutions are shown in Figure 2, with regions of disagreement in the sign of trends across the various GRACE products indicated by stippling. The trends are characterized by large increases in midlatitude North America, the Amazon and Parana basins of South America, western and southern Africa, eastern Australia, and portions of eastern Eurasia. Large decreases are evident across the northern and southern tiers of North America, Patagonia, western Eurasia, and the Himalaya. In general, the various GRACE products are consistent in depicting trends, with disagreement limited to regions of very small Mascon signals ($<2 \text{ mm yr}^{-1}$) and western Europe where GRACE retrievals are complicated by challenges in retrieving variability along coastlines. Many of the trends in the GRACE record are associated with significant potentially water cycle driven socioeconomic disruptions, including droughts in the southern United States [22], conflict in western Eurasia (e.g., [23]), and major floods in Australia that impacted sea level worldwide (e.g., [18]).

Many of the regions in which pronounced trends are evident in GRACE are also strongly influenced by internal

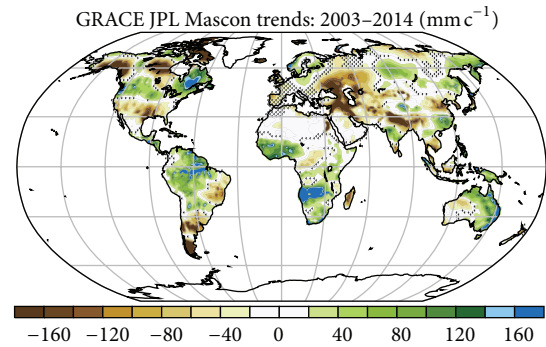


FIGURE 2: GRACE-era trends (2003–2014) in surface liquid water equivalent (mm c^{-1}) from JPL Mascon fields [9], stippled where the sign of the trend is inconsistent across available GRACE datasets (see text).

variability, particularly in rainfall [21, 24–26]. Understanding the evolution of such internal variability is therefore critical for interpreting trends and evolution of ENSO (using the Multivariate ENSO Index, MEI, [27]), the PDO, and AMO is shown in Figure 3. Here, the MEI is used instead of Niño3.4 SST as it is a more holistic measure of ENSO, being based on sea level pressure, surface wind, SST, surface air temperature, and cloud fraction, though both mean anomalies in the MEI (0.01) and Niño3.4 SST ($<0.01 \text{ K}$) are negligible for the GRACE era. As MEI is unavailable for model fields, Niño3.4 is used in assessing LE simulations. In contrast, the PDO and AMO are anomalous for much of the period with strong negative anomalies prevailing over much of the middle and latter part of the record. Of note, however, in regard to the AMO index, is the fact that when estimated by earlier techniques that do not account for global change [24] a positive anomaly is reported, whereas, once corrected for such effects, the methodology of Trenberth and Shea [19] shows it to be modestly negative (-0.33 K ; -0.35σ). Here, the latter convention is adopted in light of the strong high latitude warming that occurred during the early 2000s on a planetary scale (e.g., Figure 9 of [7]).

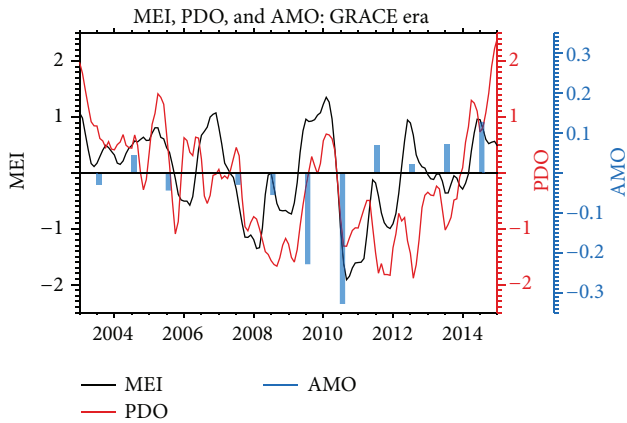


FIGURE 3: Evolution of ENSO (based on the MEI), the PDO, and AMO during the GRACE era.

4. Simulated Internal and Forced Variability

A major advantage of the LE is that it incorporates multiple realizations of the 20th and 21st centuries with a single model. It is therefore possible to accurately estimate the forced response by averaging together the various ensemble members to remove internal variability, the influence of which can be viewed as being random at any given point in time. Here, the forced response in TWS is estimated for the GRACE era and for the full span of the LE (Figure 4), with regions for which the sign of trends lacks consistency across at least three-quarters of the ensemble members which are stippled. The forced GRACE-era trend (Figure 4(a)) is very similar to the overall trend from the beginning of the LE to the present (1920 to 2014, not shown) and also exhibits many of the features of the forced response from 1920 to 2100 (Figure 4(b)), with reductions across western North America and the Amazon and Mediterranean regions and increases at high latitudes, across Australia and central Africa. However, there is substantial spread across ensemble members at regional and zonal mean scales, with the sign of trends in each being highly variable across such a brief period. In contrast, when the full LE record is considered, trends in these regions both intensify and become robust across ensemble members. Zonal mean averages across the full record become particularly robust, with increases at high latitudes and northern tropics (albeit with significant spatial structure) and decreases near 40°N and especially north of 70°N .

Given the strong role for internal variability suggested in Figure 3, the spatial structures of major modes over variability are explored (Figure 5) by regressing indices of climate variability against TWS in the LE's 2000-yr control simulation. For these internal variations, the CLM simulates the greatest contribution to TWS from liquid soil water and ground water terms. At high latitudes ($>50^{\circ}$), ice soil water and snow cover can also play an important role. For ENSO (Figure 5(a)), strong positive associations are evident across the southern tier of North America, southern South America, central Africa, and northern Eurasia, with deficits in northwestern

North America, north and eastern South America, west and east Africa, Southeast Asia, and Australia. The TWS pattern is therefore spatially correlated with rainfall teleconnections (Figure 1), suggesting a strong (and perhaps obvious) physical linkage between the two. Many of the features of ENSO are also evident in the PDO, which again may be expected given their strong interconnectedness [21]. Regional associations with the AMO however are in many ways distinct from those of ENSO and the PDO, with positive anomalies in northern South America, the Sahel, and southeast Asia, and negative anomalies spanning much of eastern North America and western Africa. Other features, such as regressions in the southwestern United States, central South America, western Eurasia, and south Africa, are qualitatively similar to ENSO and the PDO. The roles of these features contributing to observed changes will be discussed further in Section 7.

5. Regional Trends and Variability

The complexity of the spatial patterns in both the forced response and modes of internal variability motivates an analysis of the time evolution of regional structures (Figure 6). For global land, there is a positive TWS trend ($\sim 0.3 \text{ mm yr}^{-1}$), associated with an intensified and spatially redistributed water cycle (e.g., [2]), and an increase in internal variability (red dotted line), associated with elevated risks of episodic drought and flooding [3, 4]. The increase in variability between the early 20th and late 21st centuries is substantial ($\sim 50\%$).

Regional characteristics can deviate considerably from the global mean. In Australia (Figure 6(b)), a stronger increase in storage ($\sim 0.6 \text{ mm yr}^{-1}$) and a weaker increase in variability ($\sim 30\%$) than for global land are evident. A pronounced Amazonian drying trend (Figure 6(c), -1.2 mm yr^{-1}) accompanies an increase in variance ($\sim 35\%$). Trends that are less monotonic are also evident, such as for the Colorado river basin (Figure 6(d)), where an overall negative TWS trend (0.7 mm yr^{-1}) and increase in variance ($\sim 25\%$) are evident. The Mississippi river basin also dries (0.7 mm yr^{-1}) while evolution of its variance is in itself highly variable. In California (Figure 6(f)), mean changes are highly variable while variability increases ($\sim 35\%$).

6. Global Budgets

Among the most important indicators of climate change and a key driver of its associated impacts is sea level. Its interpretation however relies critically in being able to distinguish between contributions arising from changes in ocean heat content and mass. TWS is a key part of this budget (e.g., [6, 18]). Cazenave et al. [8] use a land model forced by estimated observed rainfall to speculate that the deceleration in sea level observed during the altimeter era has been driven by TWS increases over the past decade, requiring a net increase in TWS of almost 20 mm since 2003, relative to the prior decade. The plausibility of such a large increase is explored here. In addition, it has been hypothesized that an amplified annual cycle in TWS may serve as a useful indicator

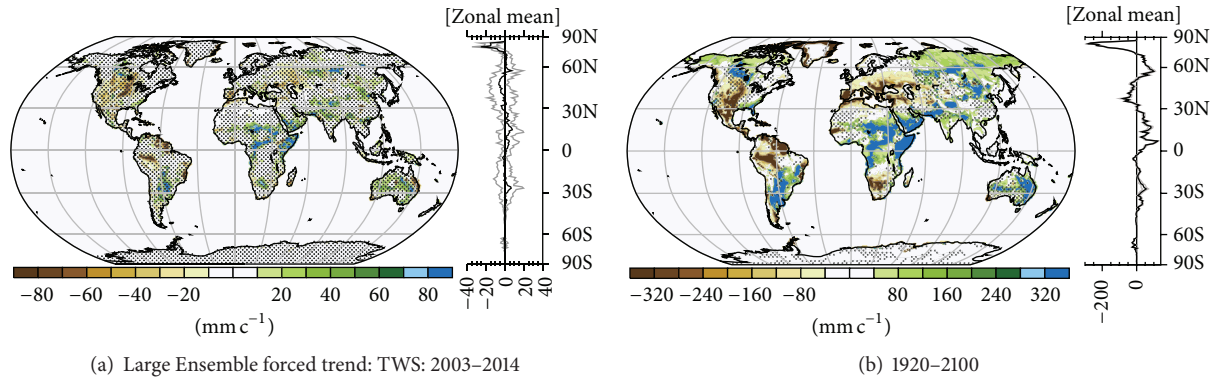


FIGURE 4: CESM forced trends in TWS from (a) 2003–2014 and (b) 1920–2100. Regions in which the ensemble mean trend is less than the standard deviation among ensemble members are stippled.

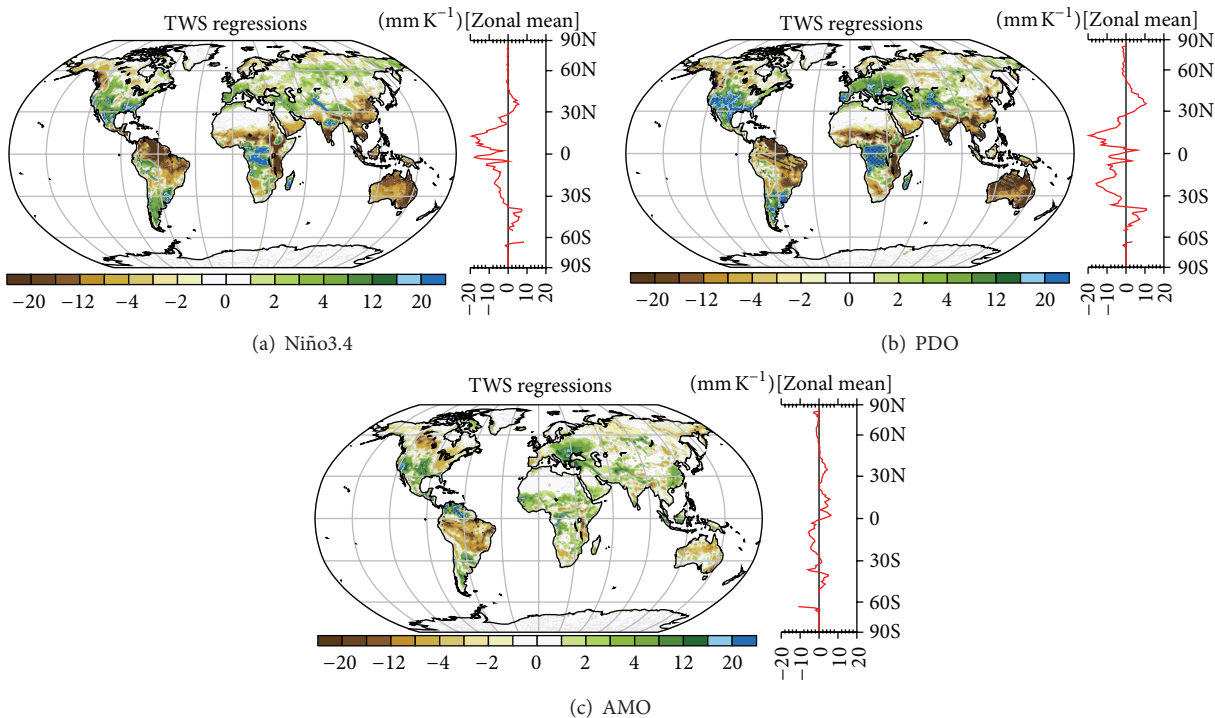


FIGURE 5: Regressed contributions to TWS of (a) ENSO as estimated from Niño3.4 SST and (b) the PDO and (c) AMO indices from the LE control run.

of global water cycle intensification [28] and that instruments such as GRACE may be able to detect such effects. The plausibility of these hypotheses is explored here using the LE simulations.

To address these issues, the frequency distribution of 10-yr global land TWS trends in the LE is explored (Figure 7). In this computation, the forced response estimated from the 40-member mean is removed from each ensemble member and running 10-yr trends are computed for all members from 1920 to 2100. Consideration is given to the states of ENSO, the PDO, and the AMO and the frequency of occurrence by intensity is then normalized. The mean (\bar{x}), standard deviation (σ), and skewness (γ) of the various distributions

are also shown. Overall, decadal trends in TWS tend to be small with σ of 3.1 mm dec^{-1} and are skewed positively (γ), likely due to skewness in the rainfall distribution ($\bar{x} = 0$ as the forced change is removed). Perhaps unexpectedly given their pronounced influence on regional budgets (e.g., Figure 5), modes of variability do not tightly constrain the mean global TWS trend, with \bar{x} being indistinguishable from zero for all modes. There is some suggestion however of increased γ for the negative phases of the PDO and AMO, which would be consistent with its expected influence in enhancing terrestrial rainfall floods. However, skewness also increases for El Niño events, for which no such strong expectation exists. Thus, while aspects of the TWS frequency distribution remain to

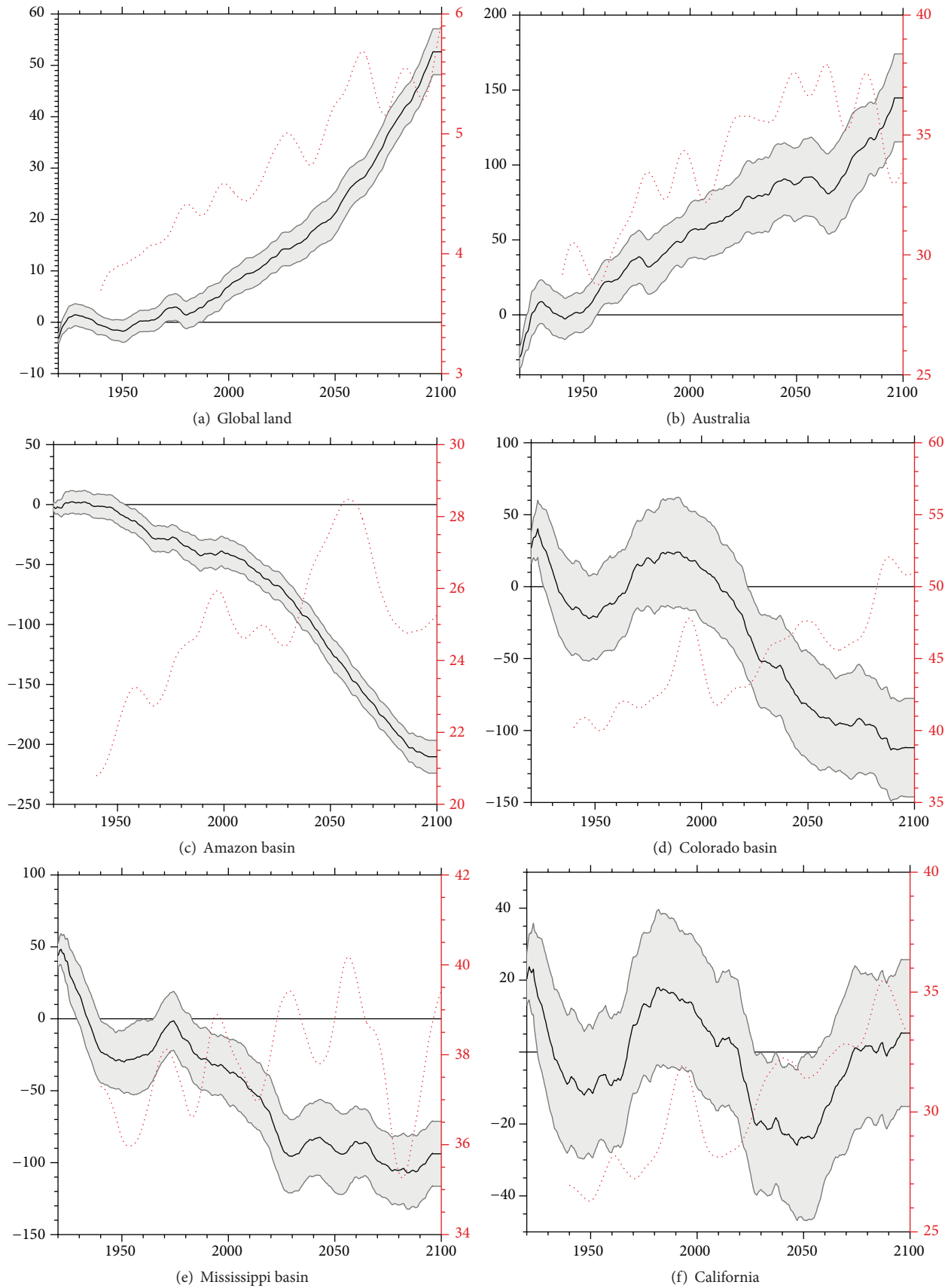


FIGURE 6: Time series of TWS anomalies and their interquartile range (shading) and internal variability based on the spread across ensemble members at each time (red dotted) for (a) global land, (b) Australia, (c) the Amazon, (d) Colorado, and (e) Mississippi river basins and (f) California. A 10-year running mean smoothing is applied to all time series.

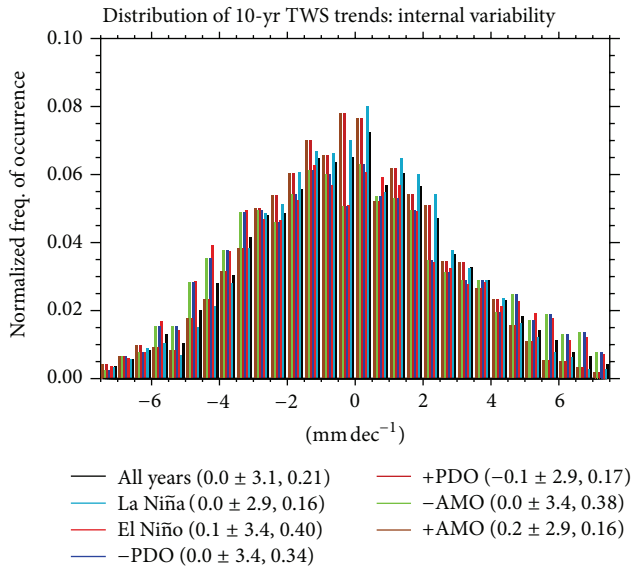


FIGURE 7: Normalized distribution of frequency of occurrence of decadal trends in TWS arising from internal variability (forced response removed) from 1920 to 2100. Also, indicated are the mean and standard deviation and skewness across trends.

be understood, the LE demonstrates two key points: mean decadal trends are rarely greater than 6 mm dec^{-1} and the trends themselves are not strongly determined by the internal modes of variability considered here.

Lastly, the capacity for using the annual amplitude of TWS as an indicator of the strength of the water cycle is explored. The mean annual cycles of global land TWS for the early 20th and late 21st centuries are shown in Figure 8 along with a $\pm 1\sigma$ range of interannual variability, where the annual mean (Figure 6(a)) has been removed. While the forms of the annual cycles are similar, the mean boreal summer minimum occurs about a month sooner (Aug. versus Sep.) and is about 1 mm lower in general in the late 21st versus early 20th centuries. These differences are statistically significant given the very large number of years included in the composite (1200). Nonetheless, the expectation that such a shift in the satellite record of a decade or so will be detectable is highly questionable, given the large internal variability inherent to the annual cycle and the demands of such detection related to the absolute accuracy of retrievals. These challenges are suggested by the LE despite a robust increase in terrestrial rainfall in the ensemble, increasing from about 2.24 mm d^{-1} to 2.44 mm d^{-1} , or about 9%, from 1920 to 2100.

7. Discussion and Conclusions

The GRACE record represents a remarkable technological achievement, providing significant and unprecedented insight into climate variability and change as manifested in terrestrial hydrology. However, the brevity of the record makes it subject to the same tensions that have long existed between the relatively short record of high-quality global satellite observations and the typically longer period of time

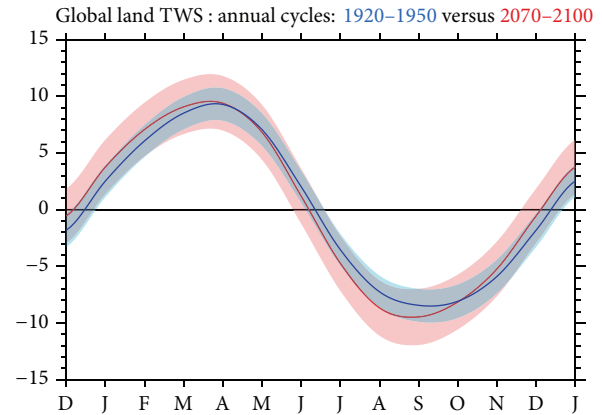


FIGURE 8: The mean annual cycle ($\pm 1\sigma$) of global land TWS (mm) from the early 20th (1920–1950, blue) to late 21st (2070–2100, red) centuries.

necessary to separate the convoluted influences of forced and internal variability. Here, it is shown that models can play a fundamental role in clarifying these roles, albeit with their own inherent uncertainties. Based on the LE, the forced TWS response is generally overwhelmed by internal variability on decadal timescales, with the AMO and PDO playing particularly influential roles in many key regions. Largely by chance, the negative phases of these modes (Figure 2) and related teleconnections (Figure 4) occurred during the GRACE era, leading to TWS increases in South America and Australia and drying in the southern tier of North and South America and western Eurasia. As these variations are also consistent with the forced response, internal variability has provided what can be reasonably viewed as an accelerated realization of many of the changes eventually anticipated under climate change. For example, this finding also suggests that there is little expectation that reported trends during subsequent satellite missions (e.g., the launch of GRACE Follow On is anticipated in 2017) will necessarily be similar to those observed during GRACE on decadal timescales. Nonetheless, despite this obfuscating role of internal variability, the sustained evolution of the forced response over time is likely to emerge into a clear pattern of response and be associated with significant shifts in terrestrial hydrology that can be either obscured or enhanced by internal variability at any given time, portending significant future impacts.

Examining global budgets, a number of findings also appear to be robust. Of particular note is the fact that the LE suggests that decadal trends in TWS rarely exceed 5 mm and are not strongly influenced by the PDO, AMO, or ENSO. Rather significant, apparently random scatter exists in the distribution of decadal trends. Explanations for recent sea level trends based on TWS (e.g., [8]) increases arising from the influence of the PDO therefore appear to be improbable according to the LE and alternative hypotheses should be explored. Similarly, evidence for the assertion that the seasonal cycle of TWS may act as a useful indicator of future water cycle intensification is found to be weak, as it is undermined by the large monthly variability and small signal that are anticipated as the water cycle strengthens.

In addition to robust global-scale changes, variability on regional scales shows an increase in many regions according to the LE. The realization of these regional changes in coming decades is likely to be much more uncertain than many of the findings above, however, due to structural model uncertainties, potential associated error, and the increased influence of internal variability on regional changes, even on multidecadal timescales (e.g., [29]).

Lastly, GRACE has provided a data record that is likely to yield additional benefits far into the future. The fields have provided developers with a new dataset that they can use to scrutinize and develop models [30], allowing for increased fidelity in simulating the movement and exchanges of moisture at the land surface. Given the importance of water in many terrestrial processes (e.g., carbon, vegetation) and its coupling to the atmosphere, the benefits of these improvements are expected to extend well beyond TWS simulation alone. While many of these improved models have yet to be used for large-scale projects such as the LE, it is only a matter of time before the insights gained and associated legacy of GRACE reach their full potential.

Competing Interests

The authors declare that they have no competing interests.

Acknowledgments

Dr. Fasullo's participation in this work was funded by NSF Award ID 1243125, NASA Award no. NNH11ZDA001N, and DOE Award ID DE-SC0012711. NCAR is sponsored by the National Science Foundation.

References

- [1] M. Kummu, P. J. Ward, H. De Moel, and O. Varis, "Is physical water scarcity a new phenomenon? Global assessment of water shortage over the last two millennia," *Environmental Research Letters*, vol. 5, no. 3, Article ID 034006, 2010.
- [2] W. K.-M. Lau, H.-T. Wu, and K.-M. Kim, "A canonical response of precipitation characteristics to global warming from CMIP5 models," *Geophysical Research Letters*, vol. 40, no. 12, pp. 3163–3169, 2013.
- [3] T. G. Huntington, "Evidence for intensification of the global water cycle: review and synthesis," *Journal of Hydrology*, vol. 319, no. 1–4, pp. 83–95, 2006.
- [4] K. E. Trenberth, "Changes in precipitation with climate change," *Climate Research*, vol. 47, no. 1–2, pp. 123–138, 2011.
- [5] J. S. Famiglietti and M. Rodell, "Water in the balance," *Science*, vol. 340, no. 6138, pp. 1300–1301, 2013.
- [6] J. T. Reager, A. S. Gardner, J. S. Famiglietti, D. N. Wiese, A. Eicker, and M. H. Lo, "A decade of sea level rise slowed by climate-driven hydrology," *Science*, vol. 351, no. 6274, pp. 699–703, 2016.
- [7] K. E. Trenberth and J. T. Fasullo, "An apparent hiatus in global warming?" *Earth's Future*, vol. 1, no. 1, pp. 19–32, 2013.
- [8] A. Cazenave, H.-B. Dieng, B. Meyssignac, K. Von Schuckmann, B. Decharme, and E. Berthier, "The rate of sea-level rise," *Nature Climate Change*, vol. 4, no. 5, pp. 358–361, 2014.
- [9] M. M. Watkins, D. N. Wiese, D.-N. Yuan, C. Boening, and F. W. Landerer, "Improved methods for observing Earth's time variable mass distribution with GRACE using spherical cap mascons," *Journal of Geophysical Research B: Solid Earth*, vol. 120, no. 4, pp. 2648–2671, 2015.
- [10] F. W. Landerer and S. C. Swenson, "Accuracy of scaled GRACE terrestrial water storage estimates," *Water Resources Research*, vol. 48, no. 4, Article ID W04531, 2012.
- [11] B. D. Tapley, S. Bettadpur, M. Watkins, and C. Reigber, "The gravity recovery and climate experiment: mission overview and early results," *Geophysical Research Letters*, vol. 31, no. 9, Article ID L09607, 2004.
- [12] C. Siemes, P. Ditmar, R. E. M. Riva, D. C. Slobbe, X. L. Liu, and H. H. Farahani, "Estimation of mass change trends in the Earth's system on the basis of GRACE satellite data, with application to Greenland," *Journal of Geodesy*, vol. 87, no. 1, pp. 69–87, 2013.
- [13] J. E. Kay, C. Deser, A. Phillips et al., "The Community Earth System Model (CESM) large ensemble project: a community resource for studying climate change in the presence of internal climate variability," *Bulletin of the American Meteorological Society*, vol. 96, no. 8, pp. 1333–1349, 2015.
- [14] A. S. Phillips, C. Deser, and J. Fasullo, "A new tool for evaluating modes of variability in climate models," *EOS*, vol. 95, no. 49, pp. 453–455, 2014.
- [15] D. M. Lawrence, K. W. Oleson, M. G. Flanner et al., "Parameterization improvements and functional and structural advances in version 4 of the Community Land Model," *Journal of Advances in Modeling Earth Systems*, vol. 3, no. 3, Article ID M03001, 2011.
- [16] D. M. Lawrence, K. W. Oleson, M. G. Flanner et al., "The CCSM4 land simulation, 1850–2005: assessment of surface climate and new capabilities," *Journal of Climate*, vol. 25, no. 7, pp. 2240–2260, 2012.
- [17] D. Dee, S. M. Uppala, A. J. Simmons et al., "The ERA-Interim reanalysis: configuration and performance of the data assimilation system," *Quarterly Journal of the Royal Meteorological Society*, vol. 137, no. 656, pp. 553–597, 2011.
- [18] J. T. Fasullo, C. Boening, F. W. Landerer, and R. S. Nerem, "Australia's unique influence on global sea level in 2010–2011," *Geophysical Research Letters*, vol. 40, no. 16, pp. 4368–4373, 2013.
- [19] K. E. Trenberth and D. J. Shea, "Atlantic hurricanes and natural variability in 2005," *Geophysical Research Letters*, vol. 33, no. 12, Article ID L12704, 2006.
- [20] N. J. Mantua, S. R. Hare, Y. Zhang, J. M. Wallace, and R. C. Francis, "A Pacific interdecadal climate oscillation with impacts on salmon production," *Bulletin of the American Meteorological Society*, vol. 78, no. 6, pp. 1069–1079, 1997.
- [21] C. Deser, A. S. Phillips, R. A. Tomas et al., "ENSO and Pacific decadal variability in the community climate system model version 4," *Journal of Climate*, vol. 25, no. 8, pp. 2622–2651, 2012.
- [22] T. R. Karl, B. E. Gleason, M. J. Menne et al., "U.S. temperature and drought: recent anomalies and trends," *Eos, Transactions American Geophysical Union*, vol. 93, no. 47, pp. 473–474, 2012.
- [23] P. H. Gleick, "Water, drought, climate change, and conflict in Syria," *Weather, Climate, and Society*, vol. 6, no. 3, pp. 331–340, 2014.
- [24] D. B. Enfield, A. M. Mestas-Nuñez, and P. J. Trimble, "The Atlantic multidecadal oscillation and its relation to rainfall and river flows in the continental U.S.," *Geophysical Research Letters*, vol. 28, no. 10, pp. 2077–2080, 2001.
- [25] R. Zhang and T. L. Delworth, "Impact of Atlantic multidecadal oscillations on India/Sahel rainfall and Atlantic hurricanes,"

Geophysical Research Letters, vol. 33, no. 17, Article ID L17712, 2006.

- [26] J. R. Knight, C. K. Folland, and A. A. Scaife, "Climate impacts of the Atlantic multidecadal oscillation," *Geophysical Research Letters*, vol. 33, no. 17, Article ID L17706, 2006.
- [27] K. Wolter and M. S. Timlin, "El Niño/Southern Oscillation behaviour since 1871 as diagnosed in an extended multivariate ENSO index (MEI.ext)," *International Journal of Climatology*, vol. 31, no. 7, pp. 1074–1087, 2011.
- [28] I. M. Held and B. J. Soden, "Robust responses of the hydrological cycle to global warming," *Journal of Climate*, vol. 19, no. 21, pp. 5686–5699, 2006.
- [29] C. Deser, A. S. Phillips, M. A. Alexander, and B. V. Smoliak, "Projecting North American climate over the next 50 years: uncertainty due to internal variability," *Journal of Climate*, vol. 27, no. 6, pp. 2271–2296, 2014.
- [30] S. C. Swenson and D. M. Lawrence, "GRACE-based assessment of interannual groundwater dynamics in the Community Land Model," *Water Resources Research*, vol. 51, no. 11, pp. 8817–8833, 2015.

Research Article

Trends in Extreme Precipitation Indices in Iran: 1951–2007

**Robert C. Balling Jr.,¹ Mohammad Sadegh Keikhosravi Kiany,²
Shouraseni Sen Roy,³ and Javad Khoshhal²**

¹*School of Geographical Sciences and Urban Planning, Arizona State University, Tempe, AZ 85287, USA*

²*Faculty of Geographical Sciences and Planning, University of Isfahan, Isfahan, Iran*

³*Department of Geography and Regional Studies, University of Miami, Coral Gables, FL 33146, USA*

Correspondence should be addressed to Robert C. Balling Jr.; robert.balling@asu.edu

Received 1 October 2015; Revised 13 December 2015; Accepted 14 January 2016

Academic Editor: Roberto Fraile

Copyright © 2016 Robert C. Balling Jr. et al. This is an open access article distributed under the Creative Commons Attribution License, which permits unrestricted use, distribution, and reproduction in any medium, provided the original work is properly cited.

We investigate trends in extreme precipitation in Iran for 1951–2007 using the recently released APHRODITE daily rainfall time series. We find that seven different indices of extreme precipitation all show an upward trend through the study period. The seven different precipitation indices include annual precipitation total, number of days above a certain threshold, maximum precipitation received over a certain period of time, maximum one-day precipitation, and number of days with precipitation above the 90th percentile. A principal components analysis reveals one eigenvector explaining much of the variance in the seven indices and reveals that this component exhibits a strong upward trend for the whole of Iran. On a regional level, we find that the upward trend in extreme precipitation has a strong southwest-to-northeast gradient across the country for all the indices. We repeated all the analyses for 42 stations across the country to compare with the results from the gridded data; trends in extreme rainfall generated from the station data compare favorably with the results from the APHRODITE daily rainfall time series thereby reinforcing the robustness of our conclusions.

1. Introduction

An extreme event is generally defined as the occurrence of a weather or climate event above or below a threshold value near the upper or lower ends of the range of observed values for a specific variable. Some of the main findings from the latest report on climate change and a special report on extreme events from the Intergovernmental Panel on Climate Change indicate a greater consensus within scientific literature about a likely increase in the frequency and intensity of heavy precipitation events over land areas since 1950, with a likely increase in the frequency of heavy precipitation or proportion of heavy precipitation in the 21st century. Additionally, there is medium confidence about the anthropogenic influence on the intensification of extreme precipitation on the global scale [1, 2]. In a comprehensive study examining the spatial patterns of precipitation extremes, Alexander et al. [3] reported a significant increase in precipitation extremes, with less spatially coherent patterns compared with trends

in extreme temperatures. In view of the widespread impacts of the extreme events on human, ecological, and/or physical systems, there is increased focus on the long-term trends of such events across the globe. The majority of studies based on observational data indicate a general increase in extreme heavy precipitation events, which is attributed to anthropogenic forcing caused by increased levels of moisture in the atmosphere and warmer temperatures overall [4].

Indeed, enhanced levels of water vapor due to warmer oceans in the lower latitudes were found by Trenberth et al. [5]. This has been further confirmed by increasing trends in specific humidity at the global level since 1970 [6, 7]. Additionally, results from CMIP3 and CMIP5 simulations also show an increase in the globally averaged 20-year return values of annual maximum 24-hour precipitation amounts at approximately 6 to 7% for each °C of global average warming [8, 9]. Several studies have highlighted the significant role of large scale circulation patterns on the positive trends in extreme precipitation events also [10, 11].

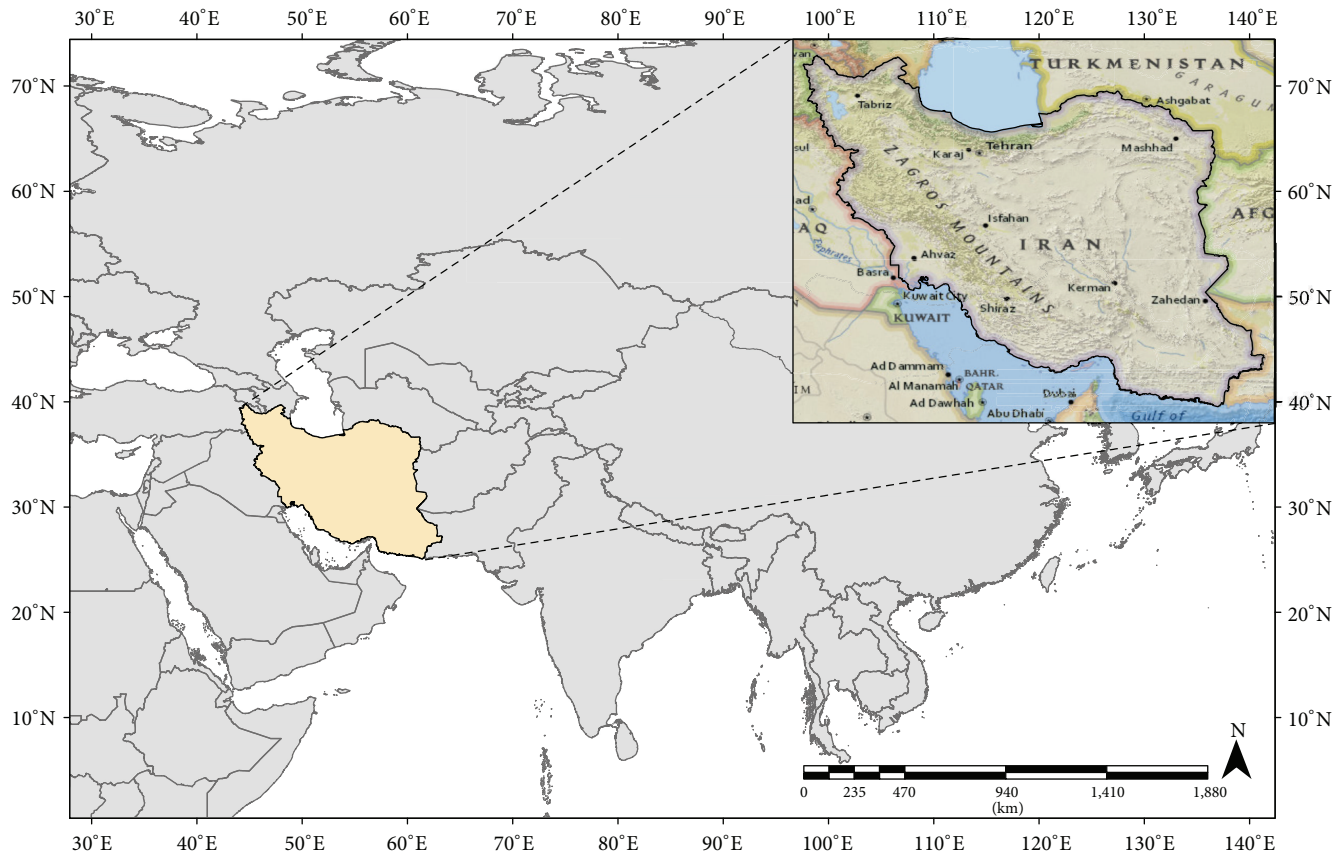


FIGURE 1: Location of Iran with stylized topographic depiction. Elevation ranges from -28 m near the Caspian Sea to 5610 m atop Mt. Damavand.

There are significant variations in long-term trends in precipitation regionally, with most of the continents, except North America and Europe, showing medium confidence in increasing trends in the frequency and intensity of observed heavy precipitation events [12]. Additionally, the majority of the land areas show an increase in extreme events during the summer season, except Europe which experienced increasing trends during the winter season [12]. Some of the specific regional level studies for extreme precipitation events show likely increases in North America [13–15] and South America [14, 16] for the entire 20th century. In the case of Europe and the Mediterranean region, the trends were mixed with most of the increase observed during the winter season and decreasing trends in the summer season precipitation [17–19]. Most of Asia and Oceania experienced mixed trends, with a greater proportion of the region showing a positive trend in extreme precipitation events [20–24]. Additionally, in the case of Africa, there were no clear significant trends [12, 25]. However, on the other hand there are a limited number of studies examining the trends in extreme precipitation patterns in the Middle East, likely due to the lack of long-term data, where Iran, the main focus of this study, is located. One of the few studies includes an analysis of station level precipitation across Iran in which Alijani et al. [26] found more than 20% of the land area exposed

to the risk of extreme rainfall. Specifically the hot, dry southern coast and the western slopes of the main north-south range, the Zagros Mountains, experienced the most frequent heavy rainfall events. Furthermore, Rahimzadeh et al. [27] examined extreme temperatures and precipitation across 27 synoptic stations across Iran. The results of their analysis indicated marked negative trends in cool days and cool nights, diurnal temperature range (DTR), and positive trends in warm days and tropical nights. Recently, with the advent of gridded data developed from station level measurements at high spatial resolutions, it has become possible to conduct detailed analysis of extreme precipitation events over these regions. Accordingly, in the present study we have analyzed trends in extreme precipitation for Iran which represents a location with precipitation coming largely from cool-season cyclonic events and limited warm-season convective precipitation.

2. Study Area: Iran

Iran is located between 25° and 40° N and 45° and 60° E and is a mountainous country bordering the Gulf of Oman, the Persian Gulf, and the Caspian Sea (Figure 1). The total area of Iran is 1.648×10^6 km² which represents 0.32 percent of the Earth's surface. Overall, sixty percent of Iran is covered

by mountains, with the central part of the country consisting of two dry deserts: the Dasht-e-Kavir and the Dasht-e-Lut. The Alborz range in the north, close to the Caspian Sea, extends in an east–west direction with a maximum elevation of approximately 5000 m. The Zagros Mountains are aligned in a northwest-to-southeast direction and reach a maximum elevation of approximately 3500 m. These two ranges play a significant role in determining the nonuniform spatial and temporal distribution of precipitation across the entire country [28]. For instance, the high ranges of the Alborz Mountains in the north and Zagros Mountains in the west inhibit much of the moisture available from adjacent water bodies from reaching the interior of the country. Thus, the interior parts of the country receive much less precipitation. Most of the interior slopes of the Zagros Mountains experience a rain shadow effect with annual rainfall much less than their western counterparts. More than half of the country receives less than 200 mm of precipitation, with some regions that get less than 50 mm annually [26].

Over the past decade, important papers have been published focusing on trends in precipitation across Iran (e.g., [29, 30]). The analysis of station level precipitation data revealed a decreasing trend in annual rainfall at 67% of the stations, while an increasing trend was observed in the 24 hr maximum rainfall at 50% of the stations by Modarres and Sarhadi [29]. Recently, Tabari and Talaei [31] studied temporal trends in the annual rainfall time series in the west, south, and southwest of Iran during 1966–2005. The results revealed no visible rainfall trends in the region for their study period. Soltani et al. [32] investigated annual and monthly trends in rainfall amount, number of rainy days, and maximum rainfall in 24 h based on the data collected at 33 synoptic stations in Iran. The results indicated that there are no significant linear trends in monthly rainfall at most of the synoptic stations. Some'e et al. [33] investigated the spatiotemporal trends and variability of precipitation data from 28 synoptic stations in Iran on the annual and seasonal timescales for the period 1967–2006. Their results revealed negative trends in annual precipitation at 22 sites (79%), but only three sites had a statistically significant negative trend in precipitation. However, a subsequent study by Razi'ei et al. [34] using the gridded APHRODITE dataset found an upward trend in daily annual precipitation in most of Iran. Talaei [35] analyzed the annual, seasonal, and monthly rainfall time series at seven rain gauge stations in Hamadan Province located in the west of Iran for a 40-year period (from October 1969 to September 2009). Their results showed no clear rainfall trends for this Province of Iran. Alijani et al. [26] analyzed daily rainfall concentration and intensity over Iran using 90 stations over varying time periods. The results showed that daily precipitation tends to be irregular and intense across much of Iran and that a disproportionately large share of the annual rainfall comes from a small number of high-intensity-to-extreme rainfall events. Using meteorological data from the Urmia synoptic station, Delju et al. [36] analyzed climate variability and change in the Urmia Lake Basin in the northwest of Iran. They found that mean precipitation has decreased by 9.2% during 1964–2005.

3. “APHRODITE” Dataset

The Asian Precipitation–Highly Resolved Observational Data Integration towards the Evaluation of Water Resources (APHRODITE) dataset is a long-term daily gridded precipitation dataset for Asia, which is based on a dense network of rain gauges. The spatial resolution of this dataset is 0.5° latitude by 0.5° longitude. The data used in the construction of this gridded dataset are from three sources which include GTS-based data (the global summary of the day), data precompiled by other projects or organizations, and APHRODITE's own collection [37]. In this paper the version APHRO_V1101 of APHRODITE was used. In case of Iran station level rain gauge data were provided by the Iran Meteorological Organization. Several quality control measures were conducted on the raw dataset, such as checking for conversion between units of millimeters and inches, discrepancies between two or more databases containing the same measurements, and comparing locations with national boundaries and elevation. Next, the station level data were interpolated using a modified version of the Shepard [38] algorithm, which takes into consideration local elevation differences and horizontal distances. The interpolation technique used in APHRODITE products takes into consideration the ratio of daily precipitation to daily climatology. Further detailed information about the interpolation techniques and additional detailed information about the creation of the APHRODITE dataset are available from Yatagai et al. [37, 39, 40]. This dataset has been successfully used to study different aspects of precipitation patterns in Iran by [30, 41]. It is important to note that the APHRODITE dataset is limited in its estimation of precipitation for high altitude regions in Asia [42–44]. However, the assessment of this dataset for estimation of precipitation patterns across Iran indicates higher levels of accuracy and efficiency [45]. More specifically, a recent study by Ghajarnia et al. [46], consisting of a comparative evaluation of various gridded datasets over Urmia Basin, Iran, revealed that the APHRODITE dataset was able to detect 75% of the rainfall events, and 39% of its rainfall estimations were no rain observations.

4. Station Precipitation Data

Daily rainfall data from 42 stations operated by the Meteorological Organization of Iran were used to evaluate extreme rainfall trend throughout the country (Figure 2). These stations were selected because they have the longest daily rainfall records and are fairly evenly spread throughout the country. Quality controls are applied to the data by the meteorological organization before releasing them to the user's community. There are many weather stations in Iran, but we limited our study to only 42 stations that had data for the period from 1970 to 2009. 18 stations were used in this study with no missing data whatsoever. Another 11 stations had less than 1% of the daily data missing; however, 5 stations had less than 10% of the daily data missing. Eight stations had more than 10% of the data missing. We used several methods to address the missing data issue including substituting the missing value with the climatological average for that day and/or simply

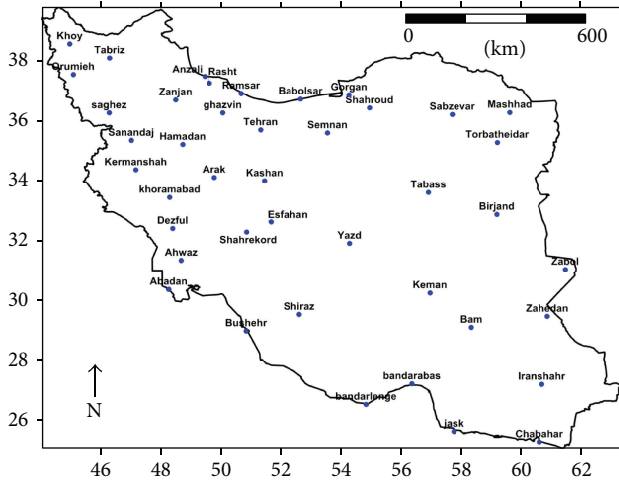


FIGURE 2: Location of 42 meteorological stations in Iran used in this study.

eliminating stations with more than 10% missing values. Our decisions did not appear to influence the final results in any meaningful way.

5. Analyses and Results

As seen in Figure 3, 618 of the $0.5^\circ \times 0.5^\circ$ grid points in the APHRODITE dataset fall within the political boundary of Iran. Therefore, our initial matrix of daily precipitation consisted of 20818 rows, one for each day from January 1, 1951, to December 31, 2007, and 618 columns, one for each grid point in Iran. The average monthly precipitation for the entire area is shown in Figure 4. We analyzed seven different popular indices (for a similar analysis, see [22]) of extreme precipitation for each grid point and year including the following:

- (1) Annual precipitation total (AnnP).
- (2) Number of days with precipitation ≥ 10 mm (ND10mm).
- (3) Percent of annual precipitation from daily events ≥ 10 mm (%Ann10mm).
- (4) Number of days with precipitation ≥ 20 mm (ND20mm).
- (5) Number of days with precipitation \geq the 90th percentile of the distribution (ND90%).
- (6) Maximum precipitation received over five consecutive days (Max5day).
- (7) Maximum one-day precipitation (Max1day).

The calculation of these indices by year and grid point resulted in a new matrix for each index of 57 rows, one for each year from 1951 to 2007, and 618 columns, one for each grid point. In order to compute a countrywide time series for each of the seven indices, the time series at each grid cell was converted to z -scores (mean of 0, standard deviation of 1), and the z -scores were then averaged across the 618 points.

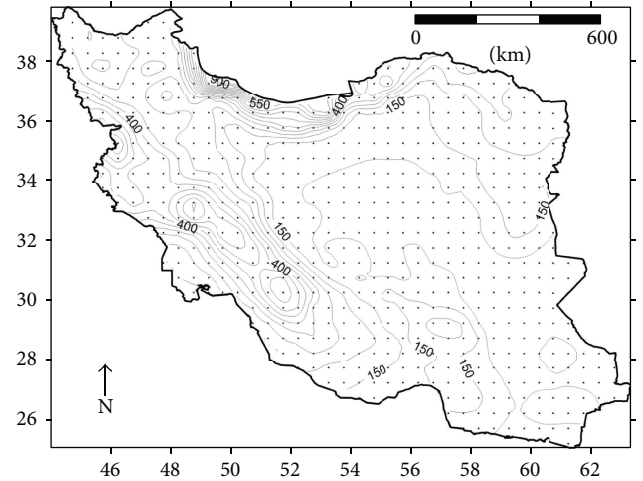


FIGURE 3: Mean annual precipitation (mm) in Iran, 1951–2007, based on 618 grid points throughout the country.

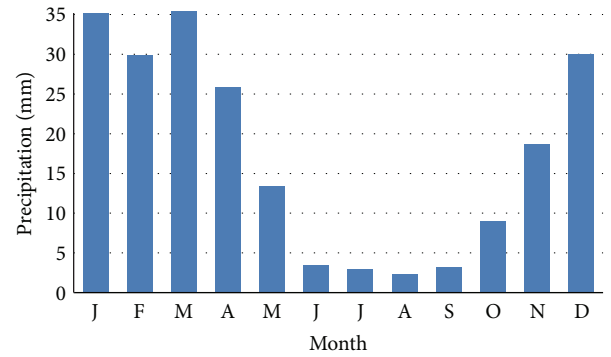


FIGURE 4: Average monthly precipitation (mm) for 618 grid points in Iran, 1951–2007.

This resulted in a final matrix of 57 rows, one for each year, and seven columns, one for each extreme precipitation index. We conducted all analyses with and without an adjustment for leap years and found no meaningful changes in our results.

Recognizing that various statistical techniques used in this study assume normality (a Gaussian distribution) in these time series, we calculated the standardized coefficients of skewness, z_1 , and kurtosis, z_2 , calculated as

$$z_1 = \frac{\left[\sum_{i=1}^N (x_i - \bar{X})^3 / N \right] \left[\sum_{i=1}^N (x_i - \bar{X})^2 / N \right]^{-3/2}}{(6/N)^{1/2}}, \quad (1)$$

$$z_2 = \frac{\left\{ \left[\sum_{i=1}^N (x_i - \bar{X})^4 / N \right] \left[\sum_{i=1}^N (x_i - \bar{X})^2 / N \right]^{-2} \right\} - 3}{(24/N)^{1/2}}, \quad (2)$$

where the resulting z values are compared against a t -value deemed appropriate for a selected level of confidence (e.g., for $N = 57$, $t = 2.66$ for the 0.99 level of confidence). If the absolute value of z_1 or z_2 exceeds the selected value

TABLE 1: Normality test results.

Index	z_1	z_2	K-S
AnnP	0.707	-1.196	0.082
ND10mm	0.865	-1.439	0.096
%Ann10mm	2.510	0.338	0.132
ND20mm	2.827	0.118	0.180
ND90%	0.583	-1.191	0.087
Max5day	1.234	-0.750	0.086
High1day	2.015	-0.186	0.115
Component 1	0.081	-1.126	0.075

z_1 and z_2 are standardized indices of skewness and kurtosis; K-S is the Kolmogorov-Smirnov test statistic.

of t , a significant deviation from the normal curve is confirmed. Otherwise, no statistically significant deviation from a normal distribution is determined (the null hypothesis that the samples came from a normal distribution cannot be rejected). We also used the Kolmogorov-Smirnov one-sample test in which the variable is tested against another variable defined as having a normal distribution. It is similar to a t -test determining whether two variables were drawn from different populations. If the Kolmogorov-Smirnov test is statistically significant, we rejected the hypothesis that the observed data follow the normal distribution.

As seen in Table 1, the only time series with a significant deviation from the normal distribution was the ND20mm index as judged by the Kolmogorov-Smirnov and skewness tests. The deviation was not severe and it could be corrected using a square root transformation in which the sign is maintained and the square root is taken of the absolute value of the z -score. All analyses were conducted with and without this transformation and no meaningful differences were observed.

Given the general lack of deviations from normality, we calculated the Pearson product-moment correlation coefficients among the seven time series (Table 2). All intercorrelation coefficients were significant at the <0.01 level of confidence and many of the correlation coefficients were above $+0.90$. Given the high correlation among the different indices, a principal components analysis (PCA) was conducted to explain the predominant trends in all seven indices analyzed in the present study. The results of PCA to the matrix of seven indices revealed one component explaining 80.9% of the variance in the matrix. The loadings (Table 3) were all positive and ranged from $+0.77$ for AnnP to $+0.99$ for ND10mm. The strength of this one component suggests that it does adequately capture a robust dimension in the precipitation data related to all of the measures of extreme precipitation.

There was no significant deviation from normality in the component scores (Table 1) and as seen in Figure 5, the scores show a distinctive upward trend. Using the year of record as the predictor variable, a simple regression shows that the trend is upward and highly statistically significant ($p < 0.01$) for component 1 and for five of the seven indices; AnnP and ND90% had upward trends that were not significant at the 0.01 level of confidence.

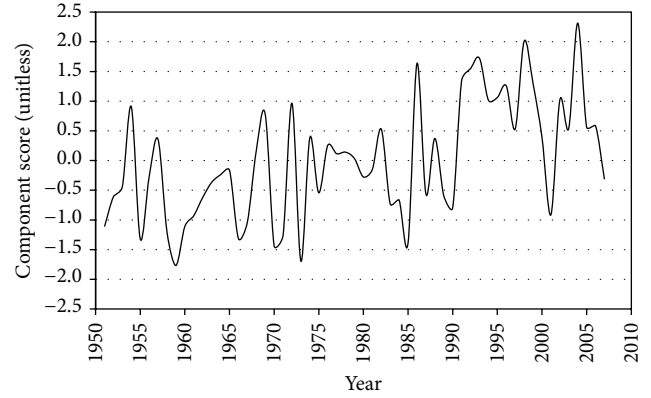


FIGURE 5: Yearly scores for single component explaining 80.9% of the variance in seven indices of extreme precipitation. Year component scores (standardized, mean of 0 and standard deviation of 1) for the single component explaining 80.9% of the variance in seven indices of extreme precipitation. The upward trend suggests that extreme precipitation events, irrespective of how they are defined, are increasing in Iran.

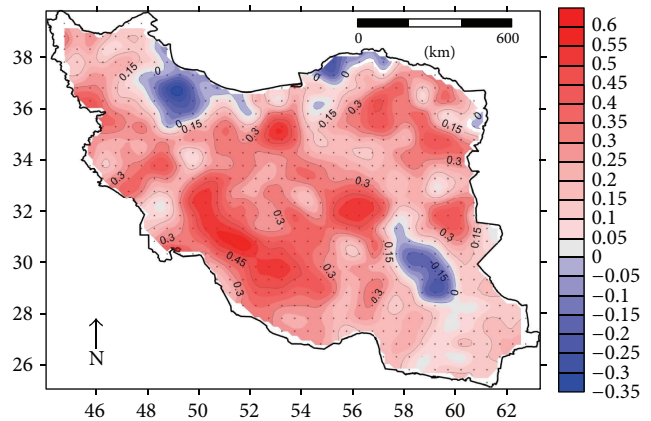


FIGURE 6: Pearson product-moment correlation coefficients for the relationship between “year” and the number of days with precipitation ≥ 10 mm.

As a final procedure with the APHRODITE dataset, we calculated the linear regression between ND10mm and year of record at each of the 618 grid points and plotted the r values (Figure 6). A strong northeast-to-southwest gradient appeared; a simple first-order polynomial interpolation (basically a plane) explained 83% of the spatial variance in the data. The lower values were generally concentrated in the northern border of the study area. The more sophisticated universal kriging method, which is useful for estimating local trend, was used to produce the pattern shown in Figure 6 [47]. It explained 95% of the spatial variance in the correlation coefficient values. Spatial variance explained by an interpolated surface is determined as $1 - (\text{RMSE}^2/\text{SD}^2)$, where RMSE is the root mean square error of the interpolation and SD is the standard deviation of the variable being mapped. We repeated the trend analysis using the Mann-Kendall Rank Statistic which also determines the strength, sign, and significance of

TABLE 2: Pearson product-moment correlation coefficients amount the indices of extreme precipitation.

Index	AnnP	ND10mm	%Ann10mm	ND20mm	ND90%	Max5day	High1day
AnnP	1.00	0.78	0.39	0.53	0.99	0.66	0.57
ND10 mm		1.00	0.87	0.92	0.81	0.92	0.93
%Ann10mm			1.00	0.95	0.45	0.85	0.96
ND20mm				1.00	0.56	0.89	0.97
ND90%					1.00	0.69	0.60
Max5day						1.00	0.90
High1day							1.00

TABLE 3: Principal component loadings and trend results for extreme precipitation indices.

Index	Loading	B	r
AnnP	0.765	1.41	0.19
ND10mm	0.991	4.76	0.54
%Ann10mm	0.885	6.06	0.63
ND20mm	0.936	5.81	0.62
ND90%	0.796	1.87	0.24
Max5day	0.944	4.20	0.49
High1day	0.952	6.16	0.64
Component 1		4.82	0.54

B values are the standardized regression coefficients (beta weights) and r values are the Pearson product-moment coefficients between the variable and year of record.

trend in the ND10mm variable. As seen in Figure 7, positive and significant trends dominated the central-western and northeastern portions of the country, and in no case was a significant downward trend identified, which is similar to the results found by Raziei et al. [34] and Rahimzadeh et al. [27]. The negative trends were mainly concentrated near the Caspian Sea region in the north and in the south central region, which was similar to the results of Raziei et al. [34]. Previously, Modarres and Sarhadi [29] used a set of 145 rainfall stations in Iran to detect trends in 24 hr maximum rainfall. Consistent with our findings, they reported positive trends in 24 hr maximum rainfall at many of the stations. The increasing trend in heavy rainfall may accelerate soil erosion through flash floods resulting in soil loss in particularly sensitive regions.

We repeated all analyses described above using the daily precipitation data from the 42 stations. We again generated the seven indices for each station and used the z -score approach to generate an Iranian-wide time series for each index. Whereas the one principal component explained 80.9% of the variance in the seven indices based on the APHRODITE data, one component explained 82.0% of the variance in the seven indices based on the station data. A time series of the component scores had a Pearson product-moment correlation coefficient of 0.69 with the component scores from the APHRODITE analyses. We repeated these analyses based on 34 stations with less than 10% missing data and found no meaningful differences in the results; the new principal component time series shared a correlation

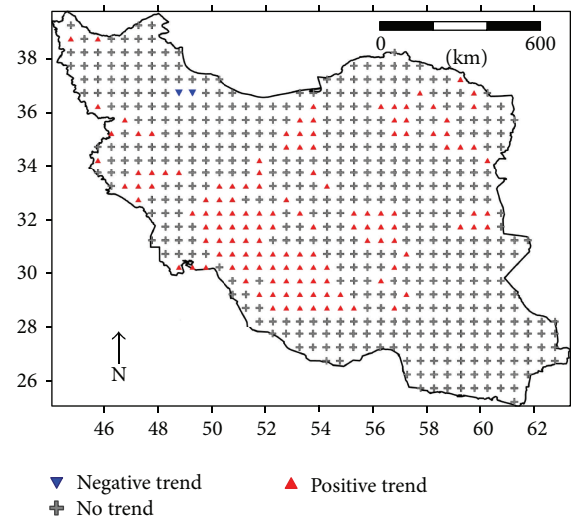


FIGURE 7: Results from Mann-Kendall Rank Statistic showing the significance of trends ($p = 0.01$) in the number of days with precipitation ≥ 10 mm.

of 0.97 with the time series generated based on all stations. The variations in the trends in the spatial patterns of extreme weather events are mainly driven by orography in the form of the mountains in the northern and western interiors [34].

6. Conclusions

We analyzed gridded daily precipitation data from APHRODITE across Iran over the period 1951–2007 and found a strong positive trend in extreme precipitation events. The upward trend appeared in seven different indices and was especially strong in a composite variable of extreme precipitation developed through a principal components analysis. On a regional basis, the trend upward in extreme precipitation was highest in the southwest and least in the northern portions of the country. We found very similar results when we conducted the same analyses based on daily precipitation data from 42 stations across Iran. Our results suggest that the APHRODITE gridded daily precipitation data can appear to be relevant for applications such as trend analysis of extreme events.

Raziei et al. [34] found that precipitation tends to decrease during the warm seasons (spring and summer) and increase

during cold seasons (autumn and winter) in most of Iran. This would imply less precipitation occurrences during the warm season and an intensification of the seasonality and dryness over the country. Iran usually receives the largest proportion of its rainfall during cold seasons. The findings of the present study indicate a significant upward trend has occurred in extreme indices in southwest of Iran (meaning that the portion of extreme occurrences that contributed to the annual rainfall has increased significantly) along the Zagros Mountains where the most important and the biggest rivers of this region originate (e.g., Karoon River, Dez River). Other parts of the country including the southeast and northwest regions showed no trend over our study period. Increases in both intensification of the seasonality and dryness over Iran, along with the increase in extreme indices of rainfall, would be very hazardous for water availability in an arid region like Iran, which receives only 250 mm annually. Consistent with our findings, Alijani et al. [26] indicated that days with rain totals above the 90th percentile account for a disproportionate percentage of the nation's total rainfall, and even very rainy areas are at risk of extreme rainfall and associated hazards. Our results, along with the findings of many other studies, suggest that water access will continue to be a challenge in Iran moving forward.

Conflict of Interests

The authors declare that there is no conflict of interests regarding the publication of this paper.

References

- [1] S. I. Seneviratne, N. Nicholls, D. Easterling et al., "Changes in climate extremes and their impacts on the natural physical environment," in *Managing the Risks of Extreme Events and Disasters to Advance Climate Change Adaptation. A Special Report of Working Groups I and II of the Intergovernmental Panel on Climate Change (IPCC)*, C. B. Field, V. Barros, T. F. Stocker et al., Eds., pp. 109–230, Cambridge University Press, Cambridge, UK, 2012.
- [2] IPCC, "Summary for policymakers," in *Climate Change 2013: The Physical Science Basis. Contribution of Working Group I to the Fifth Assessment Report of the Intergovernmental Panel on Climate Change*, T. F. Stocker, D. Qin, G.-K. Plattner et al., Eds., pp. 3–29, Cambridge University Press, Cambridge, UK, 2013.
- [3] L. V. Alexander, X. Zhang, T. C. Peterson et al., "Global observed changes in daily climate extremes of temperature and precipitation," *Journal of Geophysical Research: Atmospheres*, vol. 111, no. 5, Article ID D05109, 2006.
- [4] N. L. Bindoff, P. A. Stott, K. M. Achuta Rao et al., "Detection and attribution of climate change: from global to regional," in *Climate Change 2013: The Physical Science Basis. Contribution of Working Group I to the Fifth Assessment Report of the Intergovernmental Panel on Climate Change*, T. F. Stocker, D. Qin, G.-K. Plattner et al., Eds., pp. 867–952, Cambridge University Press, Cambridge, UK, 2013.
- [5] K. E. Trenberth, P. D. Jones, P. Ambenje et al., "Observations: surface and atmospheric climate change," in *Climate Change 2007: The Physical Science Basis. Contribution of Working Group I to the Fourth Assessment Report of the Intergovernmental Panel on Climate Change*, S. Solomon, D. Qin, M. Manning et al., Eds., Cambridge University Press, Cambridge, UK, 2007.
- [6] A. Dai, "Recent climatology, variability, and trends in global surface humidity," *Journal of Climate*, vol. 19, no. 15, pp. 3589–3606, 2006.
- [7] K. M. Willett, P. D. Jones, N. P. Gillett, and P. W. Thorne, "Recent changes in surface humidity: development of the HadCRUH dataset," *Journal of Climate*, vol. 21, no. 20, pp. 5364–5383, 2008.
- [8] V. V. Kharin, F. W. Zwiers, X. Zhang, and G. C. Hegerl, "Changes in temperature and precipitation extremes in the IPCC ensemble of global coupled model simulations," *Journal of Climate*, vol. 20, no. 8, pp. 1419–1444, 2007.
- [9] V. V. Kharin, F. W. Zwiers, X. Zhang, and M. Wehner, "Changes in temperature and precipitation extremes in the CMIP5 ensemble," *Climatic Change*, vol. 119, no. 2, pp. 345–357, 2013.
- [10] L. V. Alexander, P. Uotila, and N. Nicholls, "Influence of sea surface temperature variability on global temperature and precipitation extremes," *Journal of Geophysical Research: Atmospheres*, vol. 114, no. 18, Article ID D18116, 2009.
- [11] J. Kenyon and G. C. Hegerl, "Influence of modes of climate variability on global temperature extremes," *Journal of Climate*, vol. 21, pp. 3872–3889, 2010.
- [12] D. L. Hartmann, A. M. G. Klein Tank, M. Rusticucci et al., "Observations: atmosphere and surface," in *Climate Change 2013: The Physical Science Basis. Contribution of Working Group I to the Fifth Assessment Report of the Intergovernmental Panel on Climate Change*, T. F. Stocker, D. Qin, G.-K. Plattner et al., Eds., pp. 160–254, Cambridge University Press, Cambridge, UK, 2013.
- [13] S. C. Pryor, J. A. Howe, and K. E. Kunkel, "How spatially coherent and statistically robust are temporal changes in extreme precipitation in the contiguous USA?" *International Journal of Climatology*, vol. 29, no. 1, pp. 31–45, 2009.
- [14] M. G. Donat, L. V. Alexander, H. Yang et al., "Updated analyses of temperature and precipitation extreme indices since the beginning of the twentieth century: the HadEX2 dataset," *Journal of Geophysical Research*, vol. 118, no. 5, pp. 2098–2118, 2013.
- [15] G. Villarini and G. A. Vecchi, "Twenty-first-century projections of North Atlantic tropical storms from CMIP5 models," *Nature Climate Change*, vol. 2, no. 8, pp. 604–607, 2012.
- [16] M. M. Skansi, M. Brunet, J. Sigró et al., "Warming and wetting signals emerging from analysis of changes in climate extreme indices over South America," *Global Planetary Change*, vol. 100, pp. 295–307, 2013.
- [17] V. Pavan, R. Tomozeiu, C. Cacciamani, and M. di Lorenzo, "Daily precipitation observations over Emilia-Romagna: mean values and extremes," *International Journal of Climatology*, vol. 28, no. 15, pp. 2065–2079, 2008.
- [18] E. Lupikasza, "Spatial and temporal variability of extreme precipitation in Poland in the period 1951–2006," *International Journal of Climatology*, vol. 30, no. 7, pp. 991–1007, 2010.
- [19] A. Toretì, E. Xoplaki, D. Maraun, F. G. Kuglitsch, H. Wanner, and J. Luterbacher, "Characterisation of extreme winter precipitation in mediterranean coastal sites and associated anomalous atmospheric circulation patterns," *Natural Hazards and Earth System Science*, vol. 10, no. 5, pp. 1037–1050, 2010.
- [20] B. N. Goswami, V. Venugopal, D. Sangupta, M. S. Madhusoodanan, and P. K. Xavier, "Increasing trend of extreme rain events over India in a warming environment," *Science*, vol. 314, no. 5804, pp. 1442–1445, 2006.

- [21] N. Plummer, M. J. Salinger, N. Nicholls et al., "Changes in climate extremes over the Australian region and New Zealand during the twentieth century," *Climatic Change*, vol. 42, no. 1, pp. 183–202, 1999.
- [22] S. S. Roy and R. C. Balling Jr., "Trends in extreme daily precipitation indices in India," *International Journal of Climatology*, vol. 24, no. 4, pp. 457–466, 2004.
- [23] S. S. Roy, "A spatial analysis of extreme hourly precipitation patterns in India," *International Journal of Climatology*, vol. 29, no. 3, pp. 345–355, 2009.
- [24] Y. Wang and L. Zhou, "Observed trends in extreme precipitation events in China during 1961–2001 and the associated changes in large-scale circulation," *Geophysical Research Letters*, vol. 32, no. 17, Article ID L09707, pp. 1–4, 2005.
- [25] S. Sen Roy and M. Rouault, "Spatial patterns of seasonal scale extreme hourly precipitation in South Africa," *Applied Geography*, vol. 39, pp. 151–157, 2013.
- [26] B. Alijani, J. O'Brien, and B. Yarnal, "Spatial analysis of precipitation intensity and concentration in Iran," *Theoretical and Applied Climatology*, vol. 94, no. 1–2, pp. 107–124, 2008.
- [27] F. Rahimzadeh, A. Asgari, and E. Fattahi, "Variability of extreme temperature and precipitation in Iran during recent decades," *International Journal of Climatology*, vol. 29, no. 3, pp. 329–343, 2009.
- [28] S. Javanmard, A. Yatagai, M. I. Nodzu, J. Bodagh Jamali, and H. Kawamoto, "Comparing high-resolution gridded precipitation data with satellite rainfall estimates of TRMM_3B42 over Iran," in *Advances in Geosciences*, vol. 25, pp. 119–125, 2010.
- [29] R. Modarres and A. Sarhadi, "Rainfall trends analysis of Iran in the last half of the twentieth century," *Journal of Geophysical Research: Atmospheres*, vol. 114, no. 3, Article ID D03101, 2009.
- [30] T. Raziie, A. Mofidi, J. A. Santos, and I. Bordi, "Spatial patterns and regimes of daily precipitation in Iran in relation to large-scale atmospheric circulation," *International Journal of Climatology*, vol. 32, no. 8, pp. 1226–1237, 2012.
- [31] H. Tabari and P. H. Talae, "Temporal variability of precipitation over Iran: 1966–2005," *Journal of Hydrology*, vol. 396, no. 3–4, pp. 313–320, 2011.
- [32] S. Soltani, R. Saboohi, and L. Yaghmaei, "Rainfall and rainy days trend in Iran," *Climatic Change*, vol. 110, no. 1–2, pp. 187–213, 2012.
- [33] B. S. Somé, A. Ezani, and H. Tabari, "Spatiotemporal trends and change point of precipitation in Iran," *Atmospheric Research*, vol. 113, pp. 1–12, 2012.
- [34] T. Raziie, J. Daryabari, I. Bordi, and L. S. Pereira, "Spatial patterns and temporal trends of precipitation in Iran," *Theoretical and Applied Climatology*, vol. 115, no. 3–4, pp. 531–540, 2014.
- [35] P. H. Talae, "Iranian rainfall series analysis by means of nonparametric tests," *Theoretical and Applied Climatology*, vol. 116, no. 3–4, pp. 597–607, 2014.
- [36] A. H. Delju, A. Ceylan, E. Piguet, and M. Rebetez, "Observed climate variability and change in Urmia Lake Basin, Iran," *Theoretical and Applied Climatology*, vol. 111, no. 1–2, pp. 285–296, 2013.
- [37] A. Yatagai, K. Kamiguchi, O. Arakawa, A. Hamada, N. Yasutomi, and A. Kitoh, "APHRODITE: constructing a long-term daily gridded precipitation dataset for Asia based on a dense network of rain gauges," *Bulletin of the American Meteorological Society*, vol. 93, no. 9, pp. 1401–1415, 2012.
- [38] D. Shepard, "A two-dimensional interpolation function for irregularly-spaced data," in *Proceedings of the 23rd ACM National Conference (ACM '68)*, pp. 517–524, Brandon/Systems Press, Las Vegas, Nev, USA, August 1968.
- [39] A. Yatagai, P. Xie, and P. Alpert, "Development of a daily gridded precipitation data set for the Middle East," *Advances in Geosciences*, vol. 12, pp. 165–170, 2008.
- [40] A. Yatagai, O. Arakawa, K. Kamiguchi, H. Kawamoto, M. I. Nodzu, and A. Hamada, "A 44-year daily gridded precipitation dataset for Asia based on a dense network of rain gauges," *Scientific Online Letters on the Atmosphere*, vol. 5, no. 1, pp. 137–140, 2009.
- [41] T. Raziie, I. Bordi, J. A. Santos, and A. Mofidi, "Atmospheric circulation types and winter daily precipitation in Iran," *International Journal of Climatology*, vol. 33, no. 9, pp. 2232–2246, 2013.
- [42] C. Andermann, S. Bonnet, and R. Gloaguen, "Evaluation of precipitation data sets along the Himalayan front," *Geochemistry, Geophysics, Geosystems*, vol. 12, no. 7, Article ID Q07023, 2011.
- [43] A. M. El Kenawy and M. F. McCabe, "A multi-decadal assessment of the performance of gauge- and model-based rainfall products over Saudi Arabia: climatology, anomalies and trends," *International Journal of Climatology*, 2015.
- [44] H. Yin, M. G. Donat, L. V. Alexander, and Y. Sun, "Multi-dataset comparison of gridded observed temperature and precipitation extremes over China," *International Journal of Climatology*, vol. 35, no. 10, pp. 2809–2827, 2015.
- [45] E. Nasrabadi, S. A. Masoodian, and H. Asakereh, "Comparison of gridded precipitation time series data in APHRODITE and Asfazi databases within Iran's territory," *Atmospheric and Climate Sciences*, vol. 3, no. 2, pp. 235–248, 2013.
- [46] N. Ghajarnia, A. Liaghat, and P. Daneshkar Arasteh, "Comparison and evaluation of high resolution precipitation estimation products in Urmia Basin-Iran," *Atmospheric Research*, vol. 158–159, pp. 50–65, 2015.
- [47] Spatial-analysis.net, *Universal Kriging*, 2015, http://spatial-analyst.net/ILWIS/htm/ilwisapp/universal_kriging_functionality.htm.

Research Article

Spatial Combination Modeling Framework of Saturation-Excess and Infiltration-Excess Runoff for Semihumid Watersheds

Pengnian Huang,^{1,2} Zhijia Li,^{1,2} Cheng Yao,^{1,2} Qiaoling Li,^{1,2} and Meichun Yan³

¹College of Hydrology and Water Resources, Hohai University, Nanjing 210098, China

²National Cooperative Innovation Center for Water Safety & Hydro-Science, Hohai University, Nanjing 210098, China

³School of Earth Science and Engineering, Hohai University, Nanjing 210098, China

Correspondence should be addressed to Cheng Yao; yaocheng@hhu.edu.cn

Received 5 October 2015; Revised 22 December 2015; Accepted 30 December 2015

Academic Editor: Jingfeng Wang

Copyright © 2016 Pengnian Huang et al. This is an open access article distributed under the Creative Commons Attribution License, which permits unrestricted use, distribution, and reproduction in any medium, provided the original work is properly cited.

There exist two types of direct runoff generation mechanisms in semihumid watersheds: saturation-excess mechanism and infiltration-excess mechanism. It has always been a difficult problem for event hydrological simulation to distinguish the two types of runoff processes. Based on the concept of dominant runoff processes, combined with GIS and RS techniques, this paper proposed an event-based spatial combination modeling framework and built two spatial combination models (SCMs) accordingly. The CN parameter and topographic index, both of which are widely used in hydrological researches, are adopted by the SCM to divide the entire watershed into infiltration-excess dominated (IED) areas and saturation-excess dominated (SED) areas. Dongwan watershed was taken as an example to test the performances of infiltration-excess model, saturation-excess model, and SCM, respectively. The results of parameter optimization showed that the parameter values and state variables of SCM are much more realistic than those of infiltration-excess model and saturation-excess model. The more accurate the divisions of infiltration-excess and saturation-excess dominated areas, the more realistic the SCM parameter values. The simulation results showed that the performance of SCM was improved in both calibration and validation periods. The framework is useful for flood forecasting in semihumid watersheds.

1. Introduction

Floods are one of the most common natural hazards throughout the world. Therefore, as a crucial flood protection tool, flood simulation model has received increasing attention. In order to increase the model's predictive power, model realism is always considered as an important topic in the model development process [1–4]. As early as 1970, Nash and Sutcliffe stated that if it was hoped to use the model for watersheds without records, it was essential to obtain some guide to the realism of model parts and the accuracy of parameter values [5].

The physically based hydrological model is a powerful tool to reflect the physical reality of watershed hydrological response. However, it needs highly detailed and abundant data (e.g., high-resolution land use data, soil data, and groundwater data) to represent the hydrophysical processes. Such data are usually unavailable or difficult to obtain. In

addition, due to the use of bottom-up approach, the physically based hydrological model is more applicable for small watersheds, which cannot meet the requirements of flood forecasting.

The conceptual hydrological model is more suitable for flood forecasting. The difficulty is that how to increase the realism and the predictive power of a conceptual model. The flexible model framework proposed recently is a useful way to configure a realistic conceptual model structure for a given watershed [6–8].

Traditionally, conceptual model cannot represent the heterogeneity and complexity of hydrological processes within a watershed. To solve this problem, Savenije proposed the spatially distributed conceptual structure using the flexible approach [9]. He believed that, among landscape factors, terrain factor is the most critical factor affecting runoff generation and routing, followed by vegetation factor and soil factor. He took a typical western European watershed as

an example to elaborate his methodology. The watershed was divided into three parts: wetlands, hillslopes, and plateaus. Wetlands close to the rivers are dominated by saturation-excess runoff, hillslopes which are usually forested are dominated by lateral runoff, and plateaus are dominated by deep percolation, sometimes accompanied by infiltration-excess runoff. Gao et al. applied this methodology to the watershed of the upper Heihe River in China and found that the hillslope should be further subdivided into grassland and woodland [4]. For more researches, the reader is referred to [10–12].

Such frameworks are suitable for continuous simulation rather than event simulation. In the continuous simulation, evapotranspiration, and subsurface flow are important components, whereas in the event simulation, they can be ignored to some extent. Therefore, frameworks for continuous and event hydrological simulation should largely differ.

This study aims to develop a spatially distributed conceptual structure for flood event simulation. As is generally known, at the point scale, runoff generation can be represented exactly by differential equations [13]. However, at the watershed scale for flood simulation, the differential equations should be simplified into two runoff generation mechanisms: saturation-excess mechanism [14] and infiltration-excess mechanism [15]. Saturation-excess runoff is dominant in humid areas and infiltration-excess runoff is dominant in arid and semiarid areas [16–19]. Nevertheless, in semihumid areas, there is no dominant runoff generation mechanism. In other words, saturation-excess and infiltration-excess runoff may exist simultaneously during a storm, which can be called mixed runoff generation.

Currently, conceptual saturation-excess runoff model is maturely developed and widely used. Flood forecasting using this type of model can meet the accuracy requirements in humid areas in China. On the contrary, great difficulties have hindered accurate forecasts of infiltration-excess runoff in arid and semiarid areas, which are mainly due to the lack of high-resolution observational data. Despite the problem of data shortage, the understanding of the processes of infiltration-excess runoff generation is still clear. However, in semihumid areas, there is no clear understanding of the mixed runoff generation, and the main difficulty is how to identify the saturation-excess and infiltration-excess runoff that coexist within a watershed.

The current popular mixed runoff models are constructed in the light of the vertical combination of saturation-excess module and infiltration-excess module, such as Sacramento model [20]. These mixed runoff models partly avoid the defects of single runoff models and are able to improve the forecast accuracies of flood events. However, their performances overly depend on parameter calibration and optimization. Consequently, the problem of identification of saturation-excess runoff and infiltration-excess runoff is not solved and the model realism is limited.

To some extent, the spatial distribution of infiltration-excess and saturation-excess runoff is regular. For example, Burns et al. found that the runoff from the outcrop, which occupied about one-third of the catchment area, was most likely as infiltration-excess runoff and contributed more than half of the peak streamflow [21]. Buda et al. found

that, in upslope positions without a fragipan, runoff was generated primarily via the infiltration-excess mechanism (96% of events) [22]. As a preliminary study, based on the concept of dominant hydrological processes, we tried to divide the watershed into saturation-excess dominated (SED) areas and infiltration-excess dominated (IED) areas for event simulation and then validate whether this division can increase model realism and improve simulation accuracy.

Based on the landscape factors, a parallel-featured spatial combination modeling framework is proposed for event hydrological simulation in this paper. In this framework, the runoff curve number (simply called CN) [23] is employed to delineate the IED areas, and the topographic index (simply called TI) [24] is employed to delineate the SED areas. The spatial combination model (SCM) is built accordingly, in which the saturation-excess module and infiltration-excess module are used in SED and IED areas, respectively. The total runoff is the sum of infiltration-excess and saturation-excess runoff.

2. Study Area and Data

2.1. Study Area. Dongwan watershed is located in the source area of Yihe River Basin in Henan Province, China (Figure 1). The annual precipitation in Yihe River Basin ranges from 500 mm to 1100 mm and tends to increase as elevation increases. The mountainous areas are rainy and the valleys as well as the adjacent hilly areas are relatively dry. The distribution of precipitation during the year is uneven. The precipitation from July to September accounts for more than 50% of a whole year. The maximum annual precipitation is about 2 times larger than the least.

Dongwan watershed is located between longitude 111°~112°E and latitude 33.5°~34.5°N, covering a drainage area of 2856 km², belonging to a continental monsoon climate. The west of the watershed is high and the east is relatively low. The upstream area is mainly covered by forest. The storm is the major cause of the watershed flood which is characterized by sharp hydrograph, high peak, and short duration and is a great threat to the downstream area.

Dongwan watershed is a semihumid watershed. According to the magnitude of annual precipitation, the shape of flood hydrographs, the extent of vegetation coverage, and other factors, it is apparent that both saturation-excess and infiltration-excess mechanisms play an important role in the processes of direct runoff generation and routing.

2.2. Data. The digital elevation data are obtained from the second version of ASTER GDEM data released by NASA, at a 30 m spatial resolution. The soil data is obtained from the 1:1,000,000 scale vector-based soil map data provided by the Institute of Soil Science, Chinese Academy of Science, which contains the information of sand content (particle diameter > 0.05 mm, according to US Soil Taxonomy), silt content (diameter between 0.05 mm and 0.002 mm), clay content (diameter < 0.002 mm), saturated hydraulic conductivity, and so forth, for 0–20 cm depth and 20–100 cm depth, respectively. The vegetation data are obtained from the landsat 8 imagery data provided by USGS, path/row numbers 125/36.

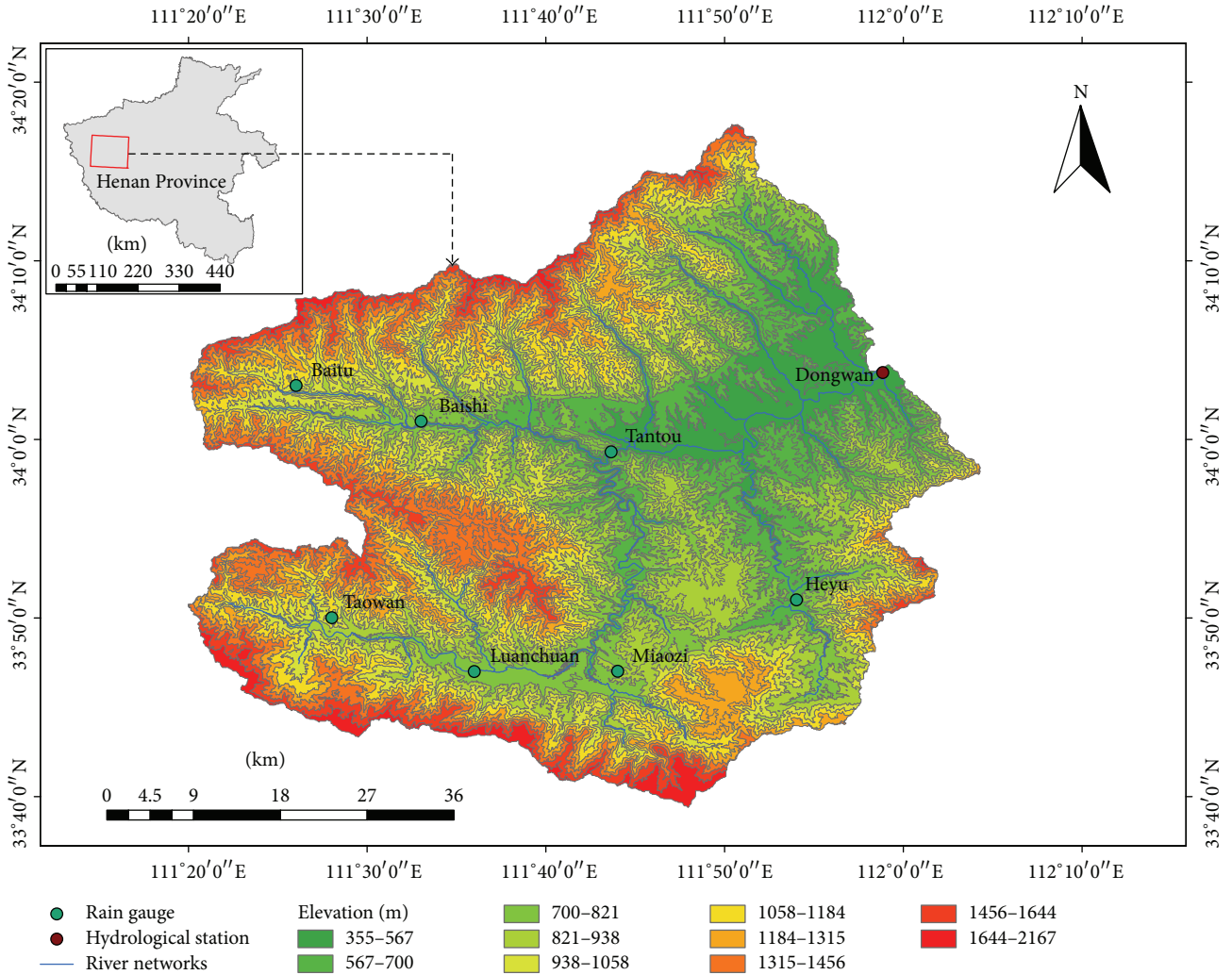


FIGURE 1: Location, topography, and river networks of Dongwan watershed.

Hydrological data include precipitation, streamflow, and pan-evaporation data, provided by the Yellow River Conservancy Commission (YRCC). There are 8 rain-gauge stations in Dongwan watershed and one hydrological station at the outlet of the watershed. Daily hydrological data are available from 1960 to 2011, except for 1969. Subdaily data are only available during flood events in the years of 1961–1968, 1973, 1975, 1977, 1981–1985, 1994–1996, 1998, and 2000–2011. Due to the effects of human activities, the flood characteristics in the post-1980 period are significantly different from those in the pre-1980 period.

The subdaily data were interpolated into hourly data. Only the subdaily data after 1994 were precise and complete enough. The subdaily data in the pre-1994 period were confusing and difficult to collect, especially in the pre-1980 period. As a result, the pre-1980 flood data were not used for calibration or validation. Flood events in the period of 1994 to 2001 were selected for calibration and those in the period of 1981 to 1985 were selected for validation.

Flood events in the calibration period were selected using the annual maximum method; thus, there were 16 flood

events except 1997 and 1999 as no flood records in the two years. In the validation period, in order to choose more flood events, 7 flood events were selected using the method of Peaks over Threshold.

3. Modeling Approach

3.1. Saturation-Excess Model. Xinanjiang (XAJ) model, the most popular conceptual rainfall-runoff model in China, is a powerful tool not only for flood simulation and operational forecasting but also for hydrology research such as flood forecasts in ungauged basins [25] and impacts of rain gauge densities on runoff simulation [26]. The main merit of XAJ model is that it can account for the uneven spatial distribution of soil moisture storage capacity represented by a parabolic curve.

The tension water storage capacity at a point W^t , varying from zero to the watershed maximum value W_{MM}^t , is described by a nonlinear functional relationship (Figure 2),

$$\frac{f}{F} = 1 - \left(1 - \frac{W^t}{W_{MM}^t} \right)^b, \quad (1)$$

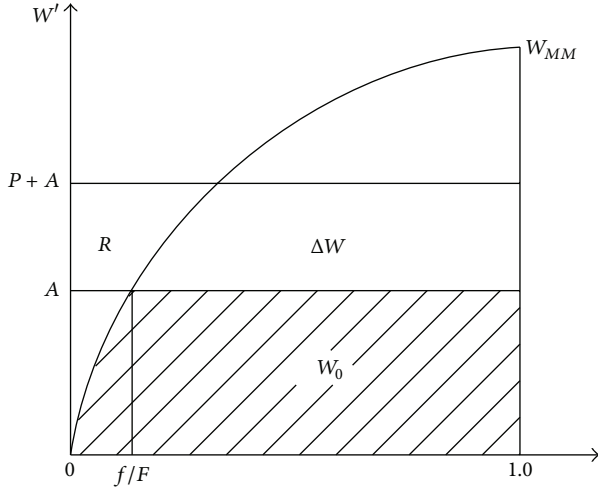


FIGURE 2: The spatial distribution of tension water capacity represented in XAJ model. W' is the tension water capacity at a certain point, W_{MM} is the maximum value of W' within a watershed, f/F is the portion of the watershed area having tension water capacity smaller than W' , A is the value of the vertical axis corresponding to f/F , P is the precipitation, R is the runoff, W_0 is the antecedent soil moisture content prior to an event, and ΔW is the change in the soil moisture content.

where f is the partial pervious area of the watershed whose tension water storage capacity is less than or equal to W' , F is the total pervious area of the watershed, and b is the shape parameter of the parabolic curve.

According to Figure 2, the initial soil moisture content W_0 can be acquired by integral calculation:

$$\begin{aligned} W_0 &= \int_0^A \left(1 - \frac{f}{F}\right) dW' \\ &= \frac{W_{MM}}{b+1} \left[1 - \left(1 - \frac{A}{W_{MM}}\right)^{b+1}\right]. \end{aligned} \quad (2)$$

If $A = W_{MM}$, then $W_0 = W_M$ and $W_M = W_{MM}/(1+b)$.

According to (2), the following equation can be expressed as follows:

$$A = W_{MM} \left[1 - \left(1 - \frac{W_0}{W_M}\right)^{1/(1+b)}\right]. \quad (3)$$

In XAJ model, runoff occurs only at the points where the tension water capacities are filled with precipitation. Hence, the formula of total runoff can be derived:

$$\begin{aligned} R &= \int_A^{P+A} \frac{f}{F} dW' \\ &= \int_A^{P+A} \left[1 - \left(1 - \frac{W'}{W_{MM}}\right)^b\right] dW'. \end{aligned} \quad (4)$$

If $P_E + A < W_{MM}$, then the runoff formula is

$$R = P_E - (W_M - W_0) + W_M \left(1 - \frac{P_E + A}{W_{MM}}\right)^{1+b}. \quad (5)$$

If $P_E + A \geq W_{MM}$, then the runoff formula is

$$R = P_E - (W_M - W_0). \quad (6)$$

The schematic diagram and more details about XAJ model can be found in [27, 28].

3.2. Infiltration-Excess Model

3.2.1. *Infiltration Curve.* The runoff generation module of Hebei model [29], which is locally used in the Hebei Province of China for flood forecasting, is adopted to build the infiltration-excess model using the modified Horton equation,

$$f = f_c + f_0 e^{-um}. \quad (7)$$

In the above equation f is the infiltration capacity, f_c is the steady-state infiltration capacity, f_0 is the initial infiltration capacity, u is an infiltration coefficient, and m is the surface soil moisture content calculated by the following equation:

$$m = F_s + k_{im} P_a, \quad (8)$$

where k_{im} is a coefficient representing the ratio of surface soil thickness to the vadose zone thickness, ranging from 0 to 1, P_a is the antecedent soil moisture content, and F_s is the cumulative infiltration amount during a flood event.

3.2.2. *Spatial Distribution Curve of Infiltration Capacity.* The spatial infiltration capacity distribution curve is analogous to the spatial storage capacity distribution curve applied in XAJ model, which indicates the spatial variation in point infiltration capacity over the watershed. Similar upscaled expression for areal average infiltration capacity can be seen in [30]. Surface runoff is generated at the point where the precipitation rate exceeds the infiltration capacity (Figure 3):

$$\frac{F_A(t)}{F} = 1 - \left(1 - \frac{f'(t)}{f_{mm}}\right)^n. \quad (9)$$

In formula (9) $F_A(t)$ is the partial area of the watershed whose infiltration capacity is less than or equal to $f'(t)$ which is equivalent to the rainfall intensity $i(t)$ in the time interval t , f_{mm} is the maximum point infiltration capacity, F is the total area of the watershed, and n is the shape parameter of the spatial distribution curve.

The initial areal average infiltration capacity $\overline{f_0(t)}$ corresponding to the rainfall intensity $i(t)$ can be calculated as

$$\overline{f_0(t)} = i(t) - \frac{i(t)^{1+n}}{(1+n)f_{mm}^n}, \quad i(t) < f_{mm}, \quad (10)$$

$$\overline{f_0(t)} = f_{mm} - \frac{f_{mm}}{1+n}, \quad i(t) \geq f_{mm}. \quad (11)$$

3.2.3. *Runoff Generation and Routing.* Integrating (7) with (11), the surface infiltration capacity in the time interval t can be calculated as

$$f(t) = \left(i(t) - \frac{i(t)^{1+n}}{(1+n)f_{mm}^n}\right) e^{-um(t)} + f_c. \quad (12)$$

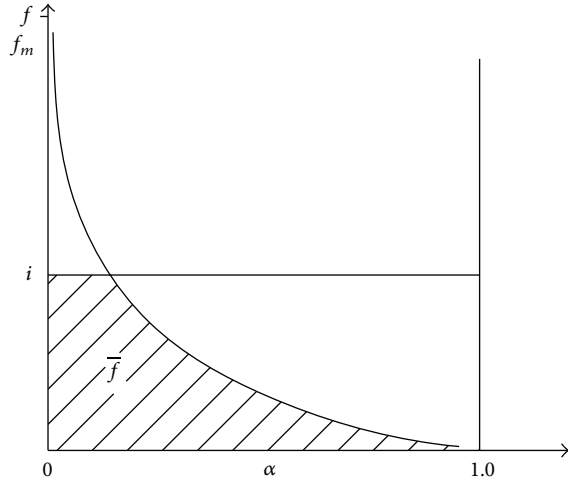


FIGURE 3: The spatial distribution of infiltration capacity represented in infiltration-excess model. f is the infiltration capacity at a certain point, f_{mm} is the maximum value of f within a watershed, α is the portion of the watershed area having the infiltration capacity smaller than f , i is the rainfall intensity, and \bar{f} is the average infiltration rate corresponding to i .

The surface runoff in the time interval t is calculated as

$$R_s(t) = P(t) - F(t), \quad (13)$$

where $P(t)$ is the precipitation amount in the time interval t and $F(t)$ is the infiltration amount in the time interval t .

The calculation of subsurface runoff generation in infiltration-excess model is similar to the runoff generation calculation in XAJ model, using (5) and (6).

The method of runoff routing calculation in infiltration-excess model is the same as that in XAJ model.

3.3. Spatial Combination Modeling Framework

3.3.1. Subwatershed Divisions. Digital elevation data are mainly used to outline the watershed boundary, extract the river network, and divide the watershed into subwatersheds.

Runoff mechanisms are determined by the combined effects of landscape factors and meteorological factors. Meteorological factors are closely related to terrain factors [31, 32]; for example, elevation and aspect factors have a strong impact on rainfall factors.

Landscape factors include terrain factors, vegetation factors, soil factors, and geological factors. The first three factors have a strong control on the surface runoff generation. Although the spatial distribution of landscape factors in a watershed is extremely complex, the distributed modeling needs to consider the spatial heterogeneity of these factors. When the entire watershed is divided into several or more subwatersheds, factors in subwatersheds are relatively simple and single; therefore, it is easier to judge runoff mechanisms in subwatersheds.

In this study, Dongwan watershed is divided into 52 subwatersheds using the ARC Hydro data model, which is developed and maintained by ESRI. The largest subwatershed covers an area of 134 km², while the smallest subwatershed

covers only 10 km². The rainfall data for each subwatershed is obtained from the rain-gauge station which is nearest to the subwatershed centroid.

3.3.2. Topographic Index Calculation. Beven and Kirkby first proposed the concept of topographic index in 1979 and defined it as $\ln(\alpha/\tan\beta)$, where α is the local upslope area draining through a certain point per unit contour length and $\tan\beta$ is the local slope [24]. Beven thought that the water flow was mainly controlled by terrain; thus, topographic index can reflect the long-term soil moisture condition of every point in a watershed. Generally, topographic index is larger in valleys, riversides, and so forth, where the soil is moist and is liable to be saturated during storms. On the contrary, it is relatively smaller in peaks, ridges, and so forth, where the soil is relatively dry and is difficult to be saturated during storms. In hydrological modeling, topographic index is often used as a physically meaningful indicator, which can be used to quantitatively evaluate the effect of terrain factors on saturation-excess runoff generation and estimate the specific locations of saturation-excess overland flow.

In this study, topographic index is calculated by the Tool Chain function in SAGA GIS of version 2.1.4, using the default multiple flow direction algorithm. SAGA GIS is a free and open source GIS software which can be downloaded from <http://sourceforge.net/projects/saga-gis/>. Then the areal average topographic index for each subwatershed can be calculated by the Zonal tool in ArcGIS 10.1 (Figure 4).

3.3.3. CN Estimation. Before estimating the CN value, remote sensing data and soil data should be processed first.

In order to take into account the effect of vegetation on runoff generation, land use information was extracted from Landsat 8 images and was classified into five classes: arable land, forest, building land, water area, and unused land (bare rock and bare soil). Forest area accounts for the largest percent of total watershed area, reaching 82.16%, followed by unused land area, constituting 10.42%. The area of the remaining land use types only accounts for 7.42%.

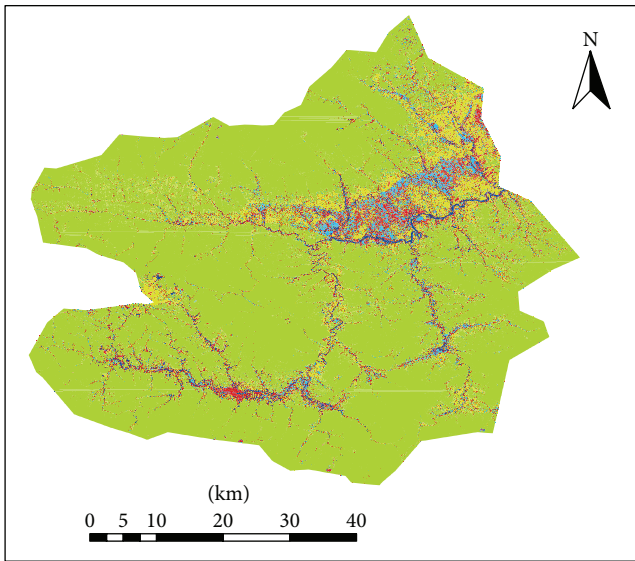
Runoff generation processes are also affected by soil types. The US Natural Resources Conservation Service has ever proposed a soil classification method from the perspective of rainfall-runoff relationship. According to the hydrological properties and runoff potential, soils can be classified into four groups, A, B, C, and D, as shown in Table 1 and Figure 5.

SCS-CN model assumes that “the ratio of actual runoff to the maximum potential runoff is equal to the ratio of the actual infiltration amount to the maximum possible infiltration amount,” which can be employed to calculate the direct runoff generated during a storm. The model is popular in the world as it is simple and easy to use [23].

CN is the only parameter of the model, which is a dimensionless number and can represent the degree of infiltration loss. It can be determined by soil type, land use type, surface morphology, and antecedent soil moisture content without calibration. Since surface morphology can be represented by topographic index, CN is only related to soil type and land use type in this study, determined using Table 2.

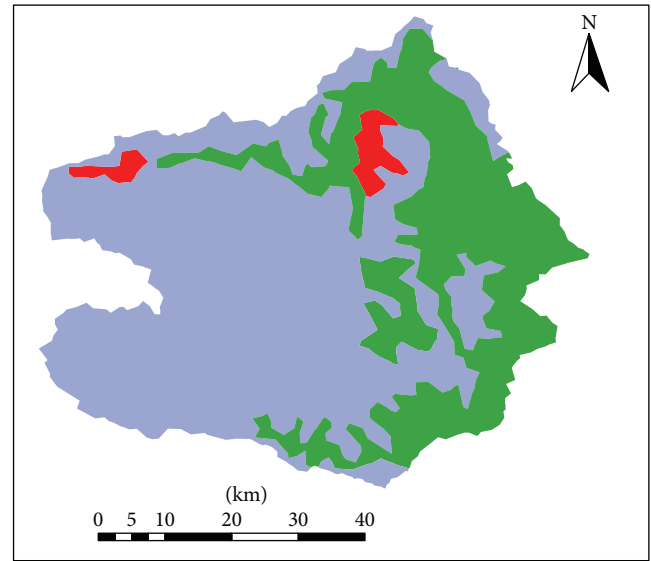
TABLE 1: Hydrological soil groups.

Hydrologic soil group	Saturated hydraulic conductivity mm/h	Runoff generation characteristics	Soil types
A	>110	Soils have low runoff potential and high infiltration rates even when thoroughly wetted	Mainly sand, loamy sand, and sandy loam
B	14~110	Soils have moderate infiltration rates when thoroughly wetted	Mainly silty sand and loam
C	1.4~14	Soils have low infiltration rates when thoroughly wetted	Mainly sandy clay loam
D	<1.4	Soils have high runoff potential and very low infiltration rates even when thoroughly wetted	Mainly clay loam, silty clay loam, sandy clay, silty clay, and clay



Land use
 Arable land (light blue)
 Forest (green)
 Unused land (yellow)
 Water body (dark blue)
 Building land (red)

FIGURE 4: Land use map for Dongwan watershed.



Soil group
 A (green)
 B (light blue)
 D (red)

FIGURE 5: Hydrological soil group map for Dongwan watershed.

TABLE 2: CN values.

Land use type	A	B	C	D
Arable land	67	78	85	89
Forest	25	55	70	77
Water body	100	100	100	100
Building land	51	68	79	84
Unused land	72	82	88	90

Now CN is a static index, reflecting the infiltration capacity of land surface under normal humidity conditions and representing the potential of infiltration-excess runoff. A large CN value shows a small infiltration capacity of land surface, where infiltration-excess runoff is likely to occur. Similarly, a small CN value indicates a large infiltration capacity, where infiltration-excess runoff is unlikely to occur.

The areal CN value for each subwatershed can be obtained by the Zonal tool in ArcGIS 10.1.

3.3.4. Model Construction. Dongwan watershed is divided into SED subwatersheds and IED subwatersheds based on the concept of dominant hydrological processes [33]. The actual runoff processes are extremely complex, and the saturation-excess runoff and infiltration-excess runoff in a watershed are spatially and temporally dynamic. Currently, hydrologists are not able to make a complete simulation of such complex runoff processes and only able to capture the essential runoff features, that is, dominant hydrological processes. For example, in a SED subwatershed which is characterized by lush vegetation, porous soil, and flat terrain, the saturation-excess runoff is likely to occur but not necessarily to occur. Although this subwatershed may be dominated by infiltration-excess runoff during few flood events, it is dominated by saturation-excess runoff during most flood events, especially medium and large flood events.

Compared with complete simulation of runoff processes, simulation of dominant hydrological processes is more important and reliable, because it needs less data and computational power and can avoid some difficult problems such as

overparameterization which are currently hard to deal with. Two methods are used in this paper to divide the study watershed into SED subwatersheds and IED subwatersheds: one is CN division method and the other is CN-TI division method. CN division method sorts the subwatersheds according to their areal CN values using the Natural Break function in ArcGIS 10.1. Subwatersheds with smaller areal CN value are considered as SED subwatersheds, and the other are IED subwatersheds. The model based on this method is named SCM I. CN-TI division method is the improved CN division method. Based on the result of the CN division method, the IED subwatersheds with larger topographic index are changed as SED subwatersheds. The constructed model is named SCM II accordingly.

XAJ model is employed in SED subwatersheds for runoff calculation and infiltration-excess model is implemented in IED subwatersheds.

The linear reservoir method is used to simulate runoff concentration in the river network of each subwatershed and segmented Muskingum formula is used to simulate runoff routing from the subwatershed outlet to the watershed outlet, which is the same as that used in XAJ model.

3.4. Model Calibration and Evaluation. When using the single runoff model (XAJ model and infiltration-excess model), Dongwan watershed was divided into 8 subwatersheds through Thiessen polygon method. When using SCM I and SCM II, the watershed was divided into 52 subwatersheds as mentioned above. To lighten the computational burden and reduce the parameter uncertainty, only sensitive parameters were automatically calibrated by the SCE-UA global optimization algorithm [34, 35]. Because flood runoff mainly includes surface runoff and rapid interflow, the model parameters associated with these runoff components can be identified as sensitive parameters. In saturation-excess module, the identified sensitive parameters are S_M and C_I ; and in infiltration-excess module, they are k_{im} , f_c , u , and f_{mm} . In addition, C_s is also very sensitive, which represent the effect of the river network on runoff processes.

Daily version of XAJ model was used to initialize the event model, calculating the soil moisture condition prior to each flood event. The period of 1994 to 2001 was selected as calibration period and the period of 1981 to 1985 was selected as validation period. The application of XAJ model can be seen in detail in [27, 28].

The performance of the model is evaluated using the following criteria on a relative basis.

The relative error of runoff depth:

$$\Delta R_T (\%) = \frac{R_{CD} - R_{OD}}{R_{OD}} \times 100\%. \quad (14)$$

The relative error of peak flow:

$$\Delta Q_p (\%) = \frac{Q_{CP} - Q_{OP}}{Q_{OP}} \times 100\%, \quad (15)$$

where R_{CD} and Q_{CP} refer to the simulated runoff depth and peak flow, R_{OD} and Q_{OP} refer to the observed runoff depth and peak flow.

Referring to the national criteria for flood forecasting in China, (14) is transformed into a binary function [36, 37],

$$Q_{uv} = \begin{cases} 1, & \Delta R_T \leq 20\%, \\ 0, & \Delta R_T > 20\%, \end{cases} \quad (16)$$

where Q_{uv} indicates whether the runoff depth simulation is qualified. 1 means qualified and 0 means unqualified.

Likewise,

$$Q_{up} = \begin{cases} 1, & \Delta Q_p \leq 20\%, \\ 0, & \Delta Q_p > 20\%, \end{cases} \quad (17)$$

where Q_{up} indicates whether the peak flow simulation is qualified.

Thus, the qualified rates of peak flow simulation R_p and runoff depth simulation R_v can be calculated as follows:

$$R_p = \sum_{i=1}^n \frac{Q_{up,i}}{n}, \quad (18)$$

$$R_v = \sum_{i=1}^n \frac{Q_{uv,i}}{n}, \quad (19)$$

where n is the number of simulated runoff events. In China, the model can be used for operational flood forecasting only when its qualified rate exceeds 70%.

Different objective functions are in favor of different hydrographic components. For hydrological event simulation, the objective function should be in favor of high flows. If the objective function was selected appropriately, the calibrated parameter values are more realistic [38]. In this study, the objective function involves simulation of peak flow and runoff depth, aggregating (18) and (19):

$$CR = \frac{1}{\left(\sum_{i=1}^n Q_{uv,i} + \sum_{i=1}^n Q_{up,i} + 1\right)}. \quad (20)$$

4. Results

4.1. Results of Subwatershed Division. Figure 6(a) shows the result of the CN division method. The IED subwatershed area accounts for about 68% of the total watershed area, most of which are located in the upstream and located on the north of the main river channel in the downstream. In the upstream there are mainly group B soils with medium infiltration capacity; therefore, infiltration-excess runoff tends to occur under high rainfall intensity. In the downstream there are mainly group A soils with high infiltration capacity; however, the north side of the main river channel is predominantly made up of bare soils with low vegetation coverage and consequently classified as IED subwatersheds.

Figure 6(b) shows the result of CN-TI division method, where the IED subwatershed area occupies about 50% of the total area. After considering the terrain factors, the number of IED subwatersheds in the downstream is significantly reduced, only one left. In other words, the IED subwatersheds

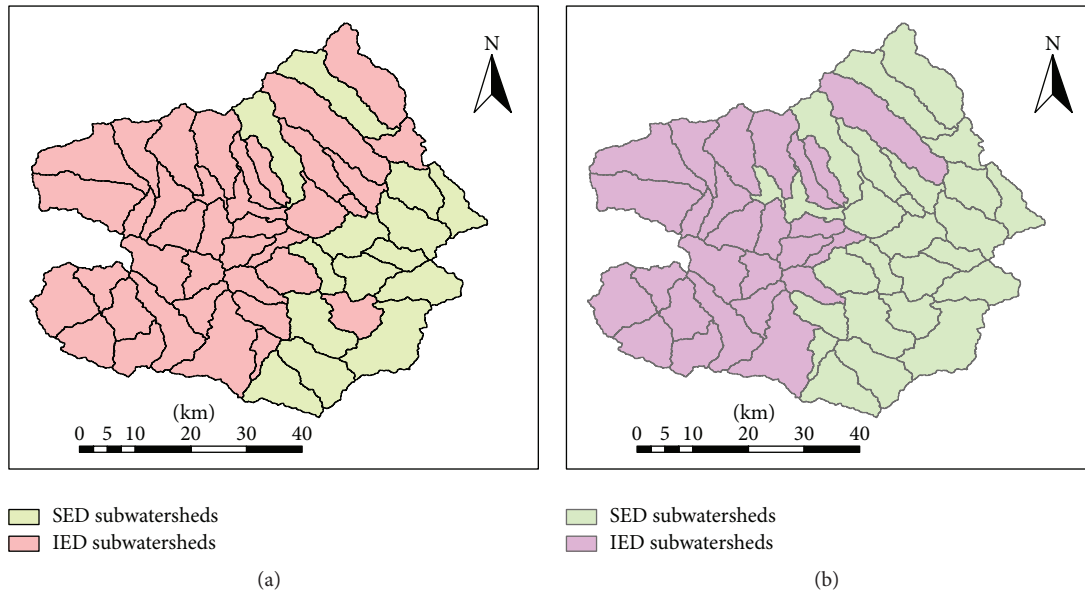


FIGURE 6: Division results of the saturation-excess dominated (SED) subwatersheds and infiltration-excess dominated (IED) subwatersheds for Dongwan watershed. (a) CN division method and (b) CN-TI division method.

are concentrated in the upstream. The result suggests that, without the disturbing effects of human activities, terrain factors are somewhat correlated to vegetation and soil factors; for example, soil infiltration capacity and vegetation cover on steep slopes are usually lower than those on gentle slopes.

4.2. Results of Parameter Calibration. Table 3 shows the optimized parameters of XAJ model and infiltration-excess model. For XAJ model, the parameter S_M which is highly associated with runoff separation has a value of only 26 mm. The smaller the S_M value, the larger the proportion of surface runoff. In XAJ model, surface runoff refers to the saturation-excess overland flow. It is obvious that saturated surface runoff is not likely to account for a large proportion of total runoff in such a watershed. In fact, infiltration-excess runoff is treated as saturation-excess runoff in XAJ model for Dongwan watershed.

For infiltration-excess model, the parameter value of k_{im} is only 0.4, less than 0.5. The closer to 1 k_{im} is, the greater the effect of antecedent soil moisture content on direct runoff generation is, and the closer to the saturation-excess mechanism is. On the contrary, the closer to 0 k_{im} is, the greater the effect of current rainfall infiltration is, and the closer to the infiltration-excess mechanism is. The value of the k_{im} indicates that the effect of infiltration-excess mechanism is quite large in Dongwan watershed, even larger than that of saturation-excess mechanism.

Table 4 shows the optimization result of two SCM models. Contrasted with XAJ model, the S_M value increases from 26 mm to 34~35 mm, which means that the proportion of saturated surface runoff is reduced. In SCM model the overland flow is divided into saturation-excess overland flow in SED areas and infiltration-excess overland flow in IED areas. The reduced saturation-excess overland flow is replaced

by the increased infiltration-excess overland flow, which is more consistent with the actual condition in Dongwan watershed.

Changes in parameter values associated with (7) and (8) are more complicated. k_{im} is insensitive with little change. f_c and u are sensitive parameters, both of which can affect infiltration capacity according to (7). Hence, the effect of equifinality cannot be ruled out. In general, compared to infiltration-excess model and SCM I, the areal average infiltration capacity in SCM II is relatively lower and consequently the amount of infiltration-excess runoff is relatively higher, which is more consistent with actual conditions as discussed in Section 5. In SCM model the entire watershed is divided into SED areas and IED areas and the overland flow is also divided into saturation-excess and infiltration-excess overland flow. Therefore, the representation of runoff generation mechanism in the semihumid watershed is clearer and more precise.

4.3. Results of Simulation and Validation. The model simulation results are shown in Table 5. For XAJ model, the qualified rates of runoff depth simulation and peak flow simulation are both 68.8%; for infiltration-excess model, the qualified rate of runoff depth simulation is 68.8% and the qualified rate of peak flow simulation is 62.8%, almost equal to XAJ model, which reflects the problem of model structure uncertainty; for SCM I, both are 75%; and for SCM II, the qualified rate of runoff depth simulation is 75% and the qualified rate of peak flow simulation is 81.3%, showing a large improvement of simulation accuracy.

Peak flow forecasting is a crucial factor for flood forecasting and warning in small and medium watersheds. There are only three unqualified peak flow forecasts by SCM II, which are the forecasts of 960802, 070729, and 090828 flood events

TABLE 3: The optimized parameters of the single runoff models.

XAJ model			Infiltration-excess model		
Parameter meaning	Notation	Value	Parameter meaning	Notation	Value
Ratio of potential evapotranspiration to pan evaporation	K	0.65	Ratio of potential evapotranspiration to pan evaporation	K	0.65
Exponential parameter with a single parabolic curve, which represents the nonuniformity of the spatial distribution of the soil moisture storage capacity over the catchment	b	0.3	Exponential parameter with a single parabolic curve, which represents the nonuniformity of the spatial distribution of the soil moisture storage capacity over the watershed	b	0.3
Coefficient of the deep layer that depends on the proportion of the basin area covered by vegetation with deep roots	C	0.08	Coefficient of the deep layer that depends on the proportion of the basin area covered by vegetation with deep roots	C	0.08
Averaged soil moisture storage capacity (mm)	W_M	180	Averaged soil moisture storage capacity (mm)	W_M	180
Averaged soil moisture storage capacity of the upper layer (mm)	W_{UM}	20	Averaged soil moisture storage capacity of the upper layer (mm)	W_{UM}	20
Averaged soil moisture storage capacity of the lower layer (mm)	W_{LM}	70	Averaged soil moisture storage capacity of the lower layer (mm)	W_{LM}	90
Percentage of impervious areas in the watershed	I_M	0.01	A coefficient representing the ratio of surface soil thickness to the vadose zone thickness	k_{im}	0.4
Areal mean free water capacity of the surface soil layer, which represents the maximum possible deficit of free water storage	S_M	26	Steady-state infiltration capacity ($\text{mm}\cdot\text{h}^{-1}$)	f_c	1.5
Exponent of the free water capacity curve influencing the development of the saturated area	E_X	1.2	Exponent of the spatial infiltration capacity distribution curve	E_X	1.6
Outflow coefficients of the free water storage to groundwater relationships	K_G	0.35	Infiltration coefficient of the improved Horton equation	u	0.006
Outflow coefficients of the free water storage to interflow relationships	K_I	0.35	Recession constants of the interflow and groundwater storage	C_{IG}	0.95
Recession constants of the groundwater storage	C_G	0.998	The maximum point infiltration capacity in the watershed ($\text{mm}\cdot\text{h}^{-1}$)	f_{mm}	312
Recession constants of the lower interflow storage	C_I	0.954	Recession constants in the lag and route method for routing through the channel system within each subbasin	C_S	0.057
Recession constants in the lag and route method for routing through the channel system within each subbasin	C_S	0.014	Lag in time (h)	L	0
Lag in time (h)	L	0			

with the relative errors of the peak flows 41.2%, 93.8%, and 125%, respectively. Such large forecast errors indicate that the abnormal results are caused not only by the model structure but also by the resolution and quality of hydrological data; for example, rainfall data fail to capture the storm center. XAJ model, infiltration-excess model, and SCM I also cannot make qualified forecasts of the three flood events. Therefore, we compare the forecast results of the four models excluding the three flood events.

Table 6 shows the model results in the validation period. The qualified rates of peak flows for XAJ model, infiltration-excess model, SCM I, and SCM II are 57.1%, 42.8%, 57.1%, and 71.4%, respectively. Complex models often have high accuracy in the calibration period, but low accuracy in

the validation period, due to overparameterization and overfitting [39]. The structure of SCM is more complex than that of XAJ model and infiltration-excess model, but its accuracy in the validation period is not lower, which indicates that the model performance is stable.

5. Analysis of Two Flood Examples

In this section the 060926 and 080720 flood events are taken as examples to assess the performances of the four models. Their hydrographs are shown in Figure 7.

For the 060926 flood event, the simulated peak flow of XAJ model is significantly greater than the observed peak flow, while the relative errors of the peak flow of the other

TABLE 4: The optimized parameters of the spatial combination models.

Parameter meaning	SCM I	SCM II
Ratio of potential evapotranspiration to pan evaporation K	0.65	0.65
Exponential parameter with a single parabolic curve, which represents the nonuniformity of the spatial distribution of the soil moisture storage capacity over the watershed b	0.3	0.3
Coefficient of the deep layer that depends on the proportion of the basin area covered by vegetation with deep roots C	0.08	0.08
Averaged soil moisture storage capacity W_M (mm)	180	180
Averaged soil moisture storage capacity of the upper layer W_{UM} (mm)	20	20
Averaged soil moisture storage capacity of the lower layer W_{LM} (mm)	90	90
Percentage of impervious areas in the watershed I_M	0.01	0.01
Areal mean free water capacity of the surface soil layer, which represents the maximum possible deficit of free water storage S_M (mm)	35	34
Exponent of the free water capacity curve influencing the development of the saturated area E_X	1.2	1.2
Outflow coefficients of the free water storage to groundwater relationships K_G	0.35	0.35
Outflow coefficients of the free water storage to interflow relationships K_I	0.35	0.35
Recession constants of the groundwater storage C_G	0.998	0.998
Recession constants of the lower interflow storage C_I	0.768	0.902
Recession constants in the lag and route method for routing through the channel system within each subbasin C_S	0.038	0.026
Lag in time L (h)	0	0
Coefficient representing the ratio of surface soil thickness to the vadose zone thickness k_{im}	0.4	0.4
Steady-state infiltration capacity f_c (mm·h ⁻¹)	1	1.2
Infiltration coefficient of the improved Horton equation u	0.004	0.007
The maximum point infiltration capacity in the watershed f_{mm} (mm·h ⁻¹)	249	211
Exponent of the spatial infiltration capacity distribution curve E_X	1.5	1.7
Recession constants of the interflow and groundwater storage C_{IG}	0.949	0.958

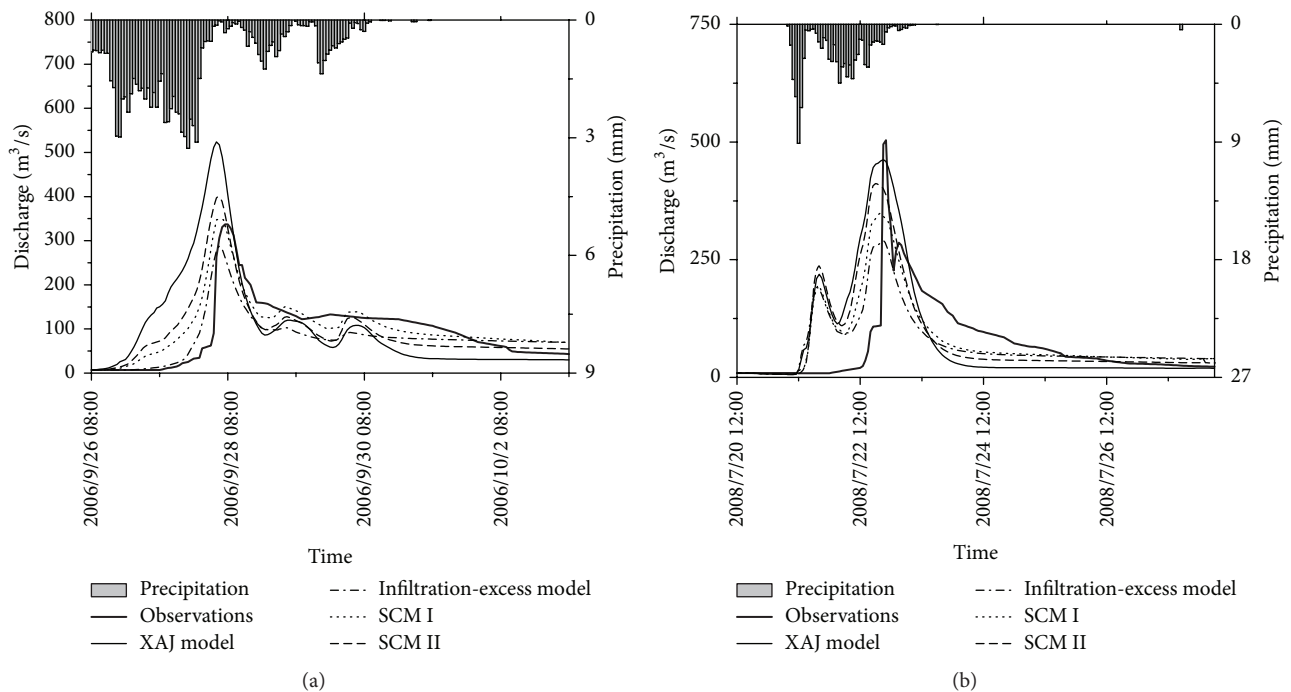


FIGURE 7: Observed and simulated runoff hydrographs for two events. (a) September 2006 and (b) July 2008.

TABLE 5: The simulation results of the models in the calibration period.

Flood number	Observed runoff (mm)	Observed peak flow (m^3/s)	XAJ model		Infiltration-excess model		SCM I		SCM II	
			Relative runoff error (%)	Relative peak error (%)	Relative runoff error (%)	Relative peak error (%)	Relative runoff error (%)	Relative peak error (%)	Relative runoff error (%)	Relative peak error (%)
940702	15.4	1210	37.9	8.8	35.7	-24.2	49.9	-1.4	48.0	6.2
950811	27.2	836	-3.8	17.9	10.8	8.8	8.0	5.2	5.7	10.3
960802	87.9	1730	-41.0	-46.8	-32.4	-46.2	-28.6	-39.0	-35.3	-41.2
980813	37.1	1320	-14.9	7.4	4.0	18.7	3.7	19.5	-7.3	13.1
000712	34.1	1770	-33.6	-32.9	-1.6	-11.5	-7.9	-12.9	-18.6	-17.1
010729	12.9	461	3.3	-8.5	6.7	-12.0	12.1	-6.5	10.5	-2.1
020626	15.4	411	-26.5	-2.5	-17.5	-13.8	-16.8	-10.9	-12.8	13.9
030831	53.7	1430	-1.9	-9.0	-7.5	-18.5	5.7	-5.2	-3.3	-12.6
040716	11.1	699	6.5	-18.5	23.9	-18.4	16.8	-14.2	25.2	3.4
050816	44.9	1090	-33.2	-15.1	-30.8	-34.3	-18.7	-19.8	-27.0	-19.1
060926	19.9	337	12.6	55.5	-15.1	-14.5	11.6	7.1	4.1	19.3
070729	29.7	812	19.4	72.7	47.0	78.0	50.4	93.2	40.8	93.8
080720	16.3	504	16.4	-8.2	3.0	-42.2	14.9	-30.3	16.4	-18.2
090828	15.3	287	5.0	120.3	8.2	71.1	19.1	94.2	15.1	125.0
100722	97.4	3780	11.1	19.6	23.4	6.4	28.5	17.8	19.6	18.3
110911	71.4	1570	-12.7	12.3	-4.7	5.2	5.1	19.5	-6.2	13.0

TABLE 6: The simulation results of the models in the validation period.

Flood number	Observed runoff (mm)	Observed peak flow (m^3/s)	XAJ model		Infiltration-excess model		SCM I		SCM II	
			Relative runoff error (%)	Relative peak error (%)	Relative runoff error (%)	Relative peak error (%)	Relative runoff error (%)	Relative peak error (%)	Relative runoff error (%)	Relative peak error (%)
810714	14.6	482	-40.4	-15.9	-45.4	-45.8	-36.5	-31.1	-31.2	-15.6
820731	80.3	3500	-3.0	-18.7	-3.7	-24.6	-2.2	-18.9	-6.5	-19.6
820812	19.9	274	-34.1	-44.1	-6.7	-14.3	-7.0	-8.3	-19.6	-19.8
830810	29.9	451	-44.9	-19.2	-32.4	-15.4	-31.7	-13.0	-38.4	-14.8
831003	72.1	1290	-13.5	15.7	-14.8	7.3	-3.5	18.7	-13.5	13.7
831017	29.9	440	-43.4	-39.3	-37.2	-37.8	-28.6	-30.3	-37.9	-42.6
840908	45.4	888	-31.6	-23.3	-35.9	-37.8	-23.0	-24.0	-29.7	-30.1

three models are in the 20% acceptable range. There was a heavy rain in the early September in 2006 and another heavy rain occurring around September 20. When the latter rain started on the evening of September 25, the soil was moist and the antecedent soil moisture content was about 130 mm~140 mm according to the daily water budget calculation. From the evening of September 25 to September 30, the rainfall continued and the total rainfall amount was large, which caused a large runoff according to the simulation result of XAJ model. As mentioned above, in XAJ model in semihumid watersheds, infiltration-excess runoff is replaced by saturation-excess runoff; therefore, when the antecedent soil moisture content is large, saturation-excess runoff is highly possible to occur, causing the simulated peak flow remarkably larger than the observed record. It also indicates that in mixed runoff watersheds the simulated peak flow of saturation-excess model is not always below the observed record and may be equal to or higher than it, but its underlying assumptions are not suitable for mixed runoff watersheds.

The infiltration-excess features of the 080720 flood event are more apparent compared to the 060926 flood event; for example, its hydrograph is much sharper. However, the simulation results are really interesting: XAJ model and SCM II can make a qualified peak flow forecast while the simulated peak flows of infiltration-excess model and SCM I, especially infiltration-excess model, are significantly lower than the actual record. Two rainfall peaks took place during the flood event. The first one happened between 12:00 and 13:00 on the July 21, 2008, with its storm center located among Tantou, Heyu, and Dongwan stations in the downstream, which were mainly SED areas. The second one occurred around 7:00 on the July 22 with the storm center located in Luanchuan in the upstream within IED areas. At the beginning of the rainfall, the soil was relatively dry with the antecedent soil moisture content around 110 mm. Therefore, the rainwater of the first rainfall peak mainly infiltrated into the soil and the rainwater of the second rainfall peak mainly generated infiltration-excess runoff.

Although XAJ model can accurately reproduce the peak flow discharge of the 080720 flood event, its underlying assumptions are not applicable to Dongwan watershed. Despite the fact that the runoff mechanism of infiltration-excess model is closer to the reality of Dongwan watershed, the optimized model parameters are far deviated from their physical meanings. Similarly, as the optimized S_M parameter of XAJ model is too small, the areal average infiltration capacity calculated by the infiltration-excess model is too large, which in turn causes the proportion of infiltration-excess runoff too small.

The simulated peak flows of the 080720 and 060926 flood events by infiltration-excess model are both smaller than the observed peak flow, indicating that even if the runoff mechanism represented by the model structure is close to the actual watershed condition, parameter identification is still a critical problem affecting simulation accuracies. Should the areal average infiltration capacity calculated by infiltration-excess model be reduced to increase the infiltration-excess overland flow? The answer should be “no.” There are also

SED flood events in Dongwan watershed; therefore, if the infiltration capacity is reduced, the simulated peak flows of SED flood events would be dramatically larger than the observed peak flows. That is to say, the calculated infiltration capacity by models may be greatly different from the actual infiltration capacity, just an “effective” variable.

SCM I also has the problem of the infiltration capacity being too large, but not obvious. This indicates that if the divisions of the SED and IED areas are precise enough, the parameter values and model variables would be closer to reality and the errors of model simulation will be reduced.

There is a peak in the simulated flood from all models around July 21, but there is no peak in the observed data. The observed data are basically flat in that period. This can be explained by the use of the parabolic distribution curve, which is described in Figures 2 and 3. The curve represents the spatial heterogeneity of hydrological variables; for example, soil water storage capacity is low in some points and high in some other points. With the use of these models, some points, such as the points with low storage capacity or low infiltration capacity, are prone to produce runoff. But in fact, no points produced runoff in the first rainfall peak. If the parabolic distribution is replaced by the uniform distribution, there may not be a peak in the simulated flood around July 21. In our future study, we will further investigate what conditions are applicable to the parabolic and uniform distribution, respectively.

6. Conclusion

This paper proposed the spatial combination modeling framework for event hydrological simulation. In this framework, the watershed is divided into saturation-excess dominated areas and infiltration-excess dominated areas by the joint use of curve number and topographic index, reflecting the phenomenon of saturation-excess runoff and infiltration-excess runoff coexisting during a storm. The spatial combination model was also built according to the framework.

A semihumid watershed was taken as an example to test the framework. It can be found that

- (1) the terrain factors are somewhat correlated to vegetation and soil factors. Therefore, the IED areas are mainly located in the upstream and the SED areas mainly in the downstream;
- (2) the SCM outperforms the saturation-excess model and the infiltration-excess model both in the calibration and validation periods. The performance of the SCM is closely related to the division of SED and IED areas. A reasonable division can produce more realistic parameter values and better performances.

The results exhibit the importance of model realism for the event hydrological simulation. In the future study, the fuzzy approach and probabilistic approach will be used to seek for a more appropriate division of IED and SED areas within a watershed. In addition, this framework will be applied to a variety of semihumid watersheds based on the concept of “large-sample hydrology” [40].

Conflict of Interests

The authors declare that there is no conflict of interests regarding the publication of this paper.

Acknowledgments

This work was supported by the National Natural Science Foundation of China (Grant nos. 41130639, 51179045, and 41201028), the Nonprofit Industry Financial Program of MWR of China (201501022 and 201301068), the Meteorological Research Fund for Huaihe River Basin (HRM201404), and National Cooperative Innovation Center for Water Safety & Hydro-Science.

References

- [1] M. Hrachowitz, H. H. G. Savenije, G. Blöschl et al., “A decade of Predictions in Ungauged Basins (PUB)—a review,” *Hydrological Sciences Journal*, vol. 58, no. 6, pp. 1198–1255, 2013.
- [2] T. Euser, H. C. Winsemius, M. Hrachowitz, F. Fenicia, S. Uhlenbrook, and H. H. G. Savenije, “A framework to assess the realism of model structures using hydrological signatures,” *Hydrology and Earth System Sciences*, vol. 17, no. 5, pp. 1893–1912, 2013.
- [3] S. Gharari, M. Hrachowitz, F. Fenicia, H. Gao, and H. H. G. Savenije, “Using expert knowledge to increase realism in environmental system models can dramatically reduce the need for calibration,” *Hydrology and Earth System Sciences*, vol. 18, no. 12, pp. 4839–4859, 2014.
- [4] H. Gao, M. Hrachowitz, F. Fenicia, S. Gharari, and H. H. G. Savenije, “Testing the realism of a topography-driven model (FLEX-Topo) in the nested catchments of the Upper Heihe, China,” *Hydrology and Earth System Sciences*, vol. 18, no. 5, pp. 1895–1915, 2015.
- [5] J. E. Nash and J. V. Sutcliffe, “River flow forecasting through conceptual models part I—a discussion of principles,” *Journal of Hydrology*, vol. 10, no. 3, pp. 282–290, 1970.
- [6] M. P. Clark, A. G. Slater, D. E. Rupp et al., “Framework for understanding structural errors (FUSE): a modular framework to diagnose differences between hydrological models,” *Water Resources Research*, vol. 44, no. 12, Article ID W00B02, 2008.
- [7] M. P. Clark, D. Kavetski, and F. Fenicia, “Pursuing the method of multiple working hypotheses for hydrological modeling,” *Water Resources Research*, vol. 47, no. 9, Article ID W09301, 2011.
- [8] F. Fenicia, D. Kavetski, H. H. G. Savenije et al., “Catchment properties, function, and conceptual model representation: is there a correspondence?” *Hydrological Processes*, vol. 28, no. 4, pp. 2451–2467, 2014.
- [9] H. H. G. Savenije, “HESS opinions ‘topography driven conceptual modelling (FLEX-Topo)’,” *Hydrology and Earth System Sciences*, vol. 14, no. 12, pp. 2681–2692, 2010.
- [10] T. C. Winter, “The concept of hydrologic landscapes,” *Journal of the American Water Resources Association*, vol. 37, no. 2, pp. 335–349, 2001.
- [11] D. M. Wolock, T. C. Winter, and G. McMahon, “Delineation and evaluation of hydrologic-landscape regions in the United States using geographic information system tools and multivariate statistical analyses,” *Environmental Management*, vol. 34, no. 1, pp. S71–S88, 2004.
- [12] T. Euser, M. Hrachowitz, H. C. Winsemius, and H. H. Savenije, “The effect of forcing and landscape distribution on performance and consistency of model structures,” *Hydrological Processes*, vol. 29, no. 17, pp. 3727–3743, 2015.
- [13] R. A. Freeze, “Mathematical models of hillslope hydrology,” in *Hillslope Hydrology*, M. J. Kirby, Ed., pp. 177–225, John Wiley & Sons, New York, NY, USA, 1978.
- [14] T. Dunne and R. D. Black, “Partial area contributions to storm runoff in a small New England watershed,” *Water Resources Research*, vol. 6, no. 5, pp. 1296–1311, 1970.
- [15] R. E. Horton, “The rôle of infiltration in the hydrologic cycle,” *Eos, Transactions American Geophysical Union*, vol. 14, no. 1, pp. 446–460, 1933.
- [16] T. Dunne, “Field studies of hillslope flow processes,” in *Hillslope Hydrology*, M. J. Kirby, Ed., pp. 227–293, John Wiley & Sons, New York, NY, USA, 1978.
- [17] R. J. Chorley, “The hillslope hydrologic cycle,” in *Hillslope Hydrology*, M. J. Kirby, Ed., pp. 1–42, John Wiley & Sons, New York, NY, USA, 1978.
- [18] D. H. Pilgrim, T. G. Chapman, and D. G. Doran, “Problems of rainfall-runoff modelling in arid and semiarid regions,” *Hydrological Sciences Journal*, vol. 33, no. 4, pp. 379–400, 1988.
- [19] C. W. Downer, F. L. Ogden, W. D. Martin, and R. S. Harmon, “Theory, development, and applicability of the surface water hydrologic model CASC2D,” *Hydrological Processes*, vol. 16, no. 2, pp. 255–275, 2002.
- [20] R. J. C. Burnash, “The NWS river forecast system—catchment modeling,” in *Computer Models of Watershed Hydrology*, V. P. Singh, Ed., pp. 311–366, Water Resources Publications, Highlands Ranch, Colo, USA, 1995.
- [21] D. A. Burns, J. J. McDonnell, R. P. Hooper et al., “Quantifying contributions to storm runoff through end-member mixing analysis and hydrologic measurements at the Panola Mountain Research Watershed (Georgia, USA),” *Hydrological Processes*, vol. 15, no. 10, pp. 1903–1924, 2001.
- [22] A. R. Buda, P. J. A. Kleinman, M. S. Srinivasan, R. B. Bryant, and G. W. Feyereisen, “Factors influencing surface runoff generation from two agricultural hillslopes in central Pennsylvania,” *Hydrological Processes*, vol. 23, no. 9, pp. 1295–1312, 2009.
- [23] S. K. Mishra and V. P. Singh, *Soil Conservation Service Curve Number (SCS-CN) Methodology*, Kluwer Academic Publishers, Dordrecht, The Netherlands, 2003.
- [24] K. J. Beven and M. J. Kirkby, “A physically based, variable contributing area model of basin hydrology,” *Hydrological Sciences Journal*, vol. 24, no. 1, pp. 43–69, 1979.
- [25] C. Yao, K. Zhang, Z. Yu, Z. Li, and Q. Li, “Improving the flood prediction capability of the Xinanjiang model in ungauged nested catchments by coupling it with the geomorphologic instantaneous unit hydrograph,” *Journal of Hydrology*, vol. 517, pp. 1035–1048, 2014.
- [26] H. Xu, C.-Y. Xu, H. Chen, Z. Zhang, and L. Li, “Assessing the influence of rain gauge density and distribution on hydrological model performance in a humid region of China,” *Journal of Hydrology*, vol. 505, pp. 1–12, 2013.
- [27] Z. Ren-Jun, “The Xinanjiang model applied in China,” *Journal of Hydrology*, vol. 135, no. 1–4, pp. 371–381, 1992.
- [28] R. Zhao and X. Liu, “The Xinanjiang model,” in *Computer Models of Watershed Hydrology*, V. P. Singh, Ed., pp. 215–232, Water Resources Publications, Highlands Ranch, Colo, USA, 1995.

- [29] Y.-L. Chen and J.-T. Han, "Problems on flood forecasting in the semi-arid region," *Advances in Water Science*, vol. 14, no. 5, pp. 612–616, 2003 (Chinese).
- [30] J. R. Craig, G. Liu, and E. D. Soulis, "Runoff–infiltration partitioning using an upscaled Green–Ampt solution," *Hydrological Processes*, vol. 24, no. 16, pp. 2328–2334, 2010.
- [31] A. Basist, G. D. Bell, and V. Meentemeyer, "Statistical relationships between topography and precipitation patterns," *Journal of Climate*, vol. 7, no. 9, pp. 1305–1315, 1994.
- [32] H. Xu and W. Yao, "A numerical study of the Beijing extreme rainfall of 21 July 2012 and the impact of topography," *Advances in Meteorology*, vol. 2015, Article ID 980747, 12 pages, 2015.
- [33] B. Sivakumar, "Dominant processes concept, model simplification and classification framework in catchment hydrology," *Stochastic Environmental Research and Risk Assessment*, vol. 22, no. 6, pp. 737–748, 2008.
- [34] Q. Duan, S. Sorooshian, and V. Gupta, "Effective and efficient global optimization for conceptual rainfall-runoff models," *Water Resources Research*, vol. 28, no. 4, pp. 1015–1031, 1992.
- [35] Q. Duan, S. Sorooshian, and V. K. Gupta, "Optimal use of the SCE-UA global optimization method for calibrating watershed models," *Journal of Hydrology*, vol. 158, no. 3-4, pp. 265–284, 1994.
- [36] M. Shafi and B. A. Tolson, "Optimizing hydrological consistency by incorporating hydrological signatures into model calibration objectives," *Water Resources Research*, vol. 51, no. 5, pp. 3796–3814, 2015.
- [37] National Center of Hydrological Information, *Standard for Hydrological Information and Hydrological Forecasting*, China WaterPower Press, Beijing, China, 2000 (Chinese).
- [38] C. Zhang, R.-B. Wang, and Q.-X. Meng, "Calibration of conceptual rainfall-runoff models using global optimization," *Advances in Meteorology*, vol. 2015, Article ID 545376, 12 pages, 2015.
- [39] G. Whittaker, R. Confesor Jr., M. Di Luzio, and J. G. Arnold, "Detection of overparameterization and overfitting in an automatic calibration of SWAT," *Transactions of the ASABE*, vol. 53, no. 5, pp. 1487–1499, 2010.
- [40] H. V. Gupta, C. Perrin, G. Blöschl et al., "Large-sample hydrology: a need to balance depth with breadth," *Hydrology and Earth System Sciences*, vol. 18, no. 2, pp. 463–477, 2014.

Research Article

Relationship between Evapotranspiration and Land Surface Temperature under Energy- and Water-Limited Conditions in Dry and Cold Climates

Zhigang Sun,^{1,2} Qinxue Wang,³ Ochirbat Batkhishig,⁴ and Zhu Ouyang^{1,2}

¹Key Laboratory of Ecosystem Network Observation and Modeling, Institute of Geographic Sciences and Natural Resources Research, Chinese Academy of Sciences, Beijing 100101, China

²Yucheng Comprehensive Experimental Station, Institute of Geographic Sciences and Natural Resources Research, Chinese Academy of Sciences, Beijing 100101, China

³Center for Regional Environmental Research, National Institute for Environmental Studies, Tsukuba 305-8506, Japan

⁴Institute of Geography, Mongolian Academy of Sciences, 14192 Ulaanbaatar, Mongolia

Correspondence should be addressed to Zhigang Sun; sunzg@igsnr.ac.cn

Received 24 May 2015; Revised 29 September 2015; Accepted 7 October 2015

Academic Editor: Ke Zhang

Copyright © 2016 Zhigang Sun et al. This is an open access article distributed under the Creative Commons Attribution License, which permits unrestricted use, distribution, and reproduction in any medium, provided the original work is properly cited.

Remotely sensed land surface temperature- (LST-) dependent evapotranspiration (ET) models and vegetation index- (VI-) LST methods may not be suitable for ET estimation in energy-limited cold areas. In this study, the relationship of ET to LST was simulated using the process-based Simultaneous Heat and Water (SHAW) model for energy- and water-limited conditions in Mongolia, to understand the differences in ET processes under these two limiting conditions in dry and cold climates. Simulation results from the SHAW model along with ground observational data showed that ET and LST have a positive relationship when air temperature (T_a) is less than or equal to the temperature (T_{tra}) above which plants transpire and have a negative relationship when T_a is greater than T_{tra} under the energy-limited condition. However, ET and LST maintain a negative relationship with changes in T_a under the water-limited condition. The differences in the relationship between ET and LST under the energy-limited and water-limited conditions could be attributed to plant transpiration and energy storage in moist/watered soil and plants. This study suggests that different strategies should be used to estimate ET under the energy-limited condition in dry and cold climates.

1. Introduction

Terrestrial evapotranspiration (ET), defined as the loss of water from the land surface to the atmosphere, is a key process in water cycles [1, 2]. ET closely relates to greenhouse gas efflux and production [3], plant growth [4–6], and droughts [7, 8]. Therefore, it is essential to understand the ET phenomenon over wide ranges of space and time for water resources management and climate change studies.

Regional or global ET maps are often obtained through satellite remote sensing [9, 10]. Among remote sensing-based ET estimation methods, remotely sensed land surface temperature- (LST) dependent methods, such as the vegetation index (VI) and LST scattered plot (VI-LST), and models that calculate ET as a residual of the land

surface energy balance equation have been widely used. The LST-dependent ET models include SEBAL (remote sensing Surface Energy Balance Algorithm for Land) [11], Sim-ReSET (Simple Remote Sensing EvapoTranspiration model) [9], SEBI (Surface Energy Balance Index) and S-SEBI (Simplified-SEBI) [12], SEBS (Surface Energy Balance System) [13], and METRIC (Mapping EvapoTranspiration at high Resolution with Internalized Calibration) [14, 15], among others. The VI-LST methods use the VI-LST triangle/trapezoidal feature space to derive an index, and this index is used to partition sensible heat and latent heat fluxes from available energy (net radiation minus soil heat flux) [16–19]. Both LST-dependent ET models and VI-LST methods assume that ET can cool land surfaces under the condition of homogeneous atmospheric forcing. In other words, land surfaces with larger

TABLE 1: Main inputs to the SHAW model.

Date type	Data item	Unit	Data source
Weather data	Air temperature	°C	AMS
	Air humidity	%	AMS
	Precipitation	Inch	AMS
	Wind speed	mph	AMS
	Solar radiation	W/m ²	AMS
Soil data	Bulk density	kg/m ³	Soil sample
	Organic matter	%	Soil sample
	Sand	%	Soil sample
	Silt	%	Soil sample
	Clay	%	Soil sample
	Soil temperature	°C	AMS
	Soil moisture	m ³ /m ³	AMS
Vegetation data	Vegetation canopy height	m	Vegetation sample
	Dry matter	kg/m ²	Vegetation sample
	Leaf area index	—	Vegetation sample
	Root depth	m	Vegetation sample
General site information	Slope	%	Field survey
	Aspect	Degree	Field survey
	Latitude	Degree	GPS
	Elevation	m	GPS

ET have lower LST while air temperature (T_a), air humidity, wind speed, and solar radiation remain homogeneous over land surfaces of interest. However, this assumption may be invalid in high latitudes ($>50^\circ$) and cold areas [2], where ET commonly exhibits a positive relationship with LST [2, 20]. A positive relationship between LST and VI has also been observed in Alaska tundra ecosystems [21] and in North America above 45°N [22]. These findings indicate that both LST-dependent ET models and VI-LST methods may not be suitable for ET estimation in the energy-limited cold areas. A study to estimate water deficit (defined as the ratio of actual to potential ET) using the VI-LST method in southern Spain also suggests that the VI-LST method should not be used to calculate ET under energy-limited conditions [19].

Reasons for the incompetence of LST-dependent ET models and VI-LST methods in energy-limited cold areas have been seldom investigated so far. In this study, the relationship between ET and LST was investigated using the process-based Simultaneous Heat and Water (SHAW) model for energy- and water-limited conditions in Mongolia, to understand the difference in ET processes under such limiting conditions in dry and cold climates.

2. Methodology

2.1. SHAW Model. The Simultaneous Heat and Water (SHAW) model, a one-dimensional model that simulates heat, water, and solute transfer within the atmosphere-plant-soil system, was used to simulate ET and LST in this study. The SHAW model, developed by USDA Agricultural Research Service, has a detailed solution to simulate soil

freezing and thawing and a sophisticated approach to simulate transpiration from a plant canopy and evaporation from soil [23, 24]. The SHAW model has been documented that it is capable to simulate heat and water movement through plant cover, snow, residue, and soil for investigating climate and anthropogenic effects on soil freezing, snowmelt, runoff, soil temperature, water, evaporation, and transpiration [23, 24]. Therefore, the calibrated SHAW model could be competent at numerically simulating the relationship between ET and LST.

Vegetation, climate, and soil data are required to run the SHAW model. These inputs include initial conditions for snow, soil temperature, and water content profiles; daily or hourly weather data; and parameters describing the vegetative cover, snow, residue, and soil. General site information is also needed to initialize the model, including the slope, aspect, latitude, and surface roughness parameters. Detailed information on these input parameters is listed in Table 1.

2.2. Data

Weather Data. Hourly air temperature (T_a), wind speed, air humidity, precipitation, and solar radiation data were collected from an auto-meteorological station (AMS; 47.75°N 107.33°E) located near Ulaanbaatar in Mongolia. A dry and cold climate dominates the region around the AMS, with an annual mean air temperature of -2.8°C and annual total precipitation of 260 mm. Detailed information regarding the AMS can be found in Sun et al. [25].

Soil Data. Data for organic matter content, bulk density, and soil component ratio of sand, silt, and clay were obtained from

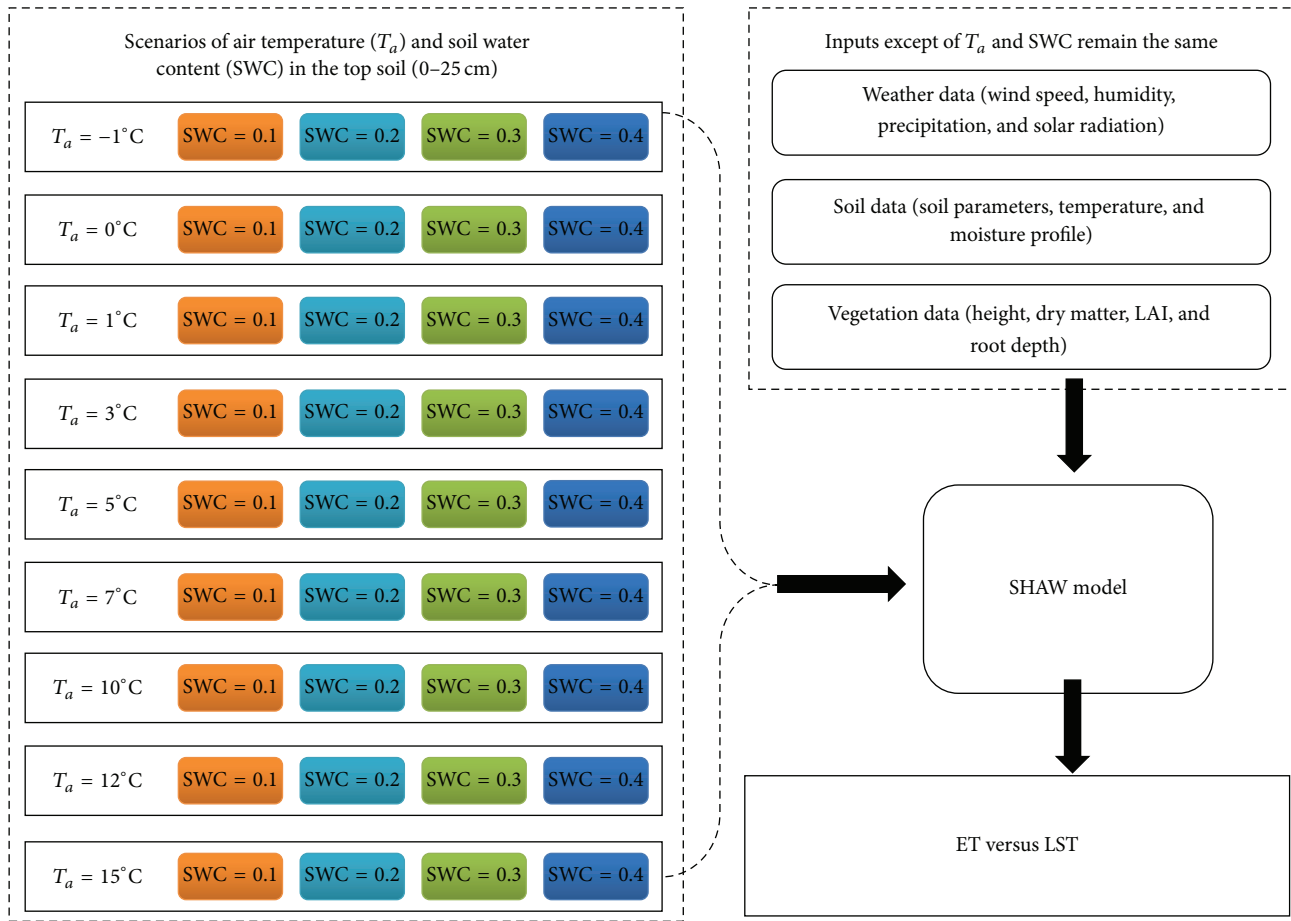


FIGURE 1: Strategies to simulate ET and LST using the SHAW model.

soil samples that were analyzed in the lab. Soil temperature and moisture profile data were obtained from the AMS.

Vegetation Data. Grass height, dry matter, leaf area index (LAI), and root depth data were obtained by measuring grass samples.

2.3. Strategies for ET and LST Simulations. In this study, nine scenarios of T_a and four scenarios of topsoil water content (SWC, 0–25 cm) were combined to simulate ET and LST for energy- and water-limited conditions. T_a was set at -1 – 15°C to match the local cold climate, and SWC was set at 0.1–0.4 to cover the soil moisture range from dry to wet. Combinations of T_a and SWC could thereby simulate a wide range of energy and water conditions under which ET and LST are simulated using the SHAW model (Figure 1). The scenario of SWC = 0.1 represents the water-limited condition where ET is mainly limited by soil water shortage. The scenario of SWC = 0.4 with low T_a values represents the energy-limited condition where ET is mainly limited by low incoming solar radiation. Since low incoming solar radiation leads to low T_a , the proxy of low T_a along with saturated soil water content could be used to define the energy-limited condition. One combination of T_a and SWC along with other inputs was used to run the model. For each model run, the SWC data were used to initialize the

moisture condition for the soil layer of 0–25 cm, and T_a data along with other weather data representing typical weather conditions at the AMS site in early spring were selected from the AMS dataset. A typical record of T_a and other weather data was repeated 84 times to simulate the condition of homogeneous atmospheric forcing. Therefore, ET and LST values from each run of the SHAW model represent the water and heat conditions of land surfaces under homogeneous atmospheric forcing. Outputted ET and LST values were plotted and analyzed using the linear regression method, and the slope and coefficient of determination (R^2) of the linear regression were used to understand the relationship of ET to LST under different energy and moisture conditions.

Before numerical simulations, intensive daily observational data during the period of August 2008 to August 2013 were used to calibrate the SHAW model by forcing the simulated soil temperature and water content to be consistent with observed values, respectively.

3. Results and Discussion

When the SHAW model was calibrated, simulations of nine scenarios of T_a (-1 to 15°C) and four scenarios of topsoil water content (SWC = 0.1, 0.2, 0.3, and 0.4) were conducted

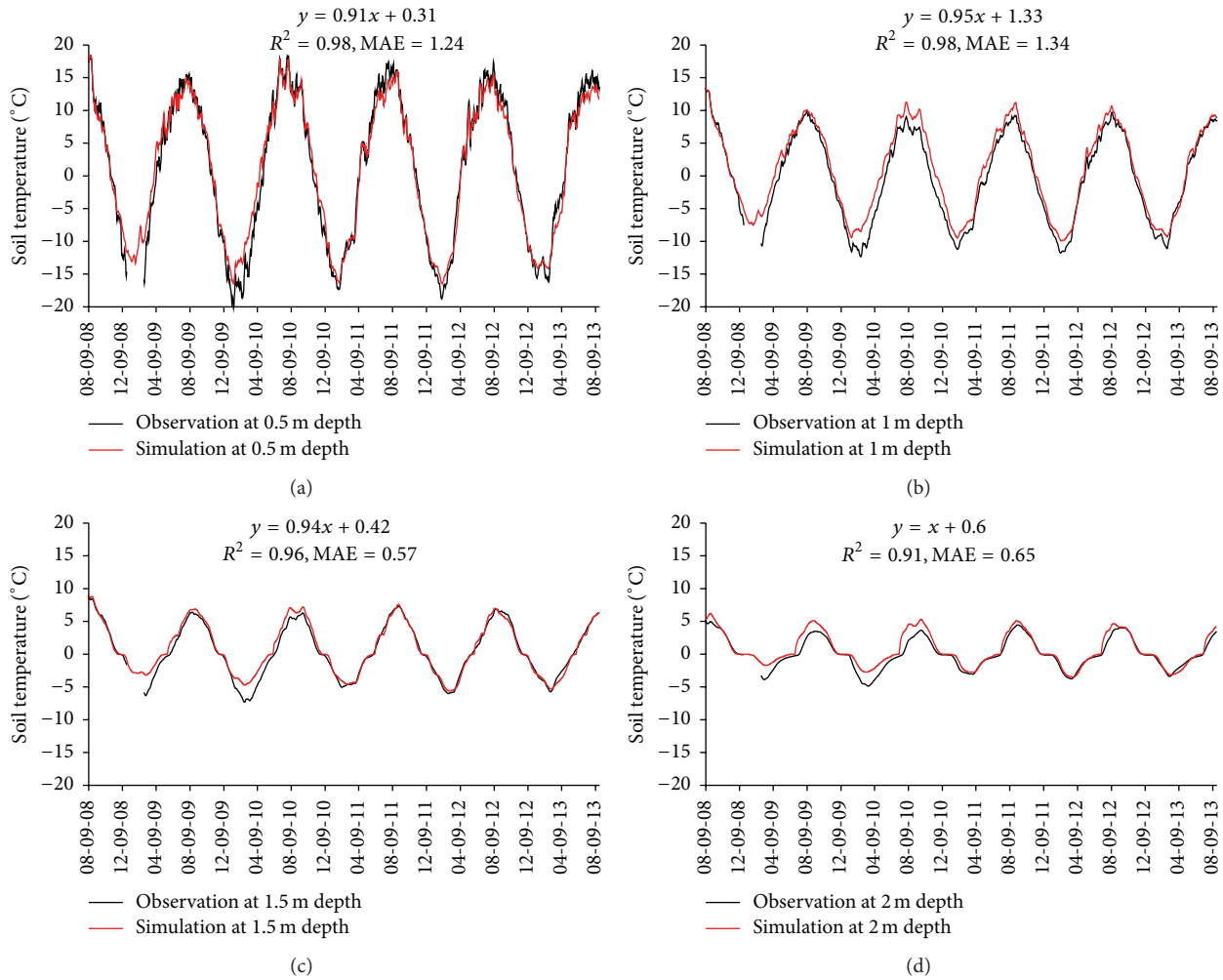


FIGURE 2: Comparison of simulated and observed soil temperature at the depths of 0.5 m, 1 m, 1.5 m, and 2 m, respectively. A linear analysis was conducted for each comparison, where R^2 is the coefficient of determination and MAE is the mean absolute error.

to estimate ET and LST. For each T_a scenario, the relationship of ET and LST for SWC = 0.2, 0.3, and 0.4 is similar, but for SWC = 0.1 the relationship is quite different. Below are detailed results and discussion regarding model calibration and the relationship of ET and LST under energy- and water-limited conditions.

3.1. Calibration Results for the SHAW Model. The comparison of simulated soil temperature and soil water content against observed values at four depths was used to evaluate the performance of the calibrated SHAW model. Figure 2 shows that simulated soil temperature matches observed one well in magnitude and seasonal variation. A linear analysis was conducted for each comparison. The coefficient of determination (R^2) is greater than 0.9, and the mean absolute error (MAE) is less than 1.4°C at four depths. Figure 3 shows that simulated soil water content also matches observed one well in magnitude. The mean absolute error (MAE) is less than 0.015 at four depths. The simulated soil water content can capture the soil water recharge from precipitation as

shown in Figure 3(a). Soil temperature and soil water content are two key variables of water and thermal processes in soil. Therefore, the consistence of soil temperature and soil water content between simulated and observed values could indicate that the calibrated SHAW model could perform well to investigate the relationship of ET and LST.

3.2. Relationship of ET and LST under the Energy-Limited Condition in a Cold and Dry Climate. The relationship of ET and LST under the soil moisture condition of SWC = 0.4 exhibited two patterns for nine simulations when T_a varied from -1 to 15°C. As shown in Figure 4, simulations with T_a from -1 to 5°C show that ET increases as LST increases, but this trend becomes progressively weaker with increases in T_a . The slope of linear regression analysis gradually decreases from 0.0059 to 0.0037, and the value of R^2 also decreases from 0.8356 to 0.1153. The relationship of ET and LST abruptly changes at $T_a = 7^\circ\text{C}$, and the slope of linear regression analysis becomes -0.0329 ($R^2 = 0.1525$). This negative trend becomes stronger as T_a increases from 7°C to 15°C; the slope

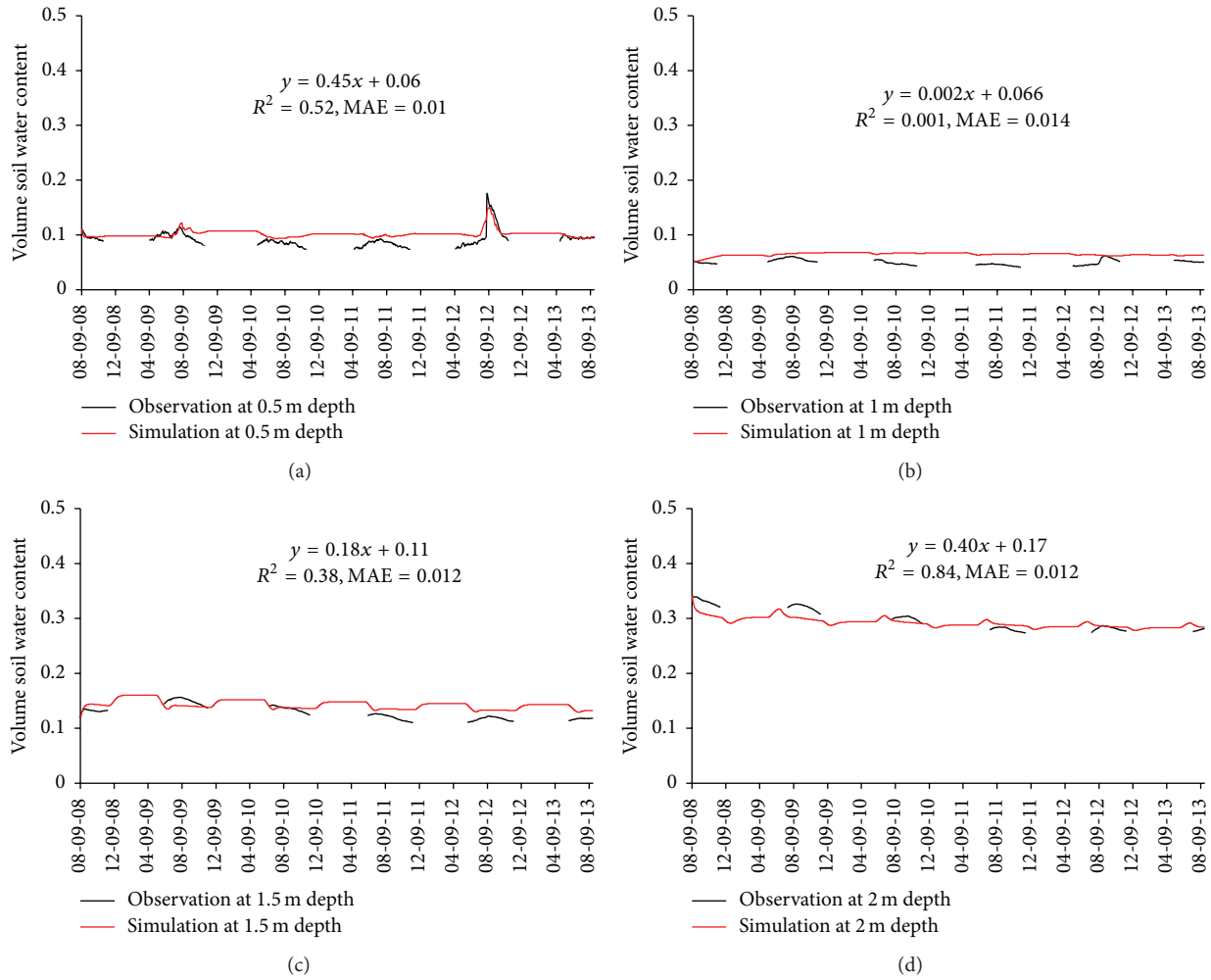


FIGURE 3: Comparison of simulated and observed soil water content at the depths of 0.5 m, 1 m, 1.5 m, and 2 m, respectively. A linear analysis was conducted for each comparison, where R^2 is the coefficient of determination and MAE is the mean absolute error.

of linear regression analysis decreases from -0.0329 to -0.0636 , and the value of R^2 increases from 0.1525 to 0.2946 .

Figures 4(a)–4(e) show that higher land surface temperature enhances ET when air is cold ($T_a \leq 5^\circ\text{C}$) and soil water is not limited. These results suggest that some caution should be noted when ET is estimated from LST-dependent ET models and VI-LST methods. These methods for ET estimation assume that ET cools terrestrial surfaces through vegetation transpiration and soil (or water surface) evaporation and that moist/watered surfaces have relatively low values of LST. However, these assumptions are invalid under the energy-limited condition ($T_a \leq 5^\circ\text{C}$, $\text{SWC} = 0.4$).

3.3. Relationship of ET and LST under the Water-Limited Condition in a Cold and Dry Climate. Compared with the energy-limited condition, the relationship of ET and LST under the water-limited condition ($\text{SWC} = 0.1$) is relatively straightforward. As shown in Figure 4, the trend of decreasing ET with increasing LST becomes more distinct as T_a is increased from -1 to 15°C . The slope of linear regression analysis gradually decreases from -0.0022 to -0.0097 , and the value

of R^2 increases from 0.1323 to 0.6552 . Results from Figure 4 indicate that ET has an apparent cooling effect even when T_a is less than or equal to 5°C under the water-limited condition ($\text{SWC} = 0.1$). Under such a condition, the assumption of ET cooling appears to be valid, and ET can be estimated from LST-dependent ET models and VI-LST methods.

3.4. Effect of Plant Transpiration on the Relationship of ET and LST under the Energy- and Water-Limited Conditions in a Cold and Dry Climate. Plant transpiration has a clear impact on the relationship of ET and LST under the energy-limited condition. As shown in Figure 5, the relationship of ET and LST becomes negative when T_a is greater than 5°C , which for this study was set as the temperature above which plants start to transpire. It indicates that soil evaporation has no clear cooling function when $T_a \leq 5^\circ\text{C}$, whereas plant transpiration above 5°C can cool land surfaces under the energy-limited condition.

Plant transpiration has less impact on the relationship of ET and LST under the water-limited condition. As shown in Figure 5, the relationship of ET and LST remains negative

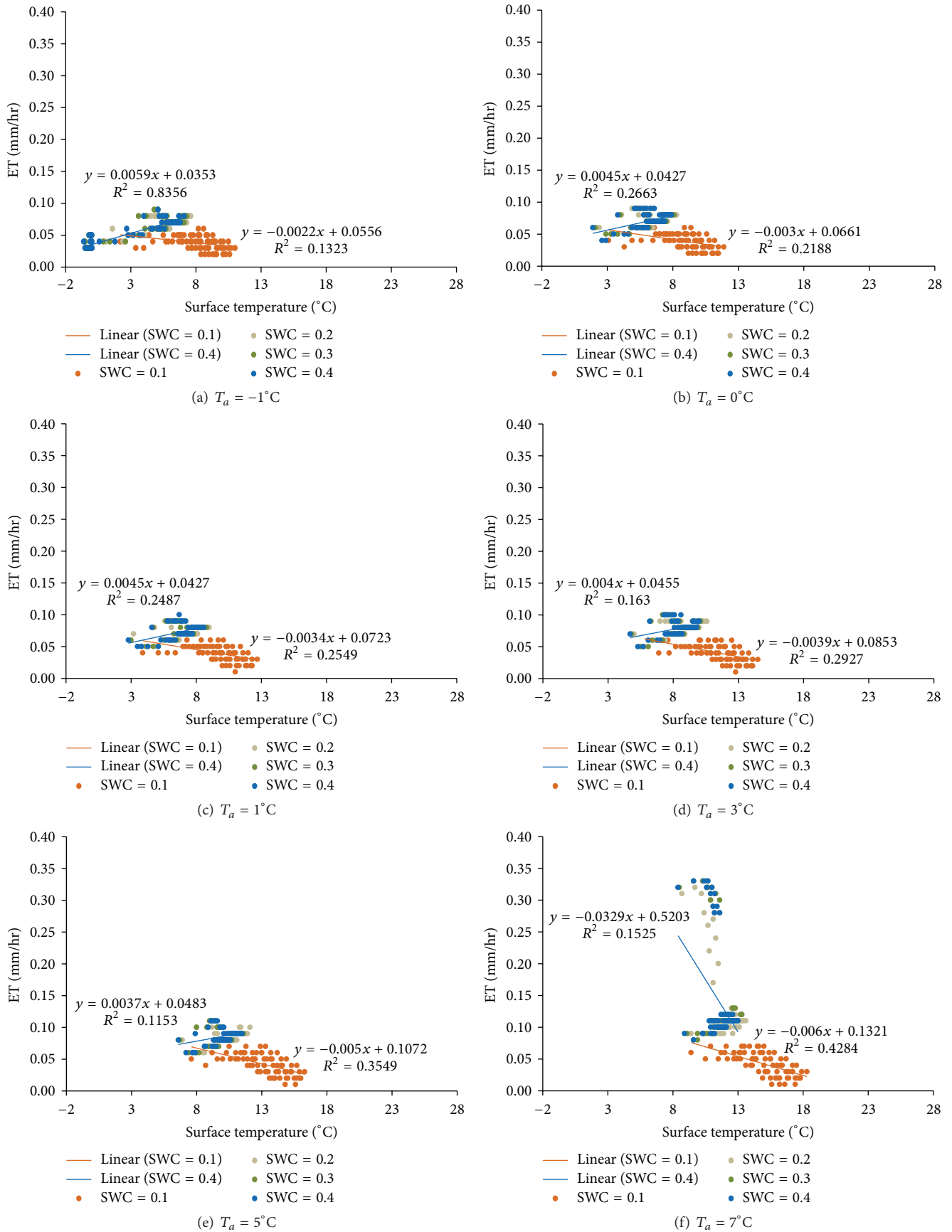


FIGURE 4: Continued.

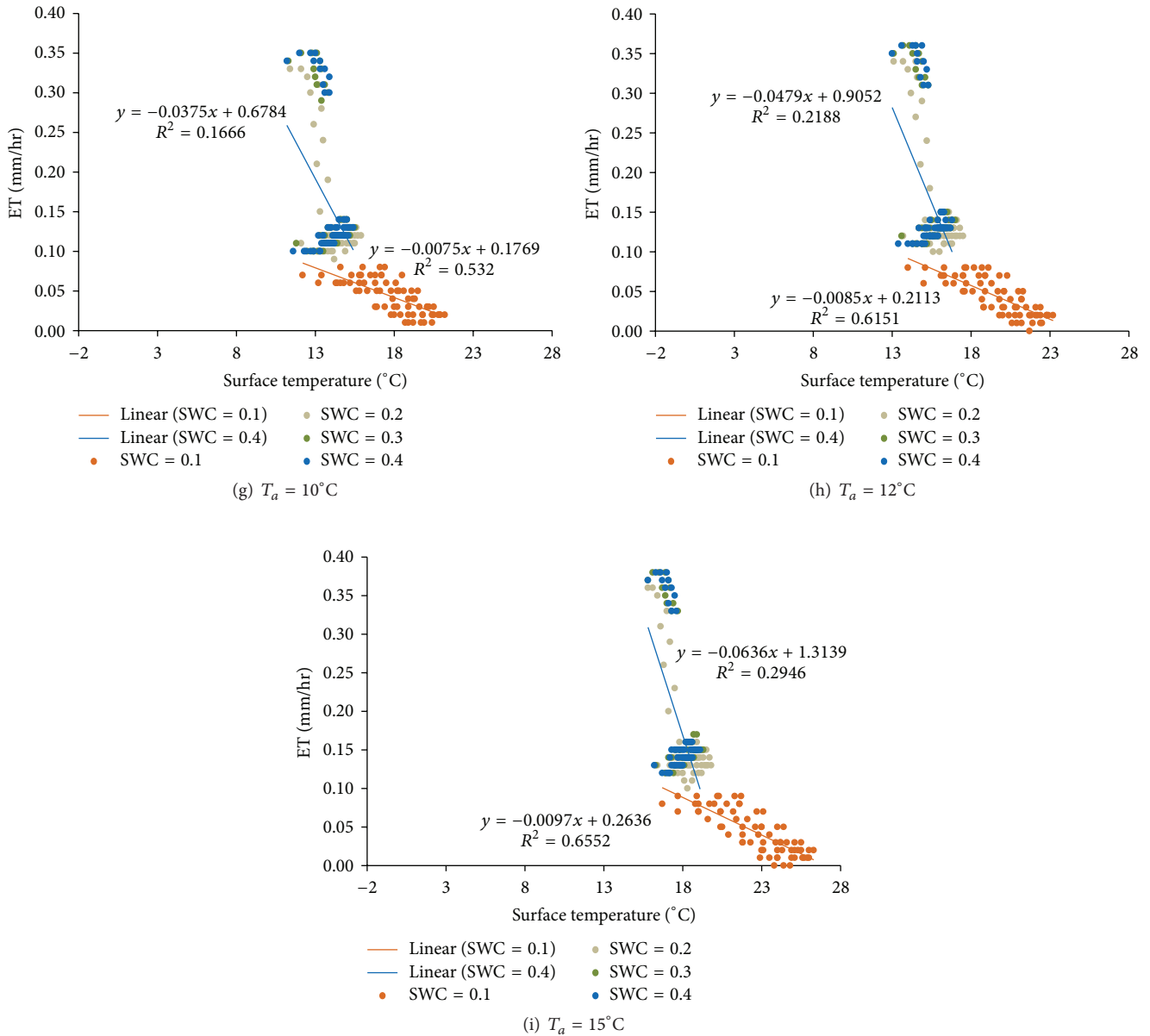


FIGURE 4: ET and LST under nine scenarios of air temperature and four scenarios of soil water content.

under the water-limited condition, and this negative relationship becomes more pronounced when $T_a > 5^\circ\text{C}$ (Figure 6). This indicates that soil evaporation has a cooling function even when $T_a \leq 5^\circ\text{C}$ and that plant transpiration above 5°C can enhance the cooling effect under the energy-limited condition.

Summarizing the inferences drawn from Figures 5 and 6, plant transpiration shows a cooling effect under both energy- and water-limited conditions, while soil evaporation has a cooling effect under the water-limited condition only. These results suggest that care should be taken with ET estimation from LST-dependent ET models and VI-LST methods at temperatures below which plants do not transpire ($T_a \leq 5^\circ\text{C}$ in this study).

3.5. Comparison of ET and LST Relationships between Energy- and Water-Limited Conditions. Under the water-limited condition, the relationship of ET and LST is always negative across the T_a range from -1 to 15°C . With the assumption of an ET cooling function under the dry and cold condition, therefore, LST-dependent ET models and VI-LST methods can be used for ET estimation. Under the energy-limited condition, however, the ET estimating methods mentioned above do not work and the assumption of an ET cooling function is invalid when $T_a \leq 5^\circ\text{C}$. The reason for this might be that the energy storage of moist/watered soil and plants is larger than that of dry soil and plants, and it is comparable to available energy for moist/watered soil and plants. This suggests that ET estimation methods based on

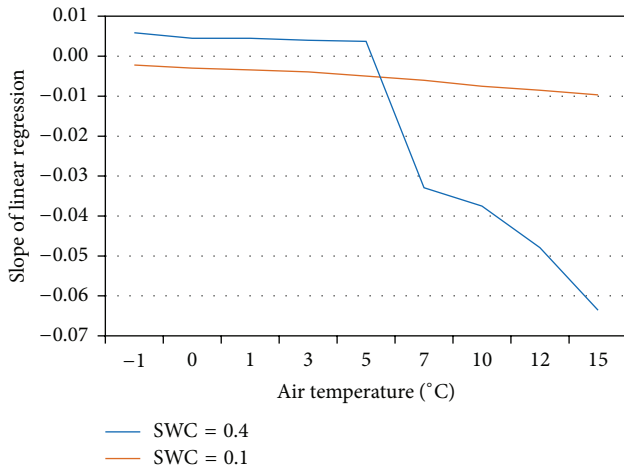


FIGURE 5: Slope of linear regression for ET and LST with nine scenarios of air temperature and two scenarios of soil water content.

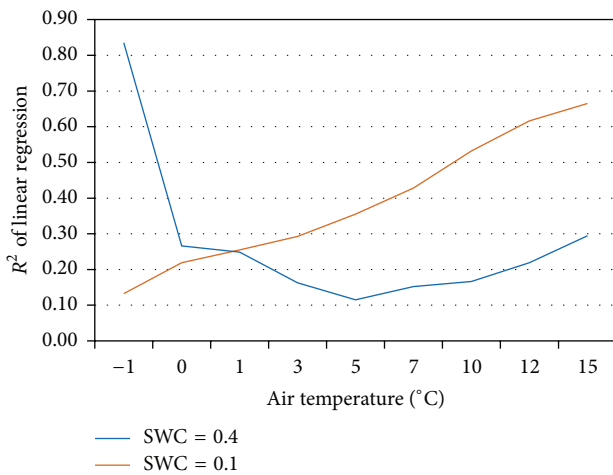


FIGURE 6: R^2 of linear regression for ET and LST with nine scenarios of air temperature and two scenarios of soil water content.

the land surface energy balance equation might be useful under the energy-limited condition if the energy storage by moist/watered soil and plants is accounted for in the land surface energy balance equation.

4. Conclusions

The energy- and water-limited ET processes should be considered and included in the methods used for ET estimation in cold and dry climates. In this study, the process-based SHAW model along with ground observational data was used to simulate ET and LST in order to understand the relationship of ET and LST under energy- and water-limited conditions. Simulation results indicated that ET and LST have a positive relationship when $T_a \leq 5^\circ\text{C}$ and a negative relationship when $T_a > 5^\circ\text{C}$ under the energy-limited condition (SWC = 0.4). However, ET and LST maintain a negative relationship under the water-limited condition (SWC = 0.1). Plant transpiration and energy storage in

moist/watered soil and plants can potentially explain the differences in the relationship of ET and LST simulated under the energy-limited and water-limited conditions. Plant transpiration likely affects the relationship of ET and LST due to its relatively strong cooling effect under the energy-limited condition. The energy storage of moist/watered soil and plants, which is comparable to the available energy, has a relatively large contribution to ET when $T_a \leq 5^\circ\text{C}$. This study suggests that different strategies should be used to estimate ET under the energy-limited condition in a dry and cold climate.

Conflict of Interests

The authors declare that there is no conflict of interests regarding the publication of this paper.

Acknowledgments

This research was supported by the 100 Talents Program of the Chinese Academy of Sciences. This research was also supported by the Grant-in-Aid for Encouragement, Center for Regional Environmental Research, National Institute for Environmental Studies, Japan, and by the Environment Research and Technology Development Fund, the Ministry of Environment, Japan.

References

- [1] S. Jasechko, Z. D. Sharp, J. J. Gibson, S. J. Birks, Y. Yi, and P. J. Fawcett, "Terrestrial water fluxes dominated by transpiration," *Nature*, vol. 496, no. 7445, pp. 347–350, 2013.
- [2] K. Wang and R. E. Dickinson, "A review of global terrestrial evapotranspiration: observation, modeling, climatology, and climatic variability," *Reviews of Geophysics*, vol. 50, no. 2, pp. 1–54, 2012.
- [3] J. Balogh, S. Fóti, K. Pintér et al., "Soil CO_2 efflux and production rates as influenced by evapotranspiration in a dry grassland," *Plant and Soil*, vol. 388, no. 1-2, pp. 157–173, 2015.
- [4] A. Harper, I. T. Baker, A. S. Denning, D. A. Randall, D. Dazlich, and M. Branson, "Impact of evapotranspiration on dry season climate in the Amazon forest," *Journal of Climate*, vol. 27, no. 2, pp. 574–591, 2014.
- [5] J. B. Wu, Y. L. Jing, D. X. Guan et al., "Controls of evapotranspiration during the short dry season in a temperate mixed forest in Northeast China," *Ecohydrology*, vol. 6, no. 5, pp. 775–782, 2013.
- [6] M. C. R. Alberto, J. R. Quilty, R. J. Buresh et al., "Actual evapotranspiration and dual crop coefficients for dry-seeded rice and hybrid maize grown with overhead sprinkler irrigation," *Agricultural Water Management*, vol. 136, pp. 1–12, 2014.
- [7] M. C. Anderson, C. Hain, B. Wardlow, A. Pimstein, J. R. Mecikalski, and W. P. Kustas, "Evaluation of drought indices based on thermal remote sensing of evapotranspiration over the continental United States," *Journal of Climate*, vol. 24, no. 8, pp. 2025–2044, 2011.
- [8] A. J. Teuling, A. F. Van Loon, S. I. Seneviratne et al., "Evapotranspiration amplifies European summer drought," *Geophysical Research Letters*, vol. 40, no. 10, pp. 2071–2075, 2013.

- [9] Z. G. Sun, Q. X. Wang, B. Matsushita, T. Fukushima, Z. Ouyang, and M. Watanabe, "Development of a simple remote sensing EvapoTranspiration model (Sim-ReSET): algorithm and model test," *Journal of Hydrology*, vol. 376, no. 3-4, pp. 476–485, 2009.
- [10] Z.-L. Li, R. L. Tang, Z. M. Wan et al., "A review of current methodologies for regional evapotranspiration estimation from remotely sensed data," *Sensors*, vol. 9, no. 5, pp. 3801–3853, 2009.
- [11] W. G. M. Bastiaanssen, M. Menenti, R. A. Feddes, and A. A. M. Holtslag, "A remote sensing surface energy balance algorithm for land (SEBAL): 1. Formulation," *Journal of Hydrology*, vol. 212, no. 1-4, pp. 198–212, 1998.
- [12] G. J. Roerink, Z. Su, and M. Menenti, "S-SEBI: a simple remote sensing algorithm to estimate the surface energy balance," *Physics and Chemistry of the Earth, Part B: Hydrology, Oceans and Atmosphere*, vol. 25, no. 2, pp. 147–157, 2000.
- [13] Z. Su, "The Surface Energy Balance System (SEBS) for estimation of turbulent heat fluxes," *Hydrology and Earth System Sciences*, vol. 6, no. 1, pp. 85–99, 2002.
- [14] R. G. Allen, M. Tasumi, A. Morse et al., "Satellite-based energy balance for mapping evapotranspiration with internalized calibration (METRIC)—applications," *Journal of Irrigation and Drainage Engineering*, vol. 133, no. 4, pp. 395–406, 2007.
- [15] R. G. Allen, M. Tasumi, and R. Trezza, "Satellite-based energy balance for mapping evapotranspiration with internalized calibration (METRIC)—model," *Journal of Irrigation and Drainage Engineering*, vol. 133, no. 4, pp. 380–394, 2007.
- [16] L. Jiang and S. Islam, "Estimation of surface evaporation map over southern Great Plains using remote sensing data," *Water Resources Research*, vol. 37, no. 2, pp. 329–340, 2001.
- [17] T. Carlson, "An overview of the 'triangle method' for estimating surface evapotranspiration and soil moisture from satellite imagery," *Sensors*, vol. 7, no. 8, pp. 1612–1629, 2007.
- [18] R. L. Tang, Z.-L. Li, and B. H. Tang, "An application of the Ts-VI triangle method with enhanced edges determination for evapotranspiration estimation from MODIS data in arid and semi-arid regions: implementation and validation," *Remote Sensing of Environment*, vol. 114, no. 3, pp. 540–551, 2010.
- [19] M. Garcia, N. Fernández, L. Villagarcía, F. Domingo, J. Puigdefábregas, and I. Sandholt, "Accuracy of the Temperature-Vegetation Dryness Index using MODIS under water-limited vs. Energy-limited evapotranspiration conditions," *Remote Sensing of Environment*, vol. 149, pp. 100–117, 2014.
- [20] R. R. Nemani, C. D. Keeling, H. Hashimoto et al., "Climate-driven increases in global terrestrial net primary production from 1982 to 1999," *Science*, vol. 300, no. 5625, pp. 1560–1563, 2003.
- [21] A. Hope, R. Engstrom, and D. Stow, "Relationship between AVHRR surface temperature and NDVI in Arctic tundra ecosystems," *International Journal of Remote Sensing*, vol. 26, no. 8, pp. 1771–1776, 2005.
- [22] A. Karnieli, N. Agam, R. T. Pinker et al., "Use of NDVI and land surface temperature for drought assessment: merits and limitations," *Journal of Climate*, vol. 23, no. 3, pp. 618–633, 2010.
- [23] G. N. Flerchinger, "Sensitivity of soil freezing simulated by the SHAW model," *Transactions of the ASAE*, vol. 34, no. 6, pp. 2381–2389, 1991.
- [24] G. N. Flerchinger, T. G. Caldwell, J. Cho, and S. P. Hardegree, "Simultaneous heat and water (SHAW) model: model use, calibration, and validation," *Transactions of the ASABE*, vol. 55, no. 4, pp. 1395–1411, 2012.
- [25] Z. G. Sun, Q. X. Wang, Q. G. Xiao, O. Batkhisig, and M. Watanabe, "Diverse responses of remotely sensed grassland phenology to interannual climate variability over frozen ground regions in Mongolia," *Remote Sensing*, vol. 7, no. 1, pp. 360–377, 2015.